2012

Tunable Luminescence And White Light Emission Of Lanthanide-Doped Cawo4 And Casio3 Phosphors Prepared By Pechini And Traditional Sol-Gel Methods

Matthew Anwar Mickens
North Carolina Agricultural and Technical State University

Tunable Luminescence and White Light Emission of Lanthanide-Doped $CaWO_4$ and $CaSiO_3$ Phosphors Prepared by Pechini and Traditional Sol-Gel Methods

Matthew Anwar Mickens

North Carolina A&T State University

A dissertation submitted to the graduate faculty

in partial fulfillment of the requirements for the degree of

DOCTOR OF PHILOSOPHY

Department: Energy and Environmental Systems

Major: Energy and Environmental Systems (Inorganic Chemistry)

Major Professor: Dr. Zerihun Assefa

Greensboro, North Carolina

2012

School of Graduate Studies
North Carolina Agricultural and Technical State University

This is to certify that the Doctoral Dissertation of

Matthew Anwar Mickens

has met the dissertation requirements of
North Carolina Agricultural and Technical State University

Greensboro, North Carolina
2012

Approved by:

Zerihun Assefa, Ph.D. Major Professor	Dhananjay Kumar, Ph.D. Committee Member
Alex Williamson, Ph.D. Committee Member	Solomon Bililign, Ph.D. Committee Member
Keith Schimmel, Ph.D. Committee Member and Department Chairperson	Sanjiv Sarin, Ph.D. Associate Vice Chancellor for Research and Dean of Graduate Studies

Biographical Sketch

Matthew Mickens was born on March 31, 1984, in Durham, North Carolina. He received a Bachelor of Science in Earth and Environmental Science on June 28, 2006 from North Carolina A&T State University. Upon completing his undergraduate studies, he also received the Waste Management Institute Certificate and Scholarship. During his undergraduate term, he had the experience of participating with organizations such as the NC A&T "Blue and Gold Marching Machine" marching band, and the Environmental Science Club, all while he worked part-time at the United Parcel Service. For his graduate studies, he received a Master of Science degree in Plant, Soil, and Environmental Science on May 10, 2008 from North Carolina A&T State University. He was also awarded several Student Excellence Awards for maintaining a 4.0 GPA throughout both his Master's and Doctoral studies. He was inducted into the Phi Kappa Phi Honor Society in 2008, the Golden Key International Honor Society in 2010, and awarded positions in both the North Carolina Space Grant Fellowship Program and the NASA Harriett G. Jenkins Predoctoral Fellowship Program. He has made poster presentations at several conferences including the National Association of Black Geologists and Geophysicists Conference (NABGG) in Phoenix AZ, the Charlotte Biotechnology Conference, and the NASA Ames STEM Symposium in San Jose, CA. Based on his achievement and personality, he was selected in 2006 to represent North Carolina A&T State University nationally on the Black Entertainment Television series "106 & Park." He is now a candidate for the Ph.D. in Energy and Environmental Systems.

Acknowledgments

My greatest praise goes to God, my Creator through Jesus Christ. My greatest appreciation goes to my advisor, Dr. Zerihun Assefa for allowing me to design my own project, for pushing me to become the expert of my system, and for sharing the excitement with me whenever there was a new finding. This really meant a lot to me and gave me the energy to keep going. I also extend thanks to my committee members Dr. Dhananjay Kumar and Dr. Alex Williamson for their ideas, advice, and humor at times when it was needed, and Dr. Solomon Bililign for showing me the importance of understanding the fundamental mathematics of my work, no matter how painful it was, it worked together for good. Last but certainly not least, Dr. Keith Schimmel, my department chairperson, is the reason this dissertation has been written. I want to thank him for recruiting me through an email sent in May of 2008 that encouraged me to apply for a Ph.D. and ultimately led to the largest achievement of my life.

Those who have contributed experimentally to this work include Dr. Sergey Yarmolenko (XRD), Dr. Cynthia Day (XRD), James King (FT-IR), Carlos Crawford (QY), Dr. Zhigang Xu (SEM), and Kwadwo Mensah–Darkwa (SEM). Indirect contributions were made by Carolyn Mayo, Charles Wilson, Dr. Margaret Kanipes, and my lifetime mentor Dr. Arona Diouf. I also salute Dr. Sonya Greene of the NASA Harriett G. Jenkins Predoctoral Fellowship Program.

I wish to thank my group members Dr. Darkus Jenkins, Kendra Whitehead, and Shaka Gore who kept me sane with the entertaining “closet” stories of their lives. I want to thank John Foster, David Galloway, and the Deep River Church of Christ for spiritual encouragement and prayers. I am grateful to have had my mother Phyllis Mickens, and my cousin Eddie Drew as first hand witnesses to all of my labors. Lastly, I thank the rest of my family and friends not mentioned here who have always believed in me from the beginning.

Table of Contents

List of Figures

List of Tables

Nomenclature

Å	Angstrom
a.u.	Arbitrary unit
C	Celsius
CCT	Correlated color temperature
CIE	Commission Internationale de I'Eclairage (International Commission on Illumination)
CT	Charge transfer
D_{65}	Standard daylight illuminant with color temperature ~6500 ºK
Em	Emission
Exc	Excitation
FT-IR	Fourier Transform Infrared Spectroscopy
GaN	Gallium nitride
InGaN	Indium gallium nitride
JCPDS	Joint Committee on Powder Diffraction Standards
K	Kelvin
LED	Light-emitting diode
Ln	Lanthanide
mg	Milligram
mL	Milliliter
mol	Mole
ms	Millisecond
NASA	National Aeronautics and Space Administration

nm	Nanometer
ns	Nanosecond
NR	Non-radiative
PEG	Polyethylene glycol
PL	Photoluminescence
PMT	Photomultiplier tube
QY	Quantum yield
RGB	Red-green-blue
SEM	Scanning electron microscopy
SSL	Solid-state lighting
T_c	Correlated color temperature
UV	Ultraviolet
VUV	Vacuum ultraviolet
WLED	White light-emitting diode
XRD	X-ray Diffraction
YAG:Ce	Yttrium aluminum garnet doped with cerium
ΔE	Energy gap
λ	Wavelength
μL	Microliter
μm	Micrometer
μs	Microsecond
ν_{max}	Highest vibrational frequency
τ	Lifetime

Abstract

This study reports the synthesis, characterization, and photoluminescence properties of a calcium tungstate/molybdate ($CaWO_4/MoO_4$) system, and the synthetic attempts of an agrellite ($NaCa_2Si_4O_{10}F$) system. The objective is to modify the photoluminescence of both systems by doping with lanthanide/transition metal ions, and to convert them into phosphors with specific applications for light-emitting-diodes (LEDs).

$CaWO_4$ is used as a host matrix to fabricate a white light phosphor. When MoO_4 is added to the system, its excitation range is extended, and its emission profile can be tuned by changing excitation wavelength. The simultaneous inclusion of Tm^{3+}, Tb^{3+}, and Eu^{3+} ions results in the phosphor emitting several hues of white light tunable by varying the excitation wavelength. Additionally, a comparison study of $CaWO_4$ doped with Eu^{3+} showed that the inclusion of Na^{+} enhances the red emission of Eu^{3+}, allowing the phosphor to emit ratios of blue and red light that are also tunable by excitation wavelength. The overall emission profile of the phosphor resembles the absorption profile of chlorophyll, allowing for potential utilization in a blue/red-emitting LED for plant growth.

The photoluminescence of natural agrellite is scarcely found in the literature and has been reported here. Moreover, an attempt to synthesize the system by traditional sol-gel techniques and to replicate its pink emission was executed by using Ce^{3+}, Mn^{2+}, Dy^{3+}, and Sm^{3+} dopants. The synthetic phosphor was found to crystallize in a phase different from agrellite, but triply-doping it with Ce^{3+}, Tb^{3+}, and Mn^{2+} produced a novel white light-emitting phosphor with potential applications for white-LEDs.

CHAPTER 1

Tunable White Light-Emission of a $CaW_{1-x}Mo_xO_4:Tm^{3+}$, Tb^{3+}, Eu^{3+} Phosphor Prepared by a Pechini Sol-Gel Method

1.1. Introduction

The development of inorganic phosphors has stimulated a growing interest for applications in field emission displays [1], automobile headlights [2], radiation detectors [3, 4], and white light-emitting diodes (WLEDs) [5]. Among these applications, WLEDs are considered to be the next generation of solid-state lighting (SSL) technology used for general illumination [6]. Since the commercialization of the first WLED by Nichia Corporation in 1996 [7], tremendous progress has been achieved for solid-state lighting as indicated by recent reviews [8, 9]. In comparison to fluorescent lamps, WLEDs offer the advantages of higher luminous efficiency, energy savings, compact size, longer persistence, and absence of toxic mercury [10].

Conventionally, WLEDs are created by coupling a yellow-emitting phosphor, $Y_3Al_5O_{12}:Ce^{3+}$ (YAG:Ce), to a blue InGaN LED chip [11, 12]. This method is widely used because of low cost and high luminous flux; however, due to the lacking red component, this approach exhibits poor color rendering properties and cannot emit warm white light [13]. To remedy this drawback, the most promising route to fabricate WLEDs is by employing single-phased phosphors that emit red-green-blue (RGB) upon excitation by an ultraviolet (UV)-LED chip [13-17], or other full color-emitting phosphors that yield even higher color rendering properties [18, 19]. Although more expensive, WLEDs based on the latter routes have yet to reach their physical limit in terms of efficiency [8]. Moreover, their efficiency is constantly being improved as new materials are synthesized and made available, inevitably making them price-competitive with fluorescent lamps in the near future.

To date, numerous reports have shown that the light emission of calcium tungstate/molybdate $Ca(W,Mo)O_4$ phosphors with scheelite structure can be tuned by doping with lanthanide (Ln^{3+}) ions [20, 21]. Since Ln^{3+} ions exhibit parity-forbidden 4*f*–4*f* transitions shielded by filled $5s^25p^6$ sub-shells, their characteristic emissions are mostly retained from host to host. Nevertheless, the forbidden nature of 4*f*–4*f* transitions can be partially lifted by the symmetry influence of different crystalline hosts causing slight shifts in emission band maxima and intensities. In addition to their chemical and thermal stability, the relatively low vibrational energies permit efficient energy transfer to emitting Ln^{3+} centers [22], and has been a predominant motivation of several studies [23-29]. For instance, among alkaline-earth metal tungstates $AWO_4:Tm^{3+}$ ($A = Ca^{2+}$, Sr^{2+}, Ba^{2+}), it was shown by Liao *et al.* that $CaWO_4$ was the most suitable host for transferring its excitation energy to Tm^{3+} [30] and Sm^{3+} [31] ions.

In terms of observing white light, Nazarov *et al.* reports on varying the luminescence color of $CaWO_4:Eu^{3+},Tb^{3+}$ and generating white light emission by energy transfer, but it required high-energy VUV (147 nm) excitation [21]. Similarly, in $CaMoO_4$ systems, warm white light emission was also reported in a multivalent $CaMoO_4:Pr^{3+}$, Pr^{4+} phosphor [32], while cool white light was observed in $CaMoO_4:Eu^{3+}$ nanofibers studied by Hou *et al.* [24] as confirmed by chromaticity and photographs, but the observation was not emphasized in the report. One unique route to convert $CaWO_4/MoO_4$ hosts into white light-emitting phosphors is by combining the two systems. Zheng and co-workers [33] recently demonstrated the capability of extending the excitation range of $CaWO_4$ by the addition Mo, where cool white light was observed by varying the concentrations doped Eu^{3+} and Tb^{3+} ions. However, to the best of our knowledge, no investigation has reported utilizing a single-phased $Ca(W,Mo)O_4$ system where various hues of white light are observed by tuning the excitation wavelength.

This chapter discusses a $CaWO_4$ host doped with a small amount of Mo^{6+} ($CaW_{1-x}Mo_xO_4$) where its excitation properties were extended and wavelength-tunability of its emission was attained. Moreover, the extended excitation range was nonradiatively transferred to triply-doped RGB-emitting Ln^{3+} ions (Ln = Tm^{3+}, Tb^{3+}, Eu^{3+}) with the resulting emission being tunable between cool, natural, and warm white light.

1.2. Experimental

1.2.1. Sample synthesis. All chemicals and reagents were purchased from Sigma-Aldrich with the exception of ammonium molybdate, which was obtained from Baker & Adamson. The phosphors were prepared by the Pechini sol-gel method [34, 35]. The $CaWO_4$:Mo host was prepared by using the formula $CaW_{0.99}Mo_{0.01}O_4$, while the synthesis of the triply-doped phosphor samples adhered to the general formula $Ca_{1-2x-2y-2z}Tm_xTb_yEu_zNa_{x+y+z}W_{0.99}Mo_{0.01}O_4$. In proportion to Ca^{2+}, the doping concentrations of Ln^{3+} and Na^+ ions were 1 mol% Tm^{3+}, 0.5 mol% Tb^{3+}, 0.5 mol% Eu^{3+}, and 2 mol% Na^+. To obtain 0.5 g of doped phosphor product, a typical experiment involved dissolving 438 mg of ammonium tungstate ($(NH_4)_{10}W_{12}O_{41}\cdot 5H_2O$) and 3 mg of ammonium molybdate ($(NH_4)_6Mo_7O_{24}\cdot 4H_2O$) in a water-ethanol (*V/V=3:1)* solution containing 667 mg of citric acid ($C_6H_8O_7$) as the chelating agent for the metal ions. The molar ratio of metal ions to citric acid was 1:2. In a separate beaker, 166 mg of calcium carbonate (99.99% $CaCO_3$), 1.8 mg of sodium carbonate (99.5% Na_2CO_3), 3.3 mg of thulium oxide (99.99% Tm_2O_3), 1.6 mg of terbium oxide (99.99% Tb_4O_7), and 1.5 mg of europium oxide (99.99% Eu_2O_3) were dissolved in 5 mL of dilute nitric acid (70% HNO_3) under heated magnetic stirring until the solution became clear. The excess HNO_3 was removed by evaporation at ~100° C until crystallization of metal-nitrate salts was apparent, and deionized water was added to dissolve the nitrate salts. The resulting metal-nitrate solution was adjusted to a pH of 2–3, and

then added to the flask containing the metal-citrate solution. Polyethylene glycol (PEG; molecular weight = 200) was added as a cross-linking agent with a final concentration of 0.20 g mL^{-1}. The solution mixture was covered and stirred magnetically for 1 h at 70 ºC, and ultrasonically for 20 min to yield a highly transparent sol. The sol was transferred to an open beaker and placed in a water bath at 65 ºC for 8 h where it was concentrated to a viscous gel. The gel was immediately placed in an oven at 100 ºC for 30 min to drive off remaining solvents until a color change to transparent yellow was observed. While hot, the reduced viscosity of the gel allowed easy transfer to a porcelain crucible where annealing took place at 900 ºC for 2 h with a heating rate of 1 ºC min^{-1}. The phosphor powders were allowed to cool naturally in the furnace and were characterized immediately.

1.2.2. Structural characterizations by X-ray diffraction (XRD). Materials that exist in the solid-state can be either crystalline or amorphous. In a crystalline solid, the atoms are arranged in a well-ordered manner, whereas in amorphous solids the arrangement of atoms is random. Approximately 95% of all solid materials can be classified as crystalline. The X-ray diffraction (XRD) method is routinely used as a finger-print method for the characterization of solid materials. The inspection using XRD is a non-destructive method to determine the average spacing between atoms and identifies the crystal structure and/or phase, it provides an estimation of the average grain size of powders, and evaluates the level of lattice strain. X-rays are a form of electromagnetic radiation with a wavelength in the range of 0.01–10 nm. When a beam of X-rays penetrates a solid material, a portion of the beam interacts with the electron density associated with each atom present, and is diffracted at angles specific to the composition of the material. An XRD spectrum shows the intensity of the diffracted X-rays as a function of the detecting angle

2θ. The interplanar spacings, d, that correspond to the peaks observed in an XRD pattern are calculated by Bragg's diffraction law which is given by:

$$n\lambda = 2d\sin\theta \quad (1.1)$$

where

n = the order of reflection

λ = the wavelength of the penetrating X-ray beam

d = distance between atomic layers of a crystal

θ = angle of incidence

The diffraction of X-rays by interatomic planes in a solid crystalline material is illustrated by Figure 1.1.

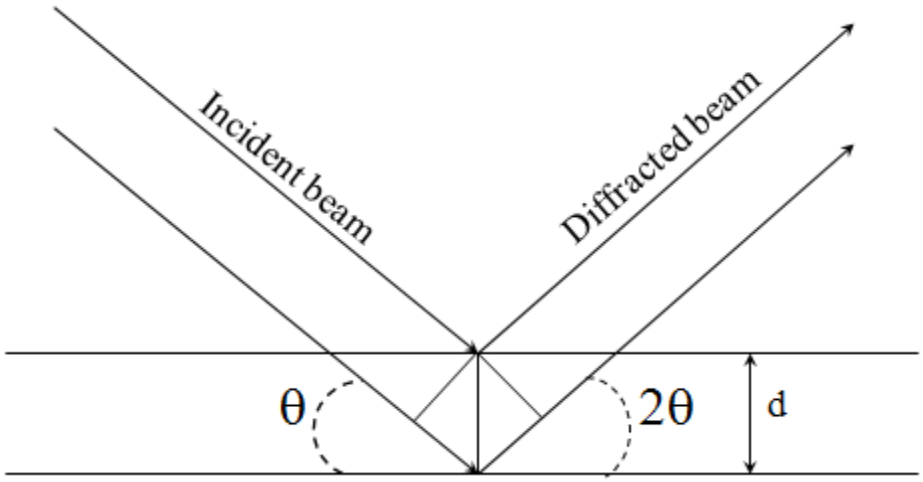

Figure 1.1. Diffraction of X-rays by interplanar arrangement of atoms.

To prepare for XRD analysis, the solid powder samples were uniformly spread onto glass microscope slides using a double-sided adhesive. The XRD patterns were collected in the range of $10^o < 2\theta < 90^o$ using a Bruker D8 Advance X-ray diffractometer with a Cu Kα radiation source (λ=0.15418 Å). The voltage and current were maintained at 40 kV and 40 mA, respectively. The increment used was 0.01426 at a scan rate of $0.1^o\ s^{-1}$. All obtained spectra were

compared to standard XRD patterns provided by the Joint Commission on Powder Diffraction Standards (JCPDS).

1.2.3. Morphology analysis by scanning electron microscope (SEM). A scanning electron microscope (SEM) is useful to produce high-resolution micro-structural images of solid-state materials and can be used to quantify particle size and crystallite structure. In comparison to conventional light microscopes, SEM exhibits better resolution, higher magnification, greater depth of focus, and easy sample preparation. These advantages have made SEM a common characterization method for solid-state materials today. An SEM employs an electron gun that emits a beam of electrons through objective and condenser lenses where the beam is impinged on a very fine spot of the sample. A set of scanning coils located in the region between the sample and the magnetic lenses are then energized by a scan generator which creates a magnetic field that rasters the beam across the specimen. When the beam strikes the sample surface, secondary electrons are removed from the sample and collected by a detector which converts them into an electrical signal. The detector sends the signal to a screen display to generate the final image of the material.

A schematic diagram of an SEM is presented in Figure 1.2. The morphology of the phosphors in this chapter was inspected using a Hitachi S-3000N SEM. The accelerating voltage was maintained at 5.0 kV and the working distance used was 11.6 mm. The phosphor powders were applied evenly to a copper-conducting adhesive and excess powders were removed with a compressed air can to ensure a thin layer of sample, and it was then placed on the sample stage for analysis.

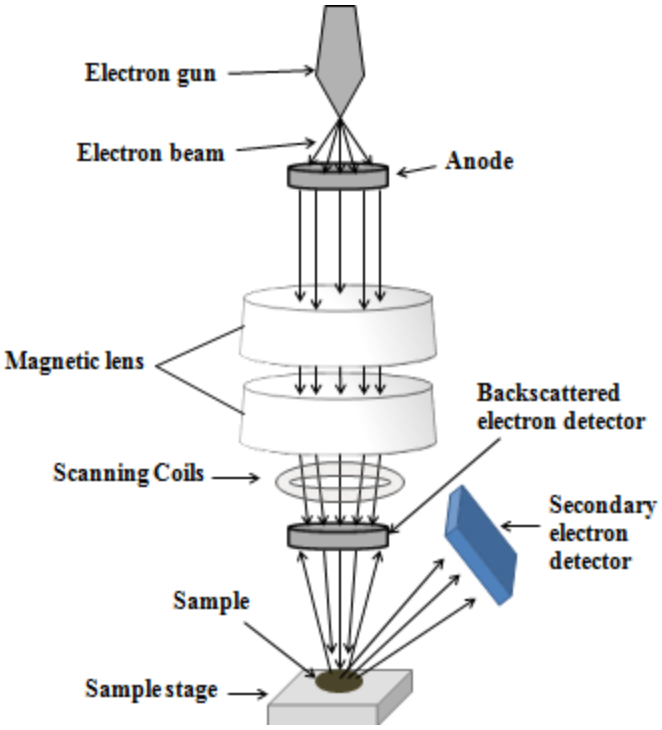

Figure 1.2. Schematic illustration of scanning electron microscope.

1.2.4. Photoluminescence (PL) characterization. The PL studies were conducted on the basis of excitation and emission spectra using a Shimadzu RF-5301 spectrofluorophotometer equipped with a 150 W xenon lamp excitation source. All spectroscopic measurements were performed at room temperature. A general schematic of the spectrofluorophotometer system is shown in Figure 1.3. The spectroscopic data were acquired and managed by HyperRF software (Version 1.57). During the course of a measurement, all phosphor powders were placed on an iron platform inside the sample chamber that was aligned perpendicularly with both monochromator lenses. The platform had dimensions of 5×3×1 inches (L×W×H). The samples were excited directly on the iron platform for the analysis. To avoid contamination, the platform was cleaned with methanol before and after a new sample was analyzed.

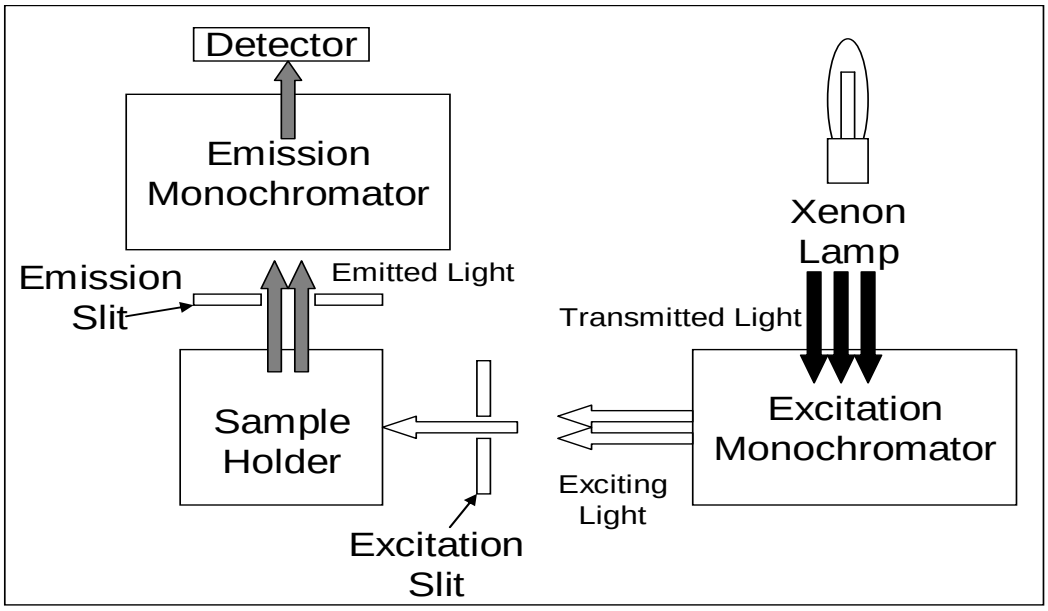

Figure 1.3. Schematic arrangement of the spectrofluorophotometer instrumentation.

The selection of an excitation wavelength was controlled by parameters in the software. In brief, the excitation monochromator isolated the desired wavelength from the light generated by the xenon lamp. After the sample was excited by the selected wavelength, the resulting emission was then pointed toward the emission monochromator lens which focused the light to the detector. The detector converts the photon signal into an electrical signal. Coupled with the detector was a photomultiplier tube (PMT) made up of dynodes that multiply the electrical signal by up to one million times that of the initial incident photon. Lastly, the output signal is converted into an analytical curve observed as a spectrum on a computer monitor. There were inherent restrictions with the use of the spectrofluorophotometer that had to be followed to prevent damage to the PMT by overflow of electric charge. The second and third order components of the excitation wavelength could easily burn out the PMT. To determine the range of wavelengths used for generating a spectrum, the beginning and ending of the range had to reside at a specific distance in nm, from the fixed excitation or emission wavelength. In this case,

the restrictions for the Shimadzu RF-5301 spectrofluorophotometer are demonstrated by the following:

$\lambda_{min\ em} = (\lambda_{exc}) + 20$ nm for minimum wavelength in emission spectrum range

$\lambda_{max\ em} = 2(\lambda_{exc}) - 20$ nm for maximum wavelength in emission spectrum range

$\lambda_{max\ exc} = (\lambda_{em}) - 20$ nm for maximum wavelength in excitation spectrum range

$\lambda_{min\ exc} = (\lambda_{em})/2 + 20$ for minimum wavelength in excitation spectrum range

where λ_{exc} is the fixed excitation wavelength, and λ_{em} is the fixed emission wavelength. For example, if 300 nm was the fixed excitation wavelength, then the scanned emission range had to begin with a minimum wavelength of 320 nm, and could not exceed 580 nm. Likewise, if 500 nm was used as the fixed emission wavelength, then the scanned excitation range had to begin with 270 nm, and could not exceed 480 nm. The obtained data were later exported to Microsoft Excel for manipulation and figure preparation.

1.2.5. CIE chromaticity and color temperature characterizations. The basic principles of chromaticity are described in detail in order to fully understand the characterization and expression of colors derived from light. The method is used in the group for the first time and thus a detailed background of the characterization method is given below. Standard functions of the three primary colors RGB were determined in 1931 by the Commission Internationale de l'Eclairage (CIE), or the International Commission on Illumination. The appearance of any color, is composed of three tristimulus values, denoted *X*, *Y*, and *Z*. These values are derived parameters representing the primary colors (RGB) that are added together to produce a specific color. Early experiments conducted by Guild [36] and Wright [37] matched the average response of the human eye to the tristimulus functions. However since then, the CIE has defined an improved set of three color-matching functions known as $\bar{x}(\lambda)$, $\bar{y}(\lambda)$, and $\bar{z}(\lambda)$ which can be

treated as if they were the spectral response curves for the cone-receptors in the human eye as shown in Figure 1.4 [38].

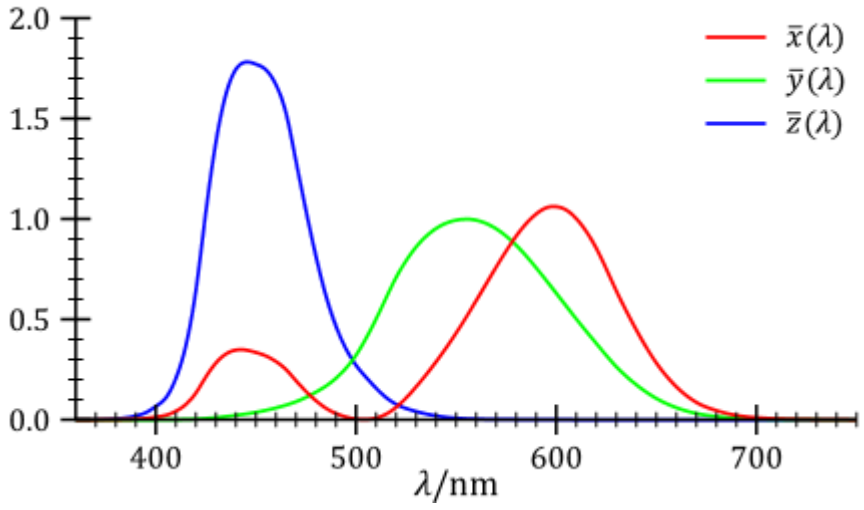

Figure 1.4. The CIE standard observer color matching functions [38].

The tristimulus values of a color with a spectral radiance distribution of $I(\lambda)$ are given by:

$$X = \int_0^\infty I(\lambda)\bar{x}(\lambda)d\lambda;$$

$$Y = \int_0^\infty I(\lambda)\bar{y}(\lambda)d\lambda;$$

$$Z = \int_0^\infty I(\lambda)\bar{z}(\lambda)d\lambda;$$

where λ is the wavelength of the equivalent monochromatic light (in nm), and $\bar{x}(\lambda)$, $\bar{y}(\lambda)$, and $\bar{z}(\lambda)$ are the color-matching functions that yield the *X*, *Y*, *Z* tristimulus components of color. Since the human eye has three types of color sensors that respond to different wavelength regions, the chromaticity coordinates of a particular color can be determined by normalizing each of the color-matching functions so that:

$$x = \frac{X}{X+Y+Z}$$

$$y = \frac{Y}{X+Y+Z}$$

$$z = \frac{Z}{X+Y+Z} = 1 - x - y.$$

Since the $z = 1 - x - y$, it is only necessary to quote the quantity of two of the reference stimuli to define a color since the three quantities x, y, z are always added to a sum of 1 ($x + y + z = 1$) [8, 39]. Therefore, the color ratios X, Y, Z in a light source are represented by the so-called (x, y) chromaticity coordinates [40].

Color temperature (Kelvin) is defined as the absolute temperature at which a blackbody radiator must be operated to have a chromaticity equal to that of the light source [8, 40]. The light of an incandescent bulb is thermal radiation and the bulb is very close to an ideal blackbody radiator, so its color temperature is the actual temperature of the filament. Other light sources, such as fluorescent lamps and LEDs, emit light by ways other than thermal radiation. Therefore, color temperature values associated with these sources are referred to as correlated color temperatures (T_c) because they are not the actual temperatures of the source, but rather exhibit chromaticity coordinates that resemble the color temperature of a blackbody. A low color temperature indicates a warmer (orange-red) colored light source, while a high color temperature appears to be a colder (bluish) light source. As an illustration, the Planckian locus with exemplified color temperatures and its location in the CIE diagram is portrayed in Figure 1.5 [8, 41, 42]. The chromaticity coordinates and correlated color temperature (T_c) were measured by a Gigahertz-Optik HCT99D optometer. The detachable optometer detector was inserted inside the sample compartment of the spectrofluorophotometer and chromaticity measurements were obtained as samples were excited by the xenon lamp source. A total of three chromaticity and color temperature measurements were taken for each sample, and the values reported in this investigation were the average of the three measurements.

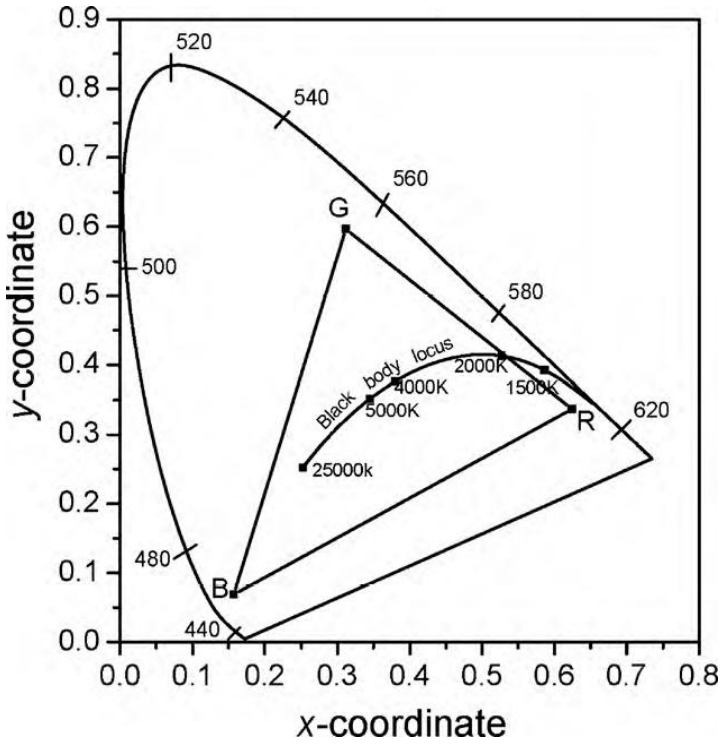

Figure 1.5. The CIE chromaticity diagram showing blackbody locus (R, G, B = coordinates of a cathode ray tube) [8, 41, 42].

1.3. Results and Discussion

1.3.1. XRD of phosphor powders. Figure 1.6(a) shows the XRD profiles of undoped $CaWO_4$ and $Ca_{0.96}W_{0.99}Mo_{0.01}O_4$**:**$0.01Tm^{3+}$, $0.005Tb^{3+}$, $0.005Eu^{3+}$, $0.02Na^{+}$ both annealed at 900 ºC. For reference, the JCPDS Card 41-1431 for $CaWO_4$ is shown in Figure 1.6(b). It can be seen that all diffraction peaks of the doped and undoped samples agree well with JCPDS 41-1431 standard data of scheelite phase $CaWO_4$. Since there are no impurity peaks or notable peak shifts, it can be assumed that the substitution of Mo^{6+}, Ln^{3+}, and Na^{+} ions has been accomplished without causing any structural change to the $CaWO_4$ lattice. The peaks in the XRD spectra are sharp and intense confirming that a highly crystalline single-phased $CaWO_4$ phosphor has been successfully synthesized by the Pechini sol-gel method.

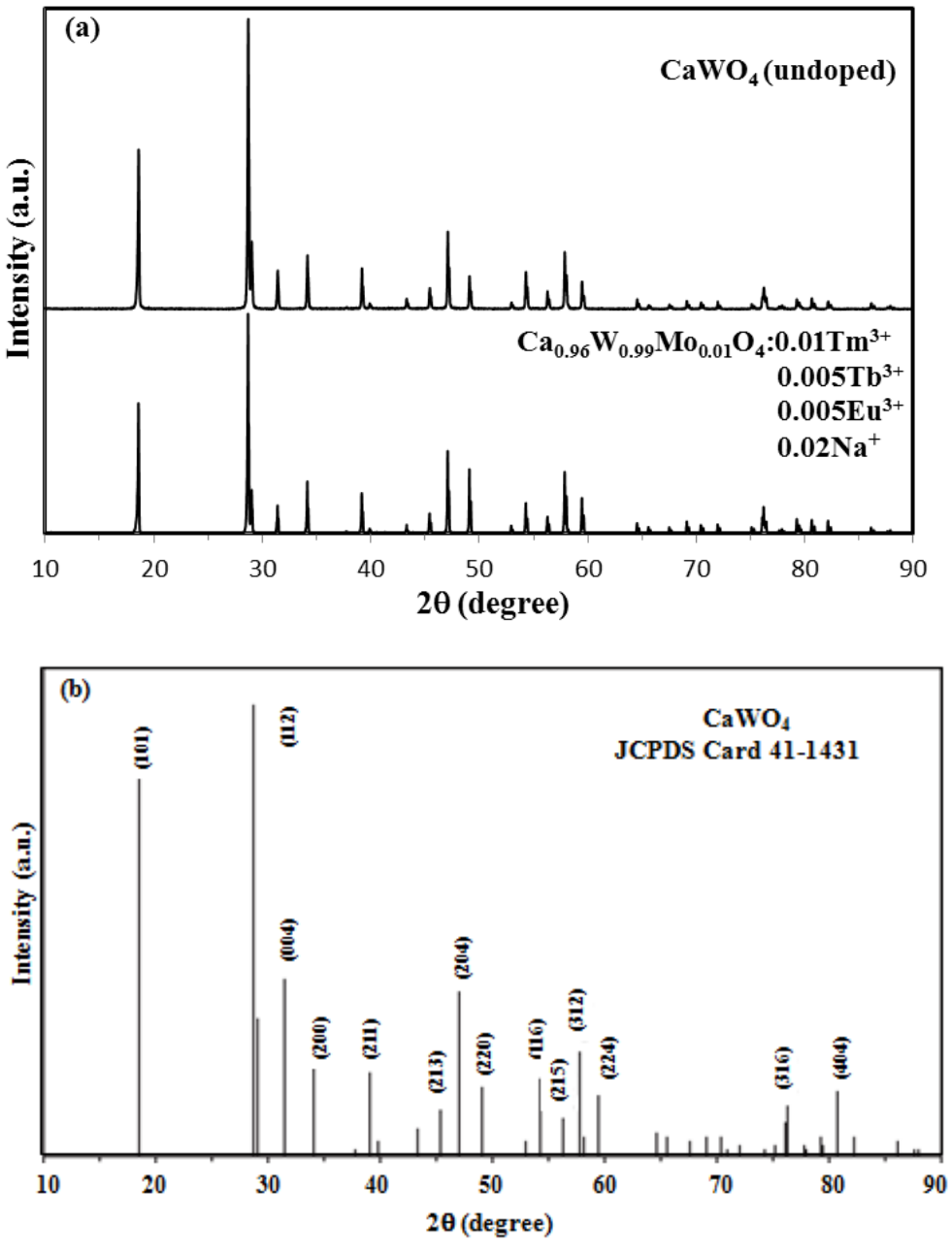

Figure 1.6. (a) X-ray diffraction patterns for undoped $CaWO_4$, $Ca_{0.96}W_{0.99}Mo_{0.01}O_4$**:**$0.01Tm^{3+}$, $0.005Tb^{3+}$, $0.005Eu^{3+}$, $0.02Na^{+}$, and (b) JCPDS Card 41-1431 data for $CaWO_4$.

The incorporation of Ln^{3+} ions into the $CaWO_4$ lattice without direct charge compensation often leads to decreased emission intensity due to the excess O_2 captured by the host. Nevertheless, it has been previously reported that replacing $2Ca^{2+}$ ions with $1Ln^{3+} + 1M^{+}$

(M^+ = alkaline ion) provides an alternative route for charge compensation and optimizes the emission intensity [43-46]. Since the ionic radius of most Ln^{3+} ions (0.87–1.11 Å) is slightly smaller than Ca^{2+}; their substitution is expected to cause contraction in the sub-lattice structure around the Ln^{3+} ions. This contraction creates distortions with oxygen-deficient sites becoming energy traps that can also decrease the emission intensity. The lattice distortions induced by Ln^{3+} doping can be partially compensated by the inclusion of slightly larger alkaline M^+ ions. Since the ionic radius of Na^+ (1.18 Å) is only slightly larger than Ca^{2+} (1.12 Å), the inclusion of Na^+ should compensate both for the excess charge of Ln^{3+}, and the ionic radii distribution around the Ln^{3+} ions. Therefore, Na^+ was selected as the compensating alkaline ion in this investigation.

1.3.2. SEM analysis. For comparison purposes, undoped $CaWO_4$ and $CaMoO_4$ phosphors were both fabricated via the Pechini sol-gel method. The morphologies of the phosphor powders were examined by SEM. The typical morphological photographs are shown in Figures 1.7 and 1.8. In Figure 1.7(a), the undoped $CaWO_4$ consists of well-defined cubical shaped particles with moderate agglomeration. Under higher magnification (Figure 1.7(b)), it can also be seen that the crystallites exhibit a variety of particle sizes ranging from 0.3–1.5μm. On the other hand, Figures 1.7(c) and (d) show that the undoped $CaMoO_4$ exhibits significantly large grains (the largest of all samples) with a high degree of agglomeration. Even though particles as small as 1 μm are seen attached to the particle surface, the images reveal dominant formations of large closely-packed grains with sizes ranging from 5–10 μm. The dramatic increase in grain size is likely due to the melting point of $CaMoO_4$ (1468 °C) being considerably lower than that of $CaWO_4$ (1620 °C) [47].

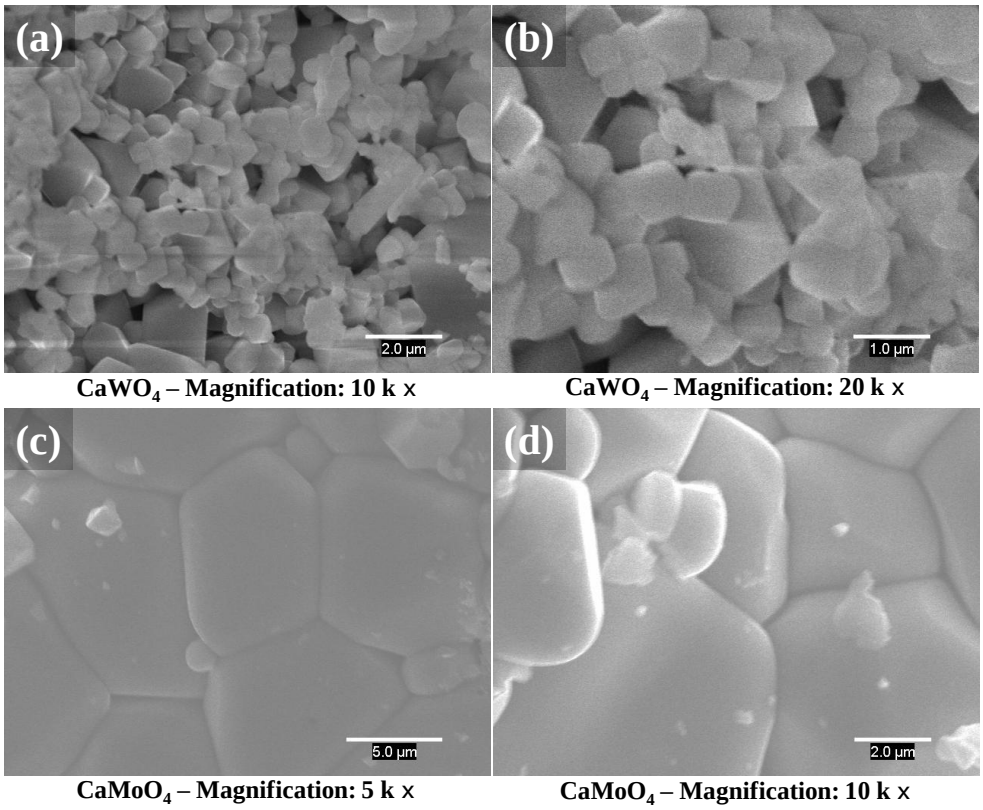

Figure 1.7. SEM images of $CaWO_4$ (a, b) and $CaMoO_4$ (c, d) under different magnifications.

The $CaWO_4$:Mo ($CaW_{1-x}Mo_xO_4$) powders in Figure 1.8(a) exhibit the most uniform particle size distribution with the average size between 2–3 μm. The textural properties appear to be slightly more spherical than undoped $CaWO_4$, while also resembling the larger $CaMoO_4$ particles by their pronounced agglomeration and smooth crystallite edges (Figure 1.8(b)). As seen in Figure 1.8(c), the $CaWO_4$:Mo, Tm^{3+}, Tb^{3+}, Eu^{3+} powder exhibits very similar particle sizes to $CaWO_4$:Mo in the range of 2–3 μm. However, under higher magnification in Figure 1.8(d), it is evident that their morphologies exhibit sharp and well-defined crystallite edges similar to the undoped $CaWO_4$ powders.

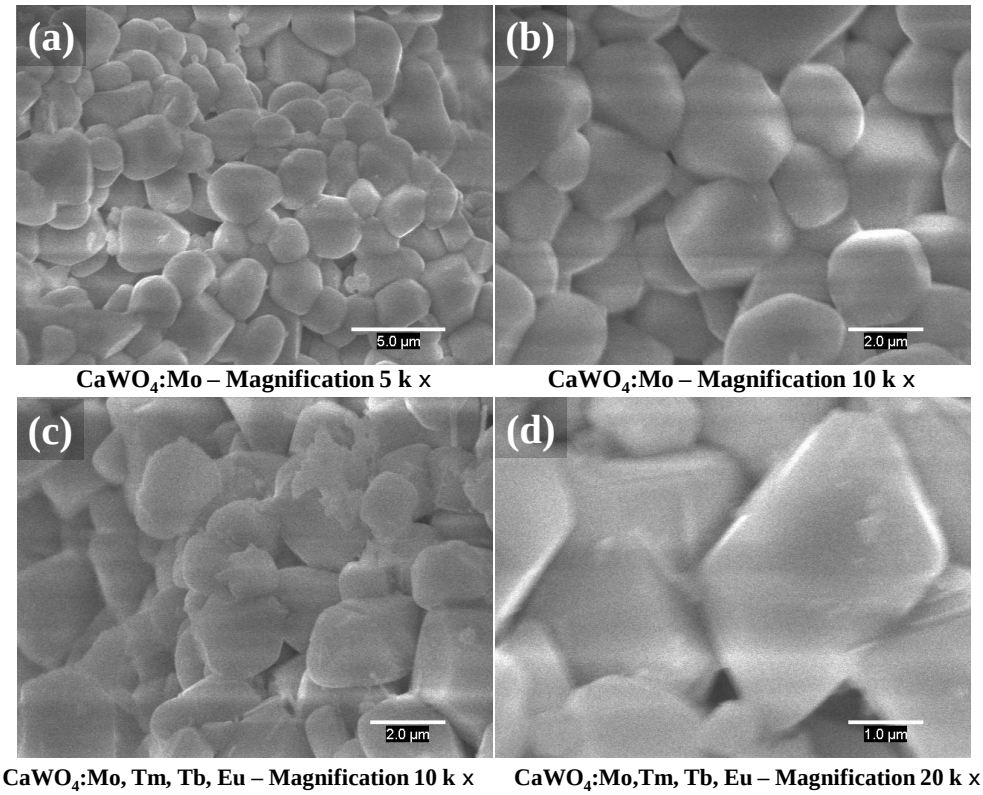

Figure 1.8. SEM images of $CaWO_4$:Mo (a, b) and $CaWO_4$:Mo, Tm^{3+}, Tb^{3+}, Eu^{3+} (c, d) under different magnifications.

1.3.3. Photoluminescent properties of $CaW_{0.99}Mo_{0.01}O_4$ host. The PL spectra of the undoped $CaWO_4$ and $CaMoO_4$ hosts are shown in Figure 1.9. The excitation spectra shown in Figures 1.7(a) and (c) correspond to that of $CaWO_4$ and $CaMoO_4$, and were monitored at 430 and 495 nm, respectively. The excitation spectrum of $CaWO_4$ consists of an intense band with a maximum at 258 nm which is ascribed to a charge transfer (CT) from the oxygen (O_{2p}) ligand to the central tungsten ($W_{t_{2g}}$) atom within the WO_4^{2-} group. Likewise, the $CaMoO_4$ excitation band at 290 nm arises from a ligand to metal CT within the MoO_4^{2-} group. Figures 1.9(b) and (d) show the emission spectra of WO_4^{2-} and MoO_4^{2-} systems excited at 260 and 290 nm, respectively. Both samples exhibit broad emissions with maxima at 427 and 495 nm, respectively. The WO_4^{2-} emission shown in Figure 1.9(b) also exhibits a well-defined shoulder at ~375 nm which is

attributed to WO_3 Shottky defects [3]. In comparison to WO_4^{2-}, the emission maximum of MoO_4^{2-} is red-shifted to 495 nm and exhibits a very broad shoulder at lower energy around 560 nm, which can also be attributed to oxygen-deficient MoO_3 surface defects [4].

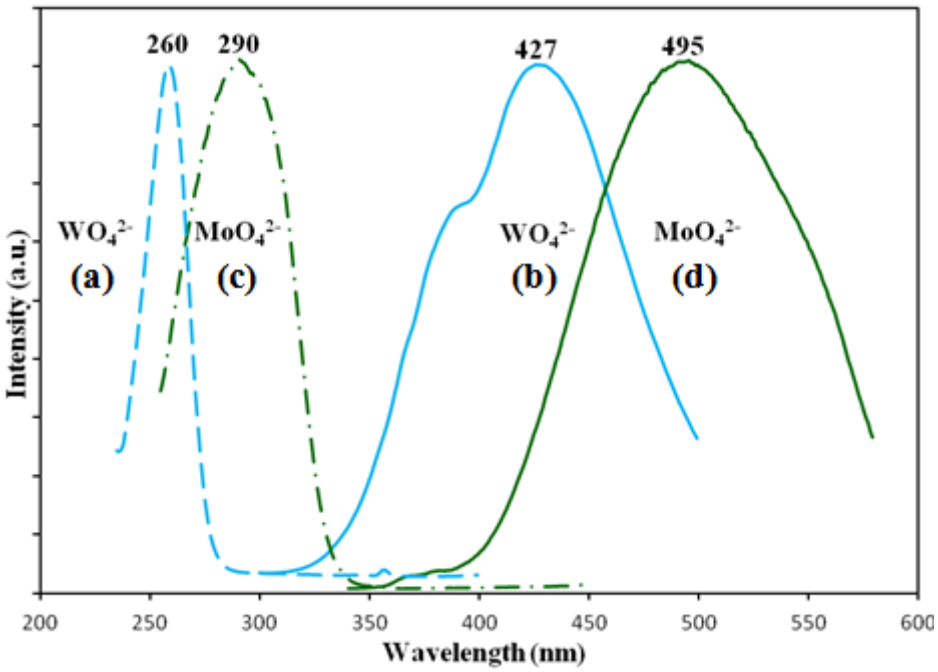

Figure 1.9. PL spectra of undoped $CaWO_4$ and $CaMoO_4$ (a, b, and c, d, respectively); Excitation spectra were obtained by monitoring at (a) 430 nm and (c) 495 nm. Emission spectra were obtained by excitation at (b) 260 nm and (d) 290 nm.

The comparison of Figures 1.9(a) and (c), clearly indicates that the doping of MoO_4^{2-} groups into the $CaWO_4$ lattice could expand the excitation range of the host, and also could result in tunability of its emission. Moreover, the lanthanide contraction effect permits the ionic radii of W (0.42 Å) and Mo (0.41 Å) in a four-fold coordination to be exceptionally similar, resulting in an ideal substitution of the MoO_4^{2-} groups into the $CaWO_4$ lattice.

Figure 1.10 shows the emission spectra of $CaWO_4$ doped with 1 mol% Mo ($CaW_{0.99}Mo_{0.01}O_4$). As the excitation wavelength increases systematically from 250 to 275 nm, the emission maximum shifts from 439 to 485 nm, corresponding to an overall shift of ~2160

cm^{-1}. The shift in the emission maximum is a result of the varying contribution of the two emitting WO_4^{2-}/MoO_4^{2-} groups under different excitation wavelengths. The inset of Figure 1.10 shows the excitation spectra monitored at 430, 450, and 495 nm. When monitored at 430 nm, the WO_4^{2-} CT band overlaps with the MoO_4^{2-} CT band which exhibits a well-defined shoulder at ~280 nm. The overall spectral profile is extended to ~315 nm.

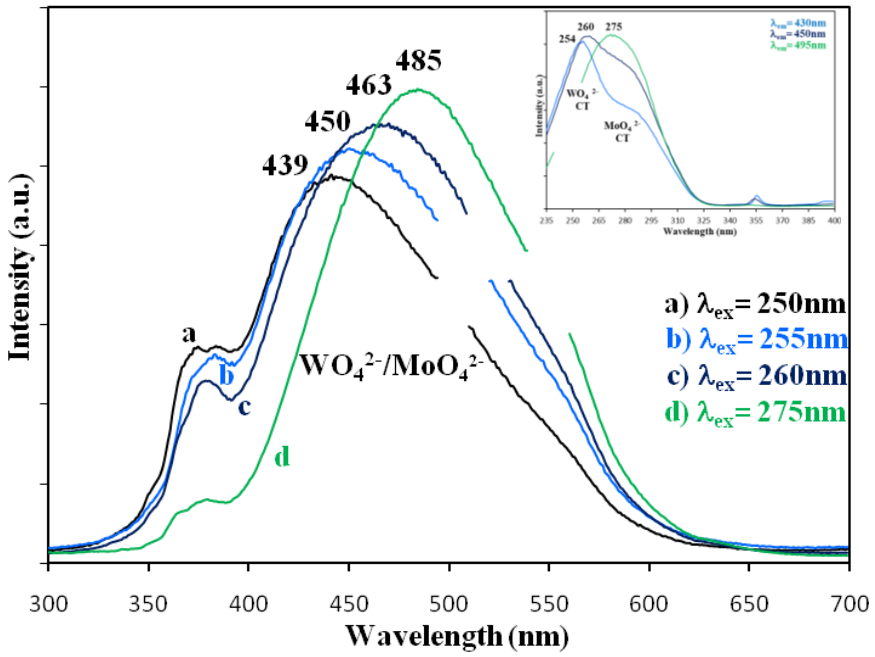

Figure 1.10. Room temperature emission spectra of $CaW_{0.99}Mo_{0.01}O_4$ under excitation wavelengths (a) 250, (b) 255, (c) 260, and (d) 275 nm (to avoid 2nd order effect to the PMT tube, spectral regions between 495-560 nm were bypassed).

Moreover, when monitored at 450 nm the excitation bands of the two groups exhibit comparable intensities. As the monitoring emission wavelength moves closer to the MoO_4^{2-} maximum at 495 nm, the MoO_4^{2-} excitation band becomes dominant. A characteristic feature in this system is that the usable excitation range of the WO_4^{2-} CT band is extended by the contributing excitation band of the MoO_4^{2-} groups within the $CaWO_4$ host. Furthermore, the emission profile is tuned by increasing the excitation wavelength from 250-280 nm.

The potential for WO_4^{2-} to transfer energy to MoO_4^{2-} within the current system has been noted, but the extent of energy migration was not specifically evaluated in this work. It is important to remark that earlier reports on a similar mixed scheelite-powellite ($CaWO_4$-$CaMoO_4$) series indicated the possibility of nonradiative energy transfer from WO_4^{2-} to MoO_4^{2-}. However, the observance of a significant enhancement in the MoO_4^{2-} CT band at the expense of attenuated emission of WO_4^{2-}, required a concentration of at least 10 mol% Mo [48]. The MoO_4^{2-} CT band was also reported to be dominant in $CaWO_4$:Mo microspheres when concentrations exceeded 10 mol% Mo [33].

1.3.4. Emission spectra of $CaW_{0.99}Mo_{0.01}O_4$:Tm^{3+}, Tb^{3+}, Eu^{3+}. Figure 1.11 shows the emission spectra of the $Ca_{0.96}W_{0.99}Mo_{0.01}O_4$:0.01$Tm^{3+}$, 0.005$Tb^{3+}$, 0.005$Eu^{3+}$, 0.02$Na^{+}$ phosphor under excitation at λ = (a) 250, (b) 260, and (c) 280 nm. In Figure 1.11(a), it can be seen that the WO_4^{2-} emission is significantly quenched relative to the undoped samples shown in Figures 1.9 and 1.10. As a result, the sharp *f–f* transitions are dominant in Figure 1.11. The weak bands in the UV region (350-375 nm) arise from the inherent host defects mentioned in the previous section. The characteristic emissions of Tm^{3+} at 455 and 476 nm are ascribed to the $^1D_2 \rightarrow {}^3F_4$ and $^1G_4 \rightarrow {}^3H_6$ electronic transitions, respectively. The Tb^{3+} emissions at 488 and 545 nm correspond to the $^5D_4 \rightarrow {}^7F_6$ and $^5D_4 \rightarrow {}^7F_5$ transitions, respectively. The higher energy bands occurring at 382, 414, and 439 nm also belong to the Tb^{3+} ion, but originate from the higher excited state transitions $^5D_3 \rightarrow {}^7F_J$ (J = 6, 5, 4), respectively. These transitions in particular are not common and are observed due to the low vibration energies of the host WO_4^{2-} groups (911, 807, and 428 cm^{-1} for ν_1, ν_3, ν_2 modes, respectively) [34]. The multiphonon relaxation of WO_4^{2-} is not able to bridge the gap between the higher $^5D_3$ and $^5D_4$ energy levels of Tb^{3+} completely, allowing the observance of these weak emissions.

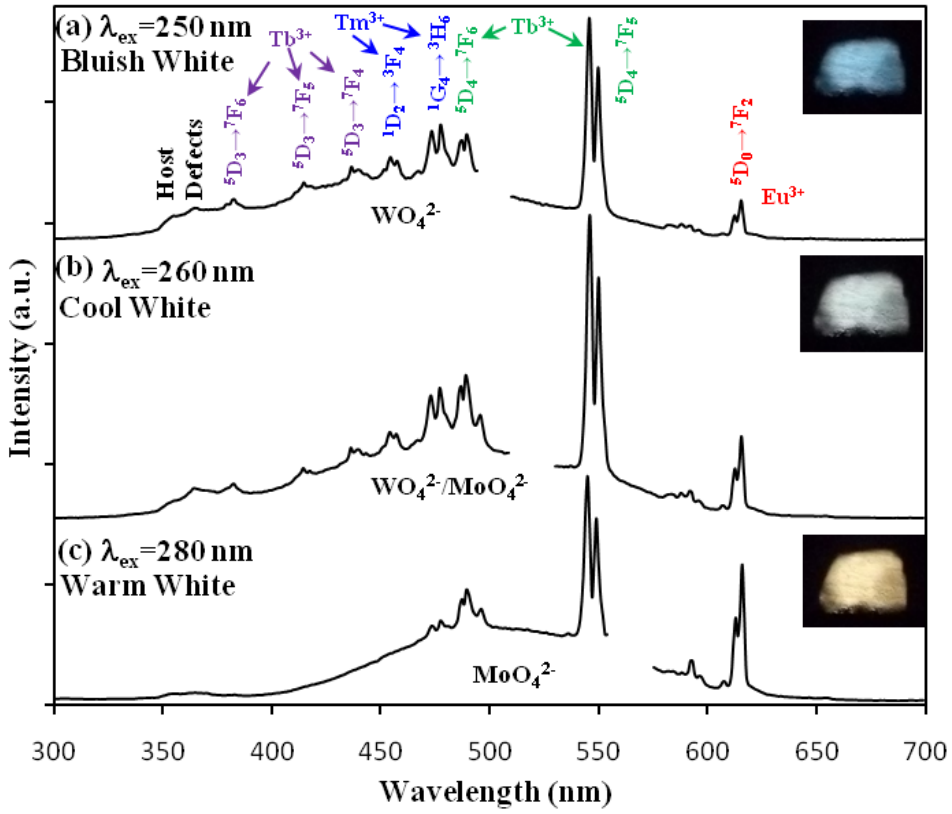

Figure 1.11. Room-temperature emission spectra of $Ca_{0.96}W_{0.99}Mo_{0.01}O_4$:0.01$Tm^{3+}$, 0.005$Tb^{3+}$, 0.005$Eu^{3+}$, 0.02$Na^{+}$ under excitation wavelengths (a) 250, (b) 260, and (c) 280 nm (to avoid 2nd order effect to the PMT tube, spectral regions between 500-575 nm were bypassed).

The region between 580–595 nm exhibits a combination of weak bands that belong to the $^5D_4 \rightarrow {}^7F_4$ transition of Tb^{3+}, and the $^5D_0 \rightarrow {}^7F_{0-1}$ magnetic dipole transitions of Eu^{3+}. The red emission of Eu^{3+} observed at 616 nm is due to the hypersensitive $^5D_0 \rightarrow {}^7F_2$ electric dipole transition. Since this transition dominates the Eu^{3+} emission, it is indicative that Eu^{3+} is substituted at Ca^{2+} sites that lack inversion symmetry. As shown in Figure 1.12(a), the Ca^{2+} ions have eight oxygen neighbors; four with bond lengths of 0.244 nm and the other four at 0.248 nm, forming a distorted cube [49]. Since the tetragonal structure of $CaWO_4$ corresponds to space group $I4_1/a$, the substituted Mo^{6+}, Ln^{3+}, and charge compensating Na^{+} ions are expected to occupy sites with $\boldsymbol{S}_4$ point symmetry [49]. As illustrated in Figure 1.12(b), the crystallographic

sites of the dopants are in agreement with the XRD patterns of Figure 1.6(a), which previously confirmed that their inclusion did not alter the phase of the $CaWO_4$ host.

Figure 1.11(b) shows the emission spectrum of the same sample under excitation at 260 nm. The prominent increase in the red and green emissions of Eu^{3+} and Tb^{3+} shifts the visual appearance from bluish white to cool white as shown in the inset of Figure 1.11(b). Furthermore, the quenched broad emission of the WO_4^{2-} host is now accompanied by weak emission from the MoO_4^{2-} groups. This is evident in the baseline region around the Tb^{3+} transition at 545 nm which is slightly elevated in comparison to Figure 1.11(a).

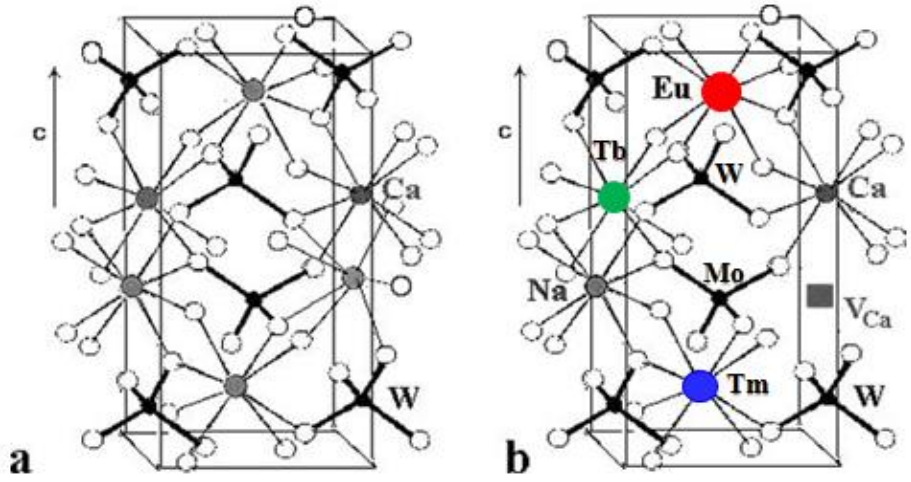

Figure 1.12. (a) Crystal structure of undoped $CaWO_4$, and (b) $CaWO_4$:Mo, Tm, Tb, Eu (charge compensation in the positions of Na^+ and Ca-vacancies is also suggested) [49].

Upon increasing the excitation to 280 nm, the quenched WO_4^{2-} emission is dominated by the broad MoO_4^{2-} emission band. Likewise, the red emission of Eu^{3+} is further enhanced shifting the visual color from cool white to warm white as shown in the inset of Figure 1.11(c). Concomitantly, the intensities of the major emission bands of Tb^{3+} (488 and 545 nm) and Tm^{3+} (476 nm) are reduced while emission from the higher excited states of Tb^{3+} ($^5D_3 \rightarrow {}^7F_J$, J = 6, 5, 4) and Tm^{3+} ($^1D_2 \rightarrow {}^3F_4$) are no longer visible. It can, thus, be assumed that the MoO_4^{2-} CT is not

as efficient as that of the WO_4^{2-} CT in generating emission from the higher $^5D_3$ and $^1D_2$ excited states of the Tb^{3+} and Tm^{3+} ions, respectively. As a result, a lower contribution from the blue region and a higher from the red region induces a warmer white color appearance. The overall energy exchange pathways are discussed more in subsequent sections.

1.3.5. Excitation spectra of $CaW_{0.99}Mo_{0.01}O_4:Tm^{3+}$, Tb^{3+}, Eu^{3+}. Figure 1.13 shows the excitation spectra of the Ln^{3+}-doped $Ca_{0.96}W0_{.99}Mo_{0.01}O_4$ host monitored at 455, 550, and 615 nm which were the selected transitions of Tm^{3+} ($^1D_2 \rightarrow {}^3F_4$), Tb^{3+} ($^5D_4 \rightarrow {}^7F_5$), and Eu^{3+} ($^5D_0 \rightarrow {}^7F_2$), respectively. The excitation spectra monitored at the Tm^{3+} and Tb^{3+} transitions, consist of broad bands with maxima at ~260 nm, and shoulders at ~282 nm which provide direct evidence of energy transfer from the WO_4^{2-} and MoO_4^{2-}groups, respectively. A unique situation of dual donor processes are exhibited where both groups are involved in the energy transfer to Tm^{3+} and Tb^{3+} ions within the $Ca_{0.96}W_{0.99}Mo_{0.01}O_4$ host. In contrast, the excitation spectra collected by monitoring the Eu^{3+} emission at 615 nm consist of a broad band at ~282 nm, which may imply that energy transfer takes place only from the MoO_4^{2-} group. Prior reports of a $CaMoO_4:Eu^{3+},Sm^{3+}$ system [50] showed a spectral overlap between the MoO_4^{2-} CT and a Eu^{3+}–O^{2-} CT band. The excitation within a Eu^{3+}–O^{2-} CT could permit an electronic transition from a 2*p* orbital of oxygen to an empty 4*f* orbital of Eu^{3+}, resulting in the observance of a broad excitation band [29, 44, 51]. In considering the red-shift in Figure 1.13, and the absence of the WO_4^{2-} CT; it can be deduced that the overlapping Eu^{3+}–O^{2-} and MoO_4^{2-}CT transitions in this system favor energy transfer to Eu^{3+} more than WO_4^{2-}. Nevertheless, in some instances the WO_4^{2-} and Eu^{3+}–O^{2-} CT bands have been reported to exist concurrently [44, 46].

Additional evidence of the Eu^{3+}–O^{2-} CT is supported by the inset of Figure 1.13, which shows the excitation spectra of $CaWO_4:0.01Tm^{3+}$, $0.005Tb^{3+}$, $0.005Eu^{3+}$, $0.02Na^+$ without the

inclusion of the Mo dopant. While energy transfer from WO_4^{2-} to Tm^{3+} and Tb^{3+} is clearly evident, the Eu^{3+} excitation band still exhibits a shifted maximum (259 vs. 274 nm), revealing the Eu^{3+}–O^{2-} CT state to be dominant while the WO_4^{2-} contribution is negligible.

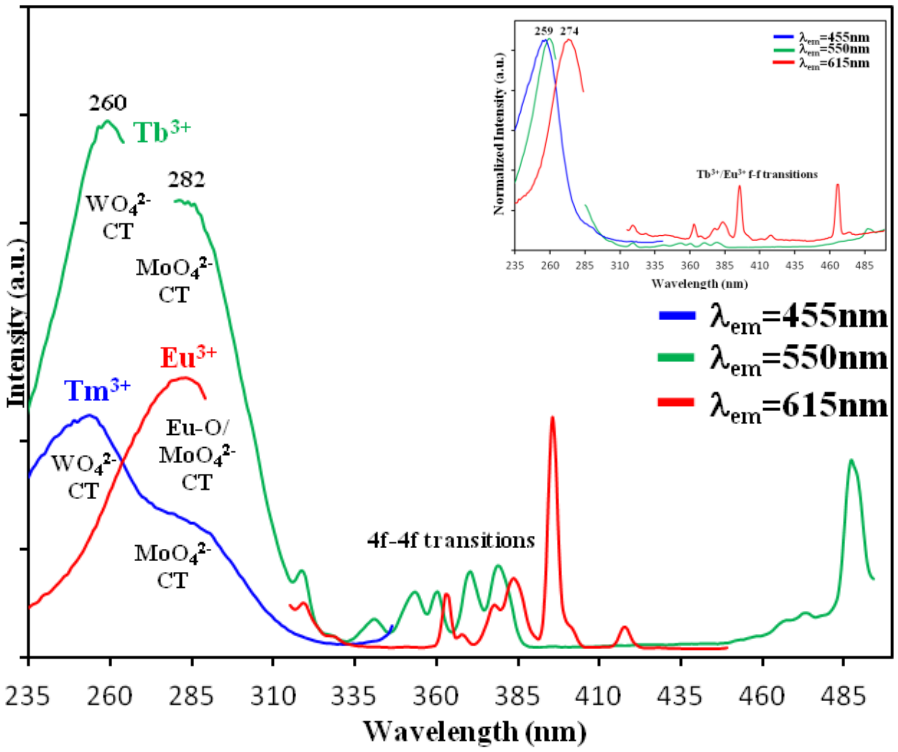

Figure 1.13. Room temperature excitation spectra of $Ca_{0.96}W_{0.99}Mo_{0.01}O_4$:0.01$Tm^{3+}$, 0.005$Tb^{3+}$, 0.005$Eu^{3+}$, 0.02$Na^+$ monitored at 455, 550, and 615 nm. The inset shows the excitation spectra of $CaWO_4$:0.01Tm^{3+}, 0.005Tb^{3+}, 0.005Eu^{3+}, 0.02Na^+ without the inclusion of Mo dopant.

The overall spectral profile of the Figure 1.13 inset appears to exhibit two independent excitation processes covering two regions. In the ~235–260 nm region the dominant feature is the CT within the WO_4^{2-} group, while in the ~265–300 nm region the dominant process is the Eu^{3+}–O^{2-} CT. Importantly, without the presence of Mo in this system, white light is only observed under one excitation wavelength (265 nm), while under longer wavelengths the red emission of Eu^{3+} is visually dominant. In the mixed $CaW_{0.99}Mo_{0.01}O_4$:Tm^{3+}, Tb^{3+}, Eu^{3+} system,

the presence of Mo extends the excitation region to where the blue and green emissions of Tm^{3+} and Tb^{3+} can still be blended with the red emission of Eu^{3+}, allowing the white light appearance to be tuned under longer excitation wavelengths.

1.3.6. Energy transfer pathways. Figure 1.14 illustrates the proposed energy transfer scheme based on the features of the emission and excitation spectra shown in Figures 1.11 and 1.13, respectively. The energy gap between the WO_4^{2-} excitation band and the $^3P_2$ (38,315 cm^{-1}) [30] excited state of Tm^{3+} is estimated to be ~445 cm^{-1}. Since the maximum phonon energy of the WO_4^{2-} host lattice is ~900 cm^{-1} [34, 52], this condition creates an ideal donor/acceptor energy match-up where the gap is easily bridged via one phonon-assisted process. The nonradiative (NR) energy transfer from WO_4^{2-} to the $^3P_2$ excited level of Tm^{3+} is efficient enough to generate emission from both the $^1D_2$ and $^1G_4$ excited states, albeit the emission from the $^1D_2$ level is much weaker (Figures 1.11(a) and (b)).

The energy gap comparison of the MoO_4^{2-} CT (34,480 cm^{-1}) indicates that the donor level matches well with the $^3P_0$ (33,710 cm^{-1}) excited level of Tm^{3+}; thereby, the energy gap of ~770 cm^{-1} can also promote energy transfer via one phonon-assisted process. However, the overall efficiency of the energy transfer from MoO_4^{2-} appears to be reduced in comparison to WO_4^{2-}. As a result, emission from the higher $^1D_2$ level is absent (Figure 1.11(c)). The emission from the lower $^1G_4$ level is also weak when compared to the emission profiles in Figures 1.11(a) and (b), confirming that the energy transfer from the MoO_4^{2-} CT to Tm^{3+} is less efficient than energy transfer from the WO_4^{2-} CT.

A similar excitation mechanism is observed in the energy transfer process to the Tb^{3+} ion. In Figure 1.14, it can be seen that the WO_4^{2-} CT has a good match with the ^5K_J levels of Tb^{3+} located at ~37,880 cm^{-1}. Hence, energy transfer is likely to these levels from the WO_4^{2-} CT state.

The donor/acceptor gap is estimated to be ~880 cm^{-1} which can easily be bridged by the assistance of one phonon. The analysis of Figure 1.14 suggests that a highly efficient energy transfer process takes place from WO_4^{2-} since the acceptor Tb^{3+} ion emits from both the $^5D_3$ and $^5D_4$ levels. Indeed, the $^5D_4 \rightarrow {}^7F_5$ (545 nm) transition of Tb^{3+} exhibits the most intense band in Figure 1.11(b) when energy is pumped from both the WO_4^{2-} and MoO_4^{2-} CT states.

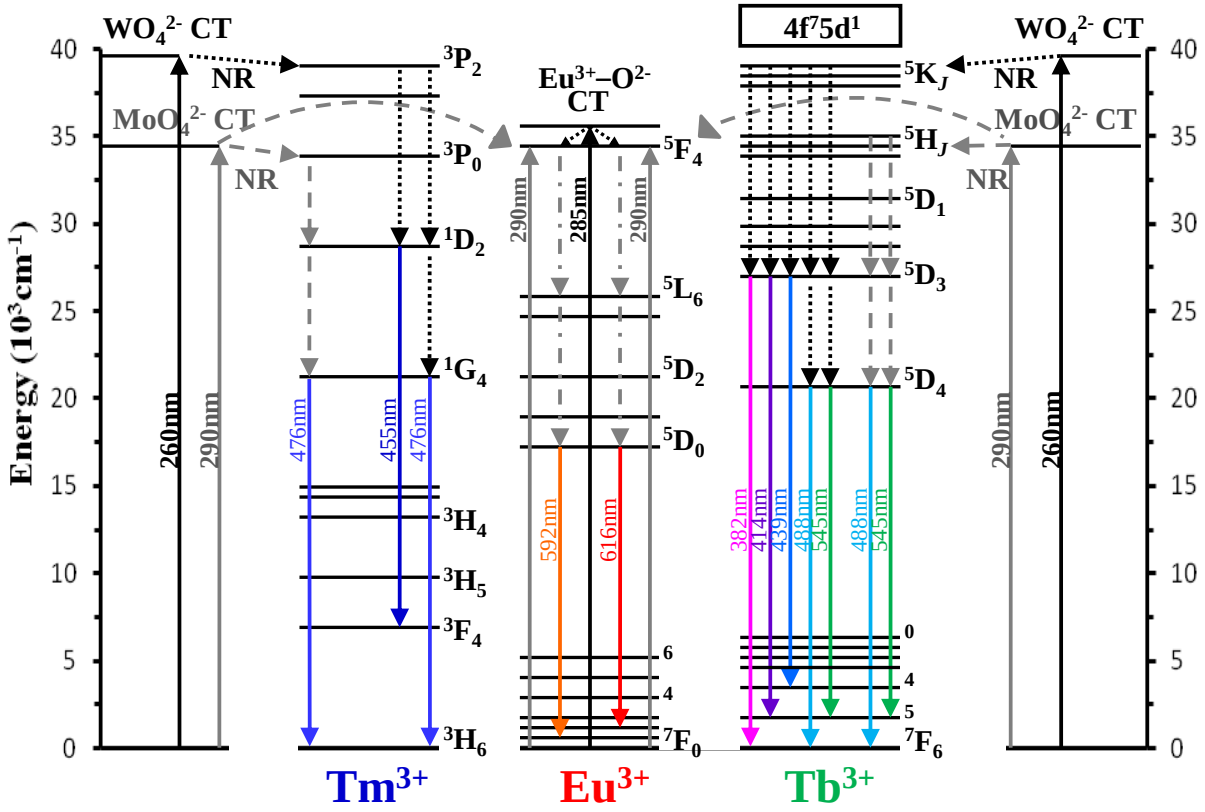

Figure 1.14. Energy transfer pathways in $Ca_{0.96}W_{0.99}Mo_{0.01}O_4$:0.01$Tm^{3+}$, 0.005$Tb^{3+}$, 0.005$Eu^{3+}$, 0.02$Na^+$.

Comparatively, the ^5H_J levels of Tb^{3+} are also in vicinity to be pumped by the MoO_4^{2-} CT. However, the overall efficiency of the energy transfer is lower than WO_4^{2-}, similar to that observed in the Tm^{3+} scenario. This conclusion is based on the following observations from Figure 1.11(c): (1) the decreased emission intensity of the $^5D_4 \rightarrow {}^7F_6$ (488 nm) and $^5D_4 \rightarrow {}^7F_5$ (545 nm) transitions, (2) the slight increase of the MoO_4^{2-} emission intensity, and (3) the absence

of the high-energy transitions from $^5D_3 \rightarrow {}^7F_J$ (J = 6, 5, 4). Unfavorably, instrumental limitations restricted our ability to conduct lifetime measurements in the short wavelength UV regions (< 300 nm), which would have provided a clear understanding of the energy transfer efficiency.

As mentioned in earlier sections, the energy transfer from WO_4^{2-} to Eu^{3+} appears to be negligible. The broad excitation band observed in Figure 1.13 when monitoring the Eu^{3+} *f–f* emission is assignable to contributions from both the Eu^{3+}–O^{2-} and the MoO_4^{2-} CT transitions. Figure 1.14 demonstrates how both transitions undergo NR relaxation from the $^5F_4$ (34,400 cm^{-1}) level leading to the characteristic emissions of Eu^{3+}. The absence of the WO_4^{2-} CT band is indicative that the red-shifted excitation band in Figure 1.13 can be assigned to the dominant Eu^{3+}–O^{2-} and MoO_4^{2-} CT states, which consequently enable the observation of warm white light under longer excitation wavelengths.

1.3.7. CIE chromaticity and color temperature. Figure 1.15 portrays the chromaticity coordinates (x, y) and correlated color temperatures (T_c) of the $Ca_{0.96}W_{0.99}Mo_{0.01}O_4$:0.01$Tm^{3+}$, 0.005$Tb^{3+}$, 0.005$Eu^{3+}$, 0.02$Na^+$ phosphor under varied excitation wavelengths. It can be clearly seen that under excitation at 255 and 260 nm, the respective chromaticity coordinates (0.3003, 0.3281) and (0.3316, 0.3520) exhibit an excellent closeness to the D_{65} sunlight white point (0.3127, 0.3290). Moreover, the high T_c values under these excitation wavelengths make the phosphor suitable for cool and natural-WLEDs. When the excitation wavelengths are changed to 265 and 280 nm, the T_c values are lowered significantly to color temperatures appropriate for warm-WLEDs. Ultimately, the simultaneous emission of the red, green, and blue-emitting Ln^{3+} ions in the $CaWO_4$ system is improved by the inclusion Mo. The MoO_4^{2-} groups not only contribute additional emission, but also extend the excitation wavelengths under which the white light emission is perceived, promoting tunable levels of chromaticity. Since warm white light

appeals to human emotion for use in home lighting, and cool white light is preferred for public lighting [11], the tunability of this single-phased emitting phosphor exhibits promising applications for SSL.

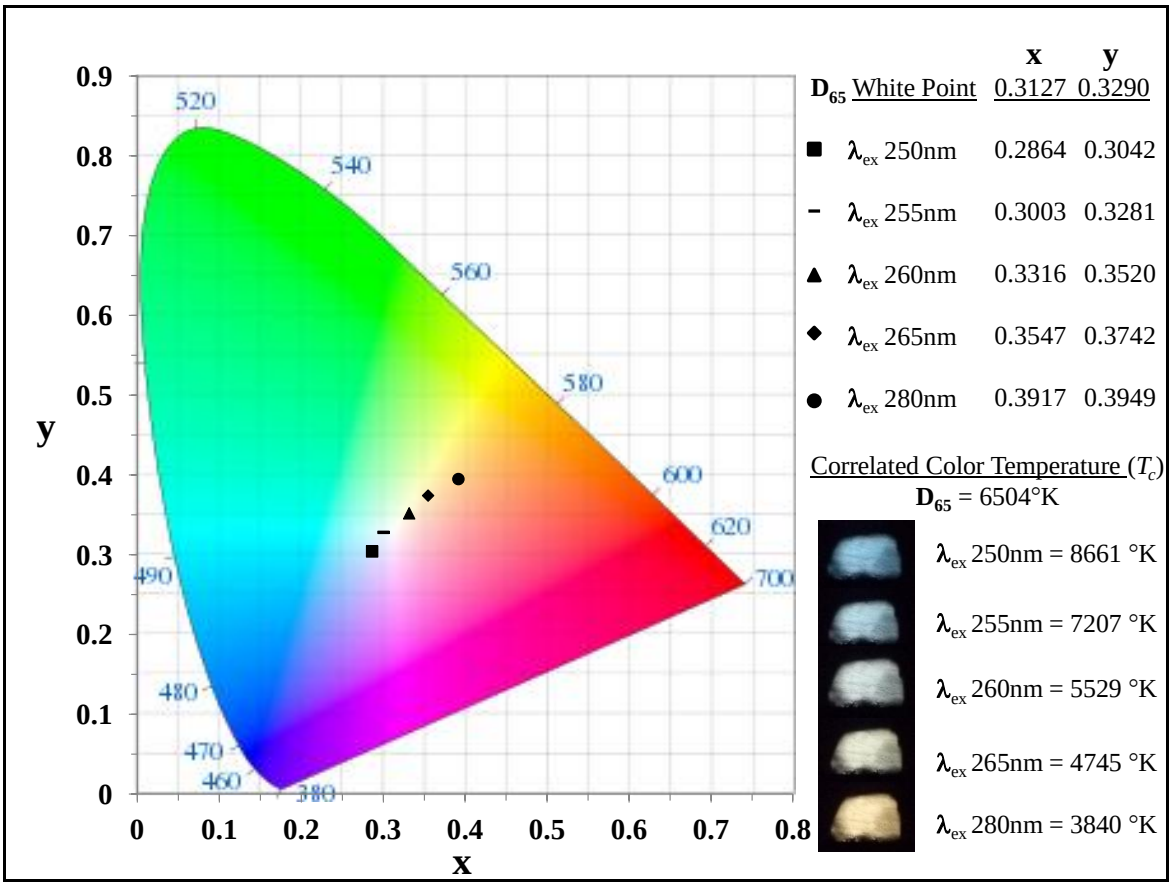

Figure 1.15. CIE chromaticity diagram for $Ca_{0.96}W_{0.99}Mo_{0.01}O_4$:0.01$Tm^{3+}$, 0.005$Tb^{3+}$, 0.005$Eu^{3+}$, 0.02$Na^{+}$ showing (*x*, *y*) coordinates, correlated color temperature, and photographs of phosphor powder under various excitation wavelengths.

1.4. Conclusion

A single-phased white light-emitting $CaW_{1-x}Mo_xO_4$:Tm^{3+}, Tb^{3+}, Eu^{3+} phosphor has been successfully synthesized via a Pechini sol-gel process. The Mo^{6+}, Ln^{3+}, and compensating Na^{+} ions were uniformly incorporated into the scheelite phase $CaWO_4$ host. The excitation and emission spectra reveal that introducing Mo into the $CaWO_4$ lattice extends the excitation range,

and induces a dual energy transfer from WO_4^{2-} and MoO_4^{2-} groups to Tm^{3+} and Tb^{3+} ions. The energy transfer schemes have been proposed. Due to the different excitation mechanisms of Eu^{3+}, the resulting white light emission is made tunable from cool white to warm white by changing the excitation wavelength as confirmed by chromaticity coordinates. By application to shortwave UV-LEDs, the $CaW_{1-x}Mo_xO_4$: Tm^{3+}, Tb^{3+}, Eu^{3+} phosphor is a suitable candidate for both cool and warm WLEDs.

CHAPTER 2

Enhanced Emission of a $Ca_{1-2x}WO_4:Eu_xM_x$ ($M = Na^+$) Phosphor and its Potential Application in Blue/Red LEDs for Space Greenhouses

2.1. Introduction

One application that has attracted the attention of NASA, is utilizing LEDs to stimulate photosynthesis for plants in space greenhouses. LEDs have offered several appealing benefits for space applications including low levels of thermal radiation that may heat the plant growing area, no hot electrodes, no high-voltage ballasts, and a very long operating life in comparison to fluorescent lamps [53]. In particular, red and blue LEDs have been useful light sources to drive photosynthesis due to their output near the peak absorption regions of chlorophyll.

Plants efficiently absorb blue and red light to initiate their photosynthetic reactions, while reflecting green light, hence owing to their green appearance [54]. Undoubtedly, various plant species require different ratios of blue/red light. For instance, a study performed by Goins *et al.* indicated that the wheat species, *triticum aestivum*, completed its life cycle under red LEDs alone, but larger plants and greater amounts of seed were produced in the presence of red LEDs supplemented with quantities of blue light [55]. Incidentally, in major plants such as soybean, grass, and clover, Warrington *et al*. reports that blue-biased conditions enhance the concentrations of amino acids (particularly aspartic and glutamic acids) and proteins; whereas, red-biased sources increase the concentrations of soluble sugars and starch in the leaf tissue [56]. Indeed, literature reports have demonstrated how various plant species require different ratios of blue/red light in order to optimize their photosynthetic processes.

Currently, NASA is seeking to optimize the photosynthesis of plants in space greenhouses by employing numerous units of red and blue LEDs [57]. These LEDs have to be

arranged in specific orientations to yield the desired ratio of blue/red light. However, different driving currents are often required for each red and blue LED, which complicates energy usage, and possibly makes the method more expensive than necessary. As a remedy, if each blue and red LED were replaced by a single LED that emits blue/red light simultaneously; we believe this will significantly reduce the number of operating LEDs needed for the desired blue/red ratio.

In an attempt to satisfy this condition, a calcium tungstate phosphor doped with Eu^{3+} and Tm^{3+} ions ($CaWO_4$:Tm^{3+}, Eu^{3+}) was synthesized for potential LED application. This phosphor material emits ratios of blue and red light that can be tuned by varying the excitation wavelength. In addition, this investigation revealed that the simultaneous inclusion of Na^+ ions provides suitable charge compensation that significantly enhances the emission of Eu^{3+}, while reducing the amount of dopant needed for sufficient light output. For comparison, the effects of Na^+ co-doping on the optical properties of $CaWO_4$:Eu^{3+} were evaluated firstly, then Tm^{3+} was later added to examine the tunability of the blue and red emissions.

2.2. Experimental

2.2.1. Sample synthesis. In this synthesis the Pechini Sol-gel method was adapted from references [34, 35], and the detailed procedure is described below. Three phosphor systems were synthesized all together. The first two systems comprised a series of samples that upheld the following formulas: $Ca_{1-x}WO_4:Eu_x$ and $Ca_{1-2x}WO_4:Eu_xM_x$ ($M = Na^+$). In the third system, one sample was prepared that adhered to the general formula $Ca_{1-2x-2y}Tm_xEu_yNa_{x+y}WO_4$. This system was selected as a representative example to illustrate the synthetic procedure. In proportion to Ca^{2+}, the doping concentrations of Ln^{3+} and Na^+ ions were 0.5 mol% Tm^{3+}, 1.5 mol% Eu^{3+}, and 2 mol% Na^+. To obtain 0.5 g of doped phosphor product, a typical experiment involved dissolving 443 mg of ammonium tungstate ($(NH_4)_{10}W_{12}O_{41}\cdot 5H_2O$) in a water-ethanol (*V/V=3:1)*

solution containing 667 mg of citric acid ($C_6H_8O_7$) as the chelating agent for the metal ions. The molar ratio of metal ions to citric acid was 1:2. In a separate beaker, 166 mg of calcium carbonate (99.99% $CaCO_3$), 2 mg of sodium carbonate (99.5% Na_2CO_3), 1.6 mg of thulium oxide (99.99% Tm_2O_3) and 4.5 mg of europium oxide (99.99% Eu_2O_3) were dissolved in 5 mL of dilute nitric acid (70% HNO_3) under heated magnetic stirring until the solution became clear. The excess HNO_3 was removed by evaporation at ~100° C until crystallization of metal-nitrate salts was apparent, and deionized water was added to dissolve the nitrate salts. The resulting metal-nitrate solution was adjusted to a pH of 2–3, and then added to the flask containing the metal-citrate solution. Polyethylene glycol (PEG; molecular weight = 200) was added as a cross-linking agent with a final concentration of 0.20 g mL^{-1}. The solution mixture was covered and stirred magnetically for 1 h at 70 ºC, and ultrasonically for 20 min to yield a highly transparent sol. The sol was transferred to an open beaker and placed in a water bath at 65 ºC for 8 h where it was concentrated to a viscous gel. The gel was immediately placed in an oven at 100 ºC for 30 min to drive off remaining solvents until a color change to transparent yellow was observed. While hot, the reduced viscosity of the gel allowed easy transfer to a porcelain crucible where annealing took place at 900 ºC for 2 h with a heating rate of 1 ºC min^{-1}. The phosphor powders were allowed to cool naturally in the furnace and were characterized immediately.

2.2.2. PL and chromaticity. The PL studies were conducted on the basis of excitation and emission spectra using a Shimadzu 5301 spectrofluorophotometer equipped with a 150 W xenon lamp excitation source (Figure 1.3). All spectroscopic measurements were performed at room temperature. The spectroscopic data were acquired and managed by HyperRF software (Version 1.57). The data were later exported to Microsoft Excel for manipulation and figure preparation. The chromaticity coordinates and correlated color temperature (T_c) were measured

by a Gigahertz-Optik HCT99D optometer. The detachable optometer detector was inserted inside the sample compartment of the spectrofluorophotometer and chromaticity measurements were obtained as samples were excited by the xenon lamp source. The samples were prepared for chromaticity measurements by spreading the phosphor powders onto a double-sided adhesive strip mounted on a microscope slide. For each phosphor sample, the average of three measurements was used to represent the chromaticity coordinates reported in this investigation.

2.3. Results and Discussion

2.3.1. Emission spectra of $Ca_{1-x}WO_4:Eu_x$ and $Ca_{1-2x}WO_4:Eu_xM_x$ ($M = Na^+$). To optimize the emission intensity of Eu^{3+} within the $CaWO_4$ host lattice, 6 samples were prepared with varied Eu^{3+} concentrations of 5, 10, and 20 mol%. Figure 2.1(a) shows the emission spectra of 3 samples in the absence of Na^+ ions adhering to the general formula $Ca_{1-x}WO_4:Eu_x$, while Figure 2.1(b) demonstrates the emission spectra of 3 samples corresponding to the formula $Ca_{1-2x}WO_4:Eu_xM_x$ ($M = Na^+$) where the Na^+ concentration is matched with that of Eu^{3+}. The major bands of Figure 2.1(a) comprise of the host emission at ~430 nm due to the $^1T_2 \rightarrow {}^1A_1$ transition of the WO_4^{2-} complex, and the $^5D_0 \rightarrow {}^7F_J$ ($J = 0,1,2$) transitions of Eu^{3+}. The observance of the weak emission line (~538 nm) from the higher $^5D_1$ excited level of Eu^{3+} is observed due to the low vibration energy of the WO_4^{2-} groups [35, 58]. Also present is a prominent band at ~375 nm due to oxygen-deficient WO_3 groups. Although these groups do not contribute to the visible emission of the phosphor, they are important markers to indicate the level of lattice distortions arising from the doping of Eu^{3+}. In Figure 2.1(b), it can be clearly observed that the inclusion of Na^+ significantly enhances the emission intensity of Eu^{3+}. In particular, the $^5D_0 \rightarrow {}^7F_2$ transition dominates the phosphor emission even at the lowest concentration (5 mol%) of Eu^{3+}. Whereas in Figure 2.1(a), at least 20 mol% was required for the $^5D_0 \rightarrow {}^7F_2$ transition to surpass the host

emission maximum, albeit at the expense of prevalent distortions revealed by the dominating WO_3 emission. Figure 2.1(b) also reveals that the inclusion of Na^+ maintains the structural integrity of the lattice by reducing the intensity of WO_3 defects. The quenched intensity of the WO_4^{2-} host emission with increasing Eu^{3+} concentration is observed in both Figures 2.1(a) and (b), which is indicative of non-radiative energy transfer from WO_4^{2-} to Eu^{3+} ions. However, in Figure 2.1(b), the energy transfer process appears to be more efficient since the 20 mol% Eu^{3+} concentration quenches the WO_4^{2-} emission to levels close to the baseline of the spectrum. Moreover, this observation also conveys that the energy transfer efficiency and pathways are also improved by the inclusion of Na^+.

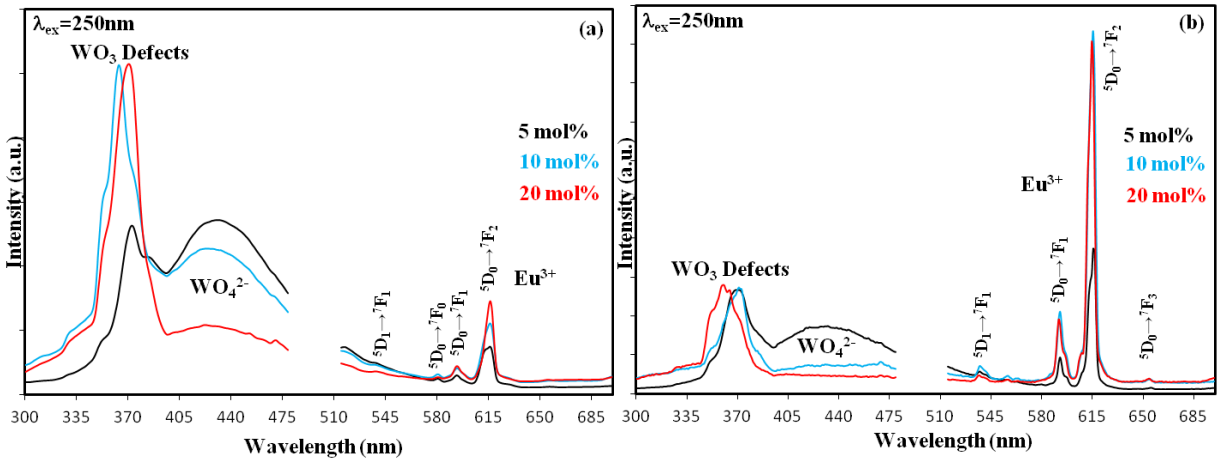

Figure 2.1. (a) Emission spectra of $Ca_{1-x}WO_4:Eu_x$ with increasing Eu^{3+} concentrations, and (b) Emission spectra of $Ca_{1-2x}WO_4:Eu_xM_x$ (M = Na^+) with increasing Eu^{3+} concentrations (to avoid 2nd order effect to the PMT tube, spectral regions between 480-515 nm were bypassed).

2.3.2. Excitation spectra of $Ca_{1-x}WO_4:Eu_x$ and $Ca_{1-2x}WO_4:Eu_xM_x$ (M = Na^+). The excitation spectra shown in Figures 2.2(a) and (b) were obtained by monitoring the emission at 615 nm corresponding to the dominant $^5D_0 \rightarrow {}^7F_2$ transition of Eu^{3+}. In Figure 2.2(a), the broad band observed for the 5 mol% concentration is the result of at least two contributions: The Eu^{3+}–O^{2-} CT band (~270 nm), and the energy transfer from the WO_4^{2-} CT to the Eu^{3+} ions (~245 nm).

These two bands become more resolved when the concentration is increased to 10 and 20 mol%. The resolution of the two bands is primarily due to an apparent red-shift of the Eu^{3+}–O^{2-} CT as the concentration increases, while the position of the WO_4^{2-} CT band remains mostly unaffected. The weak bands from 315-330 nm are attributed to the *f–f* transitions of Eu^{3+}. The excitation spectra of Figure 2.2(b) exhibit remarkably different profiles when Na^+ is incorporated. Although the excitation profile of the 5 mol% sample is similar to the 5 mol% profile of Figure 2.2(a), the profiles with higher concentrations lack the presence of the WO_4^{2-} CT band. Instead, the Eu^{3+}–O^{2-} CT appears to be the dominant route of excitation for the Eu^{3+} ions.

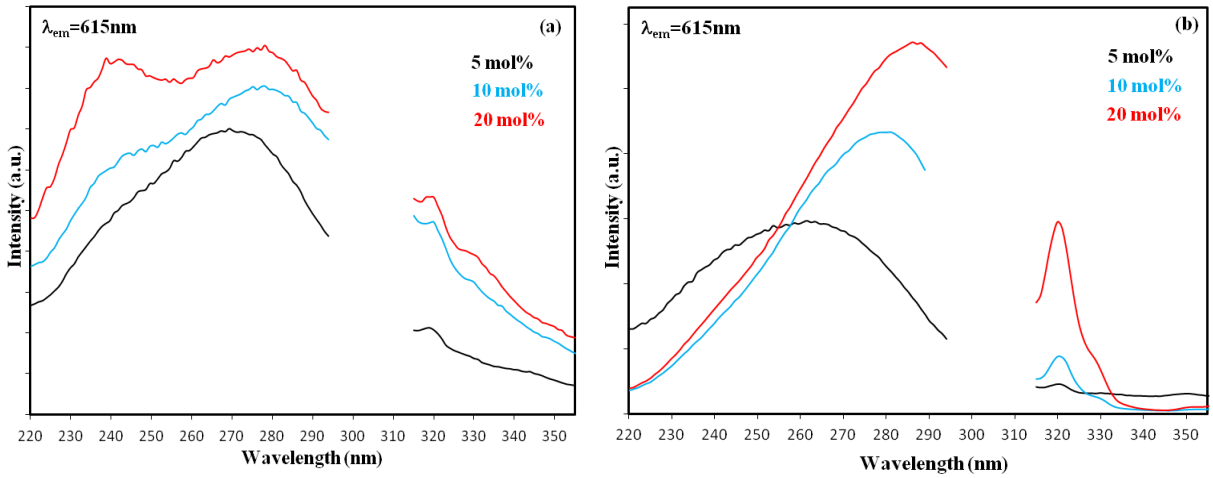

Figure 2.2. (a) Excitation spectra of $Ca_{1-x}WO_4:Eu_x$ with increasing Eu^{3+} concentrations, and (b) Excitation spectra of $Ca_{1-2x}WO_4:Eu_xM_x$ (M = Na^+) with increasing Eu^{3+} concentrations (to avoid 2nd order effect to the PMT tube, spectral regions between 295-315 nm were bypassed).

When Eu^{3+} is incorporated into the $CaWO_4$ host, the excess charge of Eu^{3+} ions to Ca^{2+} ions requires a necessary charge balance. Without charge balance the host has to capture O_2 from the air to compensate. The captured O_2 inevitably becomes a source of energy traps that reduce the emission intensity, and prohibit Eu^{3+} from entering the lattice to occupy Ca sites. Instead, impurity phases such as Eu_2O_3 and CaO may exist in the phosphor [44]. However, when the

excess charge of Eu^{3+} is compensated by the presence of an alkali metal ion such as Na^{+}, the substitution for every $2Ca^{2+}$ ions is balanced by $1Eu^{3+}$ and $1Na^{+}$ ion. This process allows Eu^{3+} to freely occupy more Ca sites which creates more emission centers that ultimately increase emission intensity. Moreover, since more Eu^{3+} ions would reside in sites with 8-fold coordination to oxygen, this will likely promote a long range increase in covalency of the Eu–O bond. Importantly, an increase in covalency would reduce the energy of the charge transfer band [46], hence possibly explaining the red-shift observed in Figure 2.2(b).

2.3.3. Wavelength tunability of blue/red-emitting $Ca_{1-2x-2y}Tm_xEu_yNa_{x+y}WO_4$. By careful analysis of the excitation properties featured in Figures 2.2(a) and (b), it was realized that the WO_4^{2-} host and the Eu^{3+} ions could be excited by two distinct wavelength regions. The blue-emitting host is excited by UV from ~240–265 nm, and the red emission of Eu^{3+} is excited from ~265–285 nm. This feature allows the ratios of blue/red light to become tunable by varying the excitation wavelength. At the same time, it was anticipated that there would exist a mid-region in the excitation spectrum at ~265 nm where the blue and red emissions would exhibit comparable intensities, demonstrating the potential for a phosphor material to simultaneously emit blue and red light in ratios that can be tuned by excitation wavelength. To confirm these postulations, an additional $CaWO_4$ sample was doped with 1.5 mol% of Eu^{3+}. The lower Eu^{3+} concentration relative to what was used in Figures 2.2(a) and (b) was chosen to prevent significant quenching of the host emission while also keeping the level of distortions to a minimum. Furthermore, with the inclusion of Na^{+}, it was expected that the enhanced emission of Eu^{3+} would still render a red emission with suitable intensity. Lastly, Tm^{3+} was co-doped at 0.5 mol% to supplement the blue emission of the WO_4^{2-} host. The charge compensation effects of Na^{+} on the Tm^{3+} emission were not evaluated in this work.

For comparison, Figure 2.3(a) shows the absorption spectrum of chlorophyll *b* as reported by Du *et al*. [59]. Figure 2.3(b) shows the emission spectra of the $Ca_{0.96}Tm_{0.005}Eu_{0.015}Na_{0.02}WO_4$ phosphor as the excitation wavelength is increased. As observed in Figure 2.3(b), the WO_4^{2-} host emission shows a systematic decrease in intensity as the excitation wavelength increase, while the red emission of Eu^{3+} appears unchanged. In fact, a closer analysis of the Eu^{3+} emission in Figure 2.4 shows a slight increase of intensity with increasing excitation wavelength.

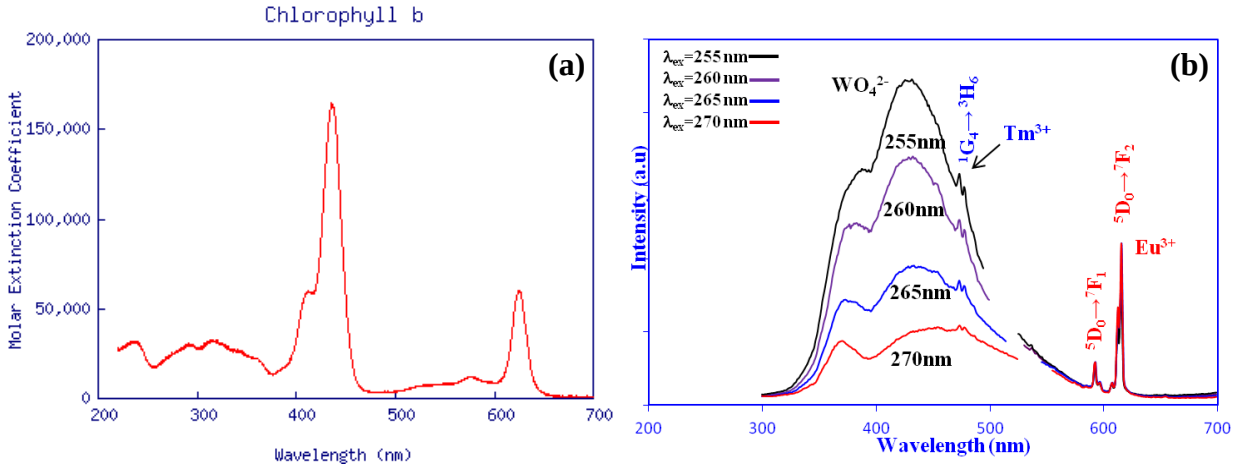

Figure 2.3. (a) Absorption spectrum of chlorophyll *b* dissolved in diethyl ether solvent [59], and (b) Emission spectra of $Ca_{0.96}Tm_{0.005}Eu_{0.015}Na_{0.02}WO_4$ under different excitation wavelengths (to avoid 2nd order effect to the PMT tube, spectral regions between 500-550 nm were bypassed).

Just as anticipated, the phosphor under excitation at 265 nm exhibits comparable intensities of blue and red light. Furthermore, when comparing Figures 2.3(a) and (b), it is clearly evident that the $Ca_{0.96}Tm_{0.005}Eu_{0.015}Na_{0.02}WO_4$ phosphor is emitting wavelengths that closely match the absorption regions required for photosynthesis. Hence, this demonstrates for potential for employment in a plant growth LED that emits blue and red light simultaneously.

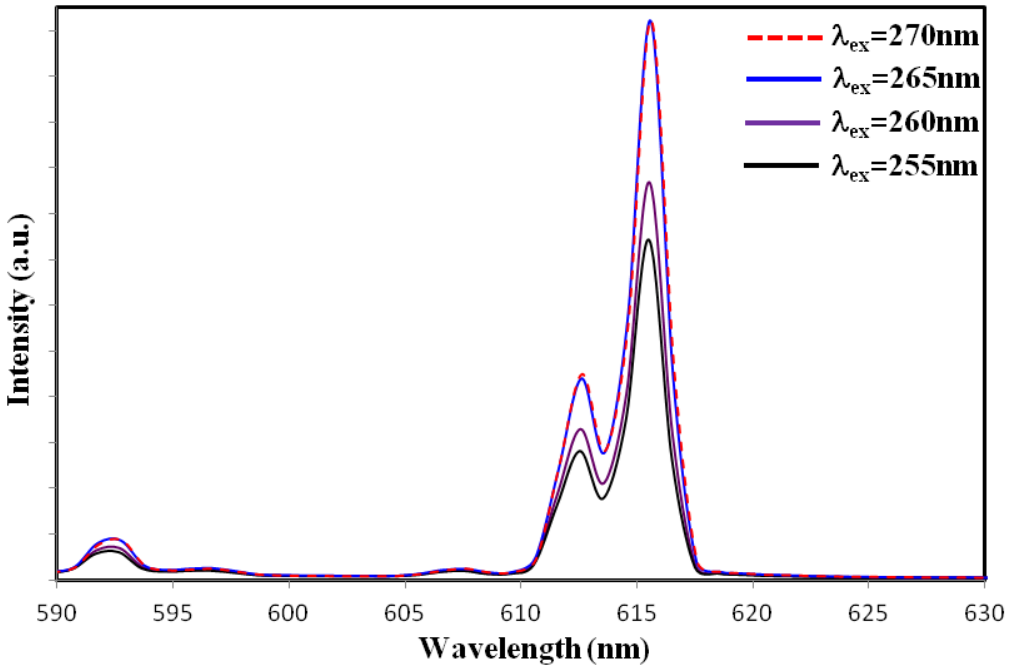

Figure 2.4. Magnified emission region extracted from Figure 2.3(b) showing increase of Eu^{3+} emission with increasing excitation wavelength of $Ca_{0.96}Tm_{0.005}Eu_{0.015}Na_{0.02}WO_4$ phosphor.

2.3.4. Excitation properties of blue/red-emitting $Ca_{1-2x-2y}Tm_xEu_yNa_{x+y}WO_4$. The occurrence of two excitation processes taking place within the same system permits the blue and red emissions to be tuned to desired ratios. Figure 2.5 shows the excitation profiles obtained by monitoring the host emission at 430 nm, and the Eu^{3+} emission at 615 nm. The WO_4^{2-} CT band at ~250 nm is clearly present when λ_{em} = 430 nm, but exhibits less contribution in the excitation of Eu^{3+} when λ_{em} = 615 nm. Instead, the excitation maximum at ~271 nm indicates that the Eu^{3+}–O^{2-} CT band is the dominant excitation route. Although energy transfer from WO_4^{2-} to Eu^{3+} in the current $Ca_{0.96}Tm_{0.005}Eu_{0.015}Na_{0.02}WO_4$ system cannot be completely discounted, the findings here demonstrate the influence of Na^+ ions on the excitation properties of Eu^{3+}. Unfavorably, instrumental limitations restricted the ability to conduct lifetime measurements in the short wavelength UV regions (< 300 nm), which would have provided a clearer understanding of energy transfer from WO_4^{2-}.

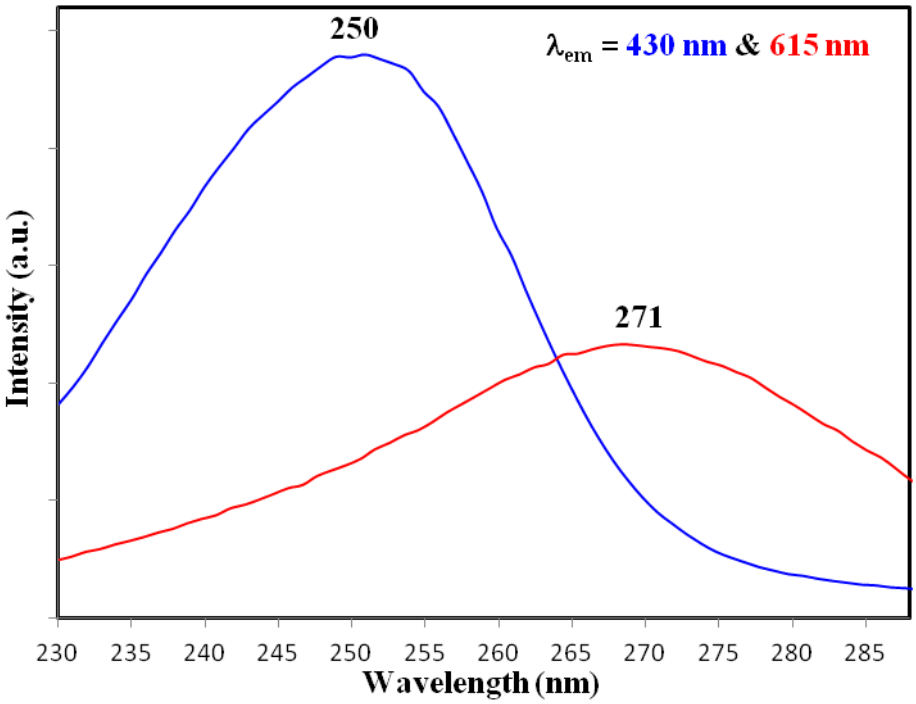

Figure 2.5. Excitation spectra of $Ca_{0.96}Tm_{0.005}Eu_{0.015}Na_{0.02}WO_4$ phosphor monitored at 430 nm (blue line) and 615 nm (red line).

2.3.5. Chromaticity characterization. The various ratios of blue and red light emitted by the $Ca_{0.96}Tm_{0.005}Eu_{0.015}Na_{0.02}WO_4$ phosphor were characterized by chromaticity coordinates plotted in the CIE diagram. Figure 2.6 depicts the chromaticity as the excitation wavelength was increased systematically from 250 to 285 nm. To demonstrate a high-quality trend, more excitation wavelengths were selected to excite the phosphor than were presented in the emission spectra of Figure 2.3(b). The slight incline of the trend towards the white region, is due the broadness of the WO_4^{2-} emission band. Nevertheless, the overall trend of the chromaticity agrees well with the emission spectra. The coordinates under excitation at 250 nm (0.24, 0.18) and 255 nm (0.26, 0.20) both reflect the dominant blue emission of the WO_4^{2-} host and Tm^{3+}. Upon excitation at 260 nm (0.29, 0.22) and 265 nm (0.34, 0.26), chromaticity coordinates enter the purple region demonstrating the appropriate mixing of the blue and red emissions as they exhibit

comparable intensities. The higher *x* coordinates under excitation at 275 nm (0.44) and 280 nm (0.46) support the dominant of red emission of Eu^{3+}. The deviation of the coordinates under excitation at 285 nm is likely attributed to the overall decreased emission of the phosphor as this excitation wavelength transcends away from both the WO_4^{2-} and Eu^{3+}–O^{2-} CT bands. Importantly, as the excitation wavelength increases, the progression of the chromaticity along the so called "line of purples," is an indication that specific ratios of blue and red light can be generated in this system. Since purple emission is not a monochromatic feature of light, it can only be observed by mixing the proper ratios of blue and red.

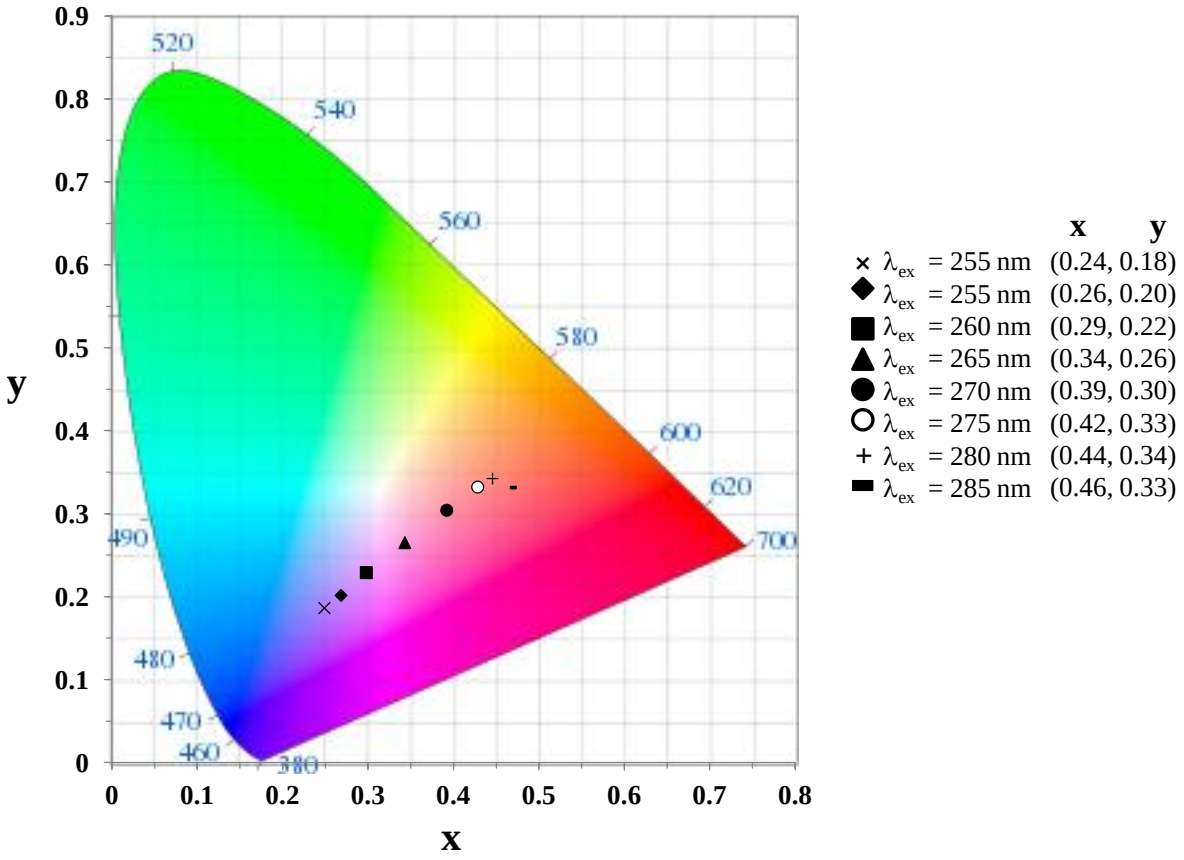

Figure 2.6. CIE chromaticity diagram of $Ca_{0.96}Tm_{0.005}Eu_{0.015}Na_{0.02}WO_4$ phosphor under different excitation wavelengths.

2.4. Conclusion

In this investigation, enhancement of the Eu^{3+} emission within a $CaWO_4$ host was attained by the co-doping of Na^+ ions. By comparing the emission and excitation properties of $Ca_{1-x}WO_4:Eu_x$ and $Ca_{1-2x}WO_4:Eu_xM_x$ ($M = Na^+$) phosphors, the charge compensation provided by Na^+ ions resulted in the following observations: (1) a significant increase of the $^5D_0 \rightarrow {}^7F_2$ transition of Eu^{3+}, (2) a reduction in intensity of the WO_3 defect emission bands, (3) an increase in the non-radiative energy transfer from the WO_4^{2-} host to Eu^{3+}, and (4) an increased red-shift of the Eu^{3+}–O^{2-} CT excitation band which became dominant over the WO_4^{2-} CT band.

In recognition that the inclusion of Na^+ influences the Eu^{3+}–O^{2-} CT excitation band to red-shift with respect to the position of the WO_4^{2-} excitation band, a $Ca_{0.96}Tm_{0.005}Eu_{0.015}Na_{0.02}WO_4$ phosphor was prepared to evaluate the possibility of tuning the blue and red emissions by varying the excitation wavelength. As confirmed by emission spectra, and the linear trend observed in the chromaticity diagram, the $Ca_{0.96}Tm_{0.005}Eu_{0.015}Na_{0.02}WO_4$ phosphor rendered tunable ratios of blue and red light.

The blue/red-emitting $Ca_{0.96}Tm_{0.005}Eu_{0.015}Na_{0.02}WO_4$ phosphor studied herein can offer a novel application for blue and red LED grow-lights designed for photosynthesis. The results presented here clearly confirm that the spectroscopic properties of the phosphor are well suited for chlorophyll absorption. In practice, if each blue and red LED in conventional grow lights were replaced by a single LED that emits blue/red light simultaneously; this significantly reduces the number of operating LEDs needed for the desired blue/red ratio. Ultimately, reducing the number of LED units needed to grow plants in space results in reduction of energy usage, and concurrently the cost of future missions.

CHAPTER 3

Photoluminescence of Natural Pink-Emitting $NaCa_2Si_4O_{10}F$ and its Conversion into a White Light Phosphor by Doping with Ce^{3+}, Tb^{3+}, and Mn^{2+} ions

3.1. Introduction

Recently, there has been an increased motivation to establish white light-emitting diodes (WLEDs) as the future light sources for general illumination [6, 8]. In certain parts of the world such as China, fluorescent lamps play a role in contributing ~75% of the mercury found in municipal solid waste due to the absence of well-developed recycling programs for fluorescent lamps [60]. Instead of relying on end-of-pipe attempts to solve the problem, elimination of mercury at the source can be achieved by the gradual transition to WLEDs, since mercury is not utilized in their operation. WLEDs are improving exponentially in terms of efficiency and color rendering properties by the fabrication of novel inorganic phosphors, and could be price-competitive in the near future [8].

The conventional WLED is based on coating a blue-emitting diode (InGaN) with a yellow-emitting phosphor, $Y_3Al_5O_{12}:Ce^{3+}$ (YAG:Ce). This system has been commercialized because it exhibits a high luminous flux and simple structure [61]. However, as stated in Chapter 1, major limitations with this method include the poor rendition of orange-red colors due to the lacking red component in the spectra. Moreover, this hinders the WLED to vividly reproduce the color appearance of red objects in museums, galleries, and the medical field. Likewise, the high color temperatures of $YAG:Ce^{3+}$-based WLEDs (CCT ≈ 7750 K) are often visually harsh and unappealing for private and home use [62, 63].

In attempts to remedy the shortcomings of $YAG:Ce^{3+}$-based WLEDs, efforts have been made [13, 64, 65] by employing the “three-converter” system for LEDs. This system applies

three different RGB-emitting phosphors to near-UV-LEDs. However, this route could not fully rectify the limitations of YAG:Ce because of high manufacturing cost and inadequate efficiency of the blue-emitting phosphor due to the strong reabsorption of the green and red phosphors [66]. Furthermore, systems that generate white light by combining several RGB phosphors can often become unstable with respect to input power [65]. For instance, increasing the current of the exciting LED can increase the level of reabsorption for one of the phosphors, causing the color-rending index to change with increasing current, thus eliminating the possibility of the WLED being coupled to dimming technology.

Currently, the efforts to improve the color-rending of WLEDs are now focused on employing UV-LEDs coated with single-phased phosphor materials [67, 68]. Single-phased phosphors are produced by doping sensitizer (donor) and activator (acceptor) ions into a single host matrix. The emission of light is generated and tuned by changing the relative concentration of either the donor or acceptor. Energy transfer from one ion species to another is an essential component to improving the efficiency and color rending of these phosphors. One important criterion for energy transfer to take place among several emitting centers is the extent at which the donor emission band overlaps with the acceptor absorption band. According to Dexter's theory [8, 69], the transfer probability, P_{DA}, between a donor (D) and acceptor (A) ion is given by:

$$P_{DA} = \frac{2\pi}{\hbar} |\langle D^*, A|H_{DA}|D, A^*\rangle|^2 \int g_D(E) g_A(E)\, dE \qquad (3.1)$$

where $|\langle D^*, A|H_{DA}|D, A^*\rangle|$ represent initial and final state, respectively; H_{DA} is the Hamiltonian of interaction and $\hbar$ is Planck constant; and $\int g_D(E) g_A(E)\, dE$ denotes the integral of spectral overlap between the donor and acceptor. When the donor and acceptor ions are close enough and

their wavefunctions are overlapped, the energy transfer mechanism from donor to acceptor can be an exchange interaction where the transfer probability $P_{ex}(R)$ is expressed by [69]:

$$P_{ex}(R) = \frac{2\pi}{\hbar} K^2 \exp\left(\frac{-2R}{L}\right) \int F_D(E) F_A(E)\, dE, \tag{3.2}$$

where K^2 is constant; R is the distance between the donor and acceptor; L denotes the average radius of the donor excited state and the acceptor ground-state; and the integrated section represents the spectral overlap.

Another important impact on the luminescence properties of phosphors is the minimum phonon energy of the host. The lower the phonon energy of the host, the lower the probability of non-radiative processes, and the higher the efficiency of the luminescence [70]. As reported by Gaft *et al.* [71], the minimum number of phonons required for a transition between states separated by an energy gap ΔE is given by:

$$p = \frac{\Delta E}{\hbar \omega_{max}}, \tag{3.3}$$

where $\hbar \omega_{max}$ is the maximum energy of optical phonons. With increased temperature, stimulated emission of phonons by thermal phonons increases the relaxation rate W according to:

$$W(T) = W(O)\,(1 + \bar{n}\,(\hbar \omega_{max}))^P, \tag{3.4}$$

where $\bar{n}$ is the average occupation number of phonons at energy $\hbar \omega_{max}$. The non-radiative relaxation in the doped ions are related to their excited-state population and are governed by the energy difference between the emitting level and next lower-level, separated by the number of phonons of the host. In the weak-coupling case such as for rare earth ions, the temperature dependence non-radiative rate is given by:

$$W(T) = \beta \exp\left[-(\Delta E - 2\, h\nu_{max})\, \alpha\right] \left([\exp(h\nu/kT) - 1]^{-1} + 1\right)^P, \tag{3.5}$$

where $p = \Delta E/h\nu$, ΔE the energy difference between the levels involved, α and β are constants, and ν_{max} the highest available vibrational frequency of the rare earth ion environment. Ultimately, this relation depends critically upon the ν_{max} of the host lattice [71].

Many inorganic phosphor hosts with low phonon energies have been recently reported to emit white light such as fluorides [72], phosphates [73, 74], borates [75], and silicates [76]. Among these, silicates were one of the first hosts fabricated into single-phased full-color emitting phosphors as reported in the earlier works of the Park group [16, 17, 77]. Silicates are desirable hosts due to their high chemical and physical stability, as well as their water-resistant properties [78]. Hence, the fabrication of a silicate-based phosphor will be the emphasis of this chapter.

The silicate system of interest, agrellite ($NaCa_2Si_4O_{10}F$), is a naturally occurring and rare mineral highly sought after by collectors due to its intense pink luminescence under mid-wave UV light. Being named in honor of the pioneering mineralogist Stuart Olof Agrell (1913-1996) of Cambridge, agrellite is mostly found in regionally metamorphosed agpaitic rock complexes of Villedieu Township, Quebec, Canada [79]. Early studies by Gittens *et al.*[80] rigorously determined the chemical composition, crystal structure, and infrared data of natural agrellite samples. Additionally, Ghose and Wan [81, 82] also reported that agrellite crystallizes as a triclinic crystal system in space group $P\bar{1}$ and cell dimensions: a = 7.759(2), b = 18.946(3), c = 6.986(1)Å, α = 89.88(2), β = 116.65(2), γ = 94.34(2)º and Z = 4. The most recent thorough analysis of agrellite's structural features was performed in 2002 [83]. Unfortunately, these earlier works did not report the photoluminescence properties of the agrellite system. Although Gittens *et al.* states in the manuscript that attempts to synthesize agrellite from oxide mixes failed at that time, to our knowledge no other reports of synthetic attempts have been in existence.

In this chapter, the photoluminescence properties of natural agrellite are investigated, and attempts to synthesize the silicate mineral by the sol-gel method are reported herein. Moreover, an attempt to replicate its pink emission under midwave UV excitation was also executed. As an additional investigation, the synthesized system was further converted into a white-light emitting phosphor by the co-doping of Ce^{3+}, Tb^{3+}, and Mn^{2+} ions where the quality of white light was tuned and optimized by varying the concentrations of the dopants.

3.2. Experimental

3.2.1. Sample preparation. The natural agrellite specimens were purchased from the Mineralogical Research Company (MRC) and were sampled originally from Kipawa County, Quebec, Canada. They were analyzed as purchased without further alteration. The phosphors were prepared by the sol-gel method reported previously [78, 84]. All chemicals and reagents were purchased from Sigma-Aldrich. The undoped sample was prepared according to the molecular formula, $NaCa_2Si_4O_{10}F$, while the attempt to synthesize agrellite adhered to the formula $NaCa_{1.97}Si_4O_{10}F$:0.005Ce^{3+}, 0.02Mn^{2+}, 0.0014Dy^{3+}, 0.0012Sm^{3+}. The concentrations of Dy^{3+} and Sm^{3+} were selected based on the chemical compositions (in wt. %) of natural agrellite previously reported by Gittens *et al.* [80]. The amounts of Ce^{3+} and Mn^{2+} were chosen based on the ratios which generated the closest match to the photoluminescence properties of agrellite. Six samples were prepared as the following: Four as $NaCa_{1.955-x}Si_4O_{10}F$:0.005$Ce^{3+}$, 0.04$Tb^{3+}$, $x$$Mn^{2+}$ (x = 0, 1, 2, and 3 mol%), One as $NaCa_{1.995}Si_4O_{10}F$:0.005Ce^{3+} for reference, and one optimized sample as $NaCa_{1.945}Si_4O_{10}F$:0.005Ce^{3+}, 0.035Tb^{3+}, 0.015Mn^{2+}.

3.2.2. Sample synthesis. To obtain 0.5 g of doped phosphor product, $NaCa_{1.945}Si_4O_{10}F$:0.005Ce^{3+}, 0.035Tb^{3+}, 0.015Mn^{2+} was selected as a representative example to illustrate the experimental process. Initially, 246 mg of calcium carbonate (99.99% $CaCO_3$), 67

mg of sodium carbonate (99.5% Na_2CO_3), and 16 mg of terbium oxide (99.99% Tb_4O_7) were dissolved in 5 mL of dilute nitric acid (70% HNO_3) under heated magnetic stirring until the solution became clear. The excess HNO_3 was removed by evaporation and then 4 mL of deionized water was added to dissolve the nitrate salts. At the same time, 5 mg of $Ce(NO_3)_3 \cdot 6H_2O$ and 95 mg of $Mn(NO_3)_2 \cdot 4H_2O$ were dissolved into the metal-nitrate solution and the pH was adjusted to ~1.0. Then, 20 mL of ethanol was added systematically. First, 10 mL of ethanol was added to the metal-nitrate solution and stirred for magnetically for 1 min. Then 33 μL (10% excess) of 2,2,2 trifluoroethanol (99% CF_3CH_2OH) was added followed by 5 mL of ethanol. Lastly, 1.15 mL of tetraethyl orthosilicate (98% $Si(OC_2H_5)_4$) was added followed by the remaining 5 mL of ethanol. The resulting solution was stirred with a magnetic stirrer for 1 h, and by sonication for 30 min at 50 ºC to obtain a clear homogeneous sol. The sol was then evaporated in a water bath at 60 ºC for 3 h until highly transparent gels formed. The gels were grinded and prefired at 500 ºC for 2 h in air, then fully ground and annealed at 900 ºC for 1 h in a weak reductive atmosphere of H_2–N_2 (5:95) gas to obtain final phosphor powders.

3.2.3. Structural characterizations by XRD. The X-ray powder diffraction (XRD) patterns of the synthesized phosphors were collected in the range of $5^o < 2\theta < 90^o$ using a Bruker D8 Advance X-ray diffractometer with a Cu Kα radiation source (λ=0.15418 Å). The voltage and current were maintained at 40 kV and 40 mA, respectively.

3.2.4. Fourier Transform-Infrared (FT-IR) characterization. The FT-IR spectra were measured with a Shimadzu IRPrestige-21 infrared spectrophotometer. The samples were prepared for measurement by employing the KBr pellet technique. The data collection was controlled and managed by IRSolution software version 1.30.

3.2.5. PL and chromaticity characterizations. The PL studies were conducted on the basis of excitation and emission spectra using a Shimadzu RF-5301 spectrofluorophotometer equipped with a 150 W xenon lamp excitation source (See Figure 1.3 for details). All spectroscopic measurements were performed at room temperature and data was managed by HyperRF software (Version 1.57). In some instances, emission spectra were also collected using a Photon Technology International (PTI) spectrometer (model-QM-7/SE) equipped with a high intensity xenon lamp source for excitation. The signal detection was accomplished with a PMT detector (model 928 tube) that was capable of both analog or digital (photon counting) modes. The data collection was controlled using the advanced FeliX32 fluorescence spectroscopic package. The chromaticity coordinates and correlated color temperature (T_c) were measured by a Gigahertz-Optik HCT99D optometer. The detachable optometer detector was inserted inside the sample compartment of the spectrofluorophotometer and chromaticity measurements were obtained as samples were excited by the xenon lamp.

3.2.6. Lifetime and quantum yield characterizations. The lifetime decay and time-resolved emission spectra were inspected using a PTI GL-3300 nitrogen laser with an excitation wavelength of 337.1 nm. Various time delays were utilized ranging from 100 μs to 20 ms. The excitation pulses from the nitrogen laser were guided to the sample compartment by means of a fibre optic cable. The solid powder samples were prepared and tightly-packed into quartz capillary tubes for the analysis. All decay data, best-fit curves, and lifetime calculations were executed by the FeliX32 software package.

The absolute PL quantum yield (QY) measurements on the solids were conducted using a PTI QM-40, PLQY ultrasensitive fluorimeter system containing a 6-inch integrating sphere (K-Sphere B) redesigned for enhanced measurement of quantum yields of solids, films, and

powders. The system includes dedicated quantum yield calculation functions that provide the ratio of emitted to absorbed photons. Wavelength selection is conducted by software controlled excitation and emission monochromators. The QY measurements were conducted on finely ground solids uniformly spread onto the sample holder and covered with a quartz disc.

3.3. Results and Discussion

3.3.1. XRD of phosphor powders. The X-ray diffraction (XRD) patterns are shown in Figure 3.1. In the top four spectra, the overall peak positions of the doped and undoped samples did not match with the agrellite ($NaCa_2Si_4O_{10}F$) phase as expected. Instead, the peak positions have a better correspondence with the wollastonite-2M phase ($CaSiO_3$), where the M stands for monoclinic. The JCPDS powder diffraction file (PDF: 00-027-0088) for $CaSiO_3$ is shown in the bottom of Figure 3.1. The two spectra above the reference pattern are the undoped precursor gels heated at 100 and 500 ºC. These two spectra reveal two broad bands in the vicinity of $2\theta \approx 15–50^{\circ}$ demonstrating the amorphous quality of the precursor gels. The sharp peak at $2\theta \approx 29.5^{\circ}$ can be attributed to CaO being formed during gelation. The precursor gels prefired at 500 ºC maintain an amorphous profile with a slight decrease in the intensity of both broad bands as well as the CaO peak. The annealing at 900 ºC generates a series of sharp and intense peaks suggesting the onset of crystallization. However, in comparing the annealed samples with the reference pattern at the bottom, there are two unknown peaks at $2\theta = 8.8^{\circ}$ and 21.7° which are indicated by (*). The origin of the peaks is unclear, but could suggest the possibility of a new phase of wollastonite with Na^+ in the structure. The colored XRD spectra indicate selected samples of the doped phosphors, which exhibit profiles consistent with the undoped sample. Therefore, it can be assumed that the co-doped samples containing Ce^{3+}, Tb^{3+}, Mn^{2+}, Dy^{3+} and Sm^{3+} ions do not cause any significant change to the prepared $CaSiO_3$ host.

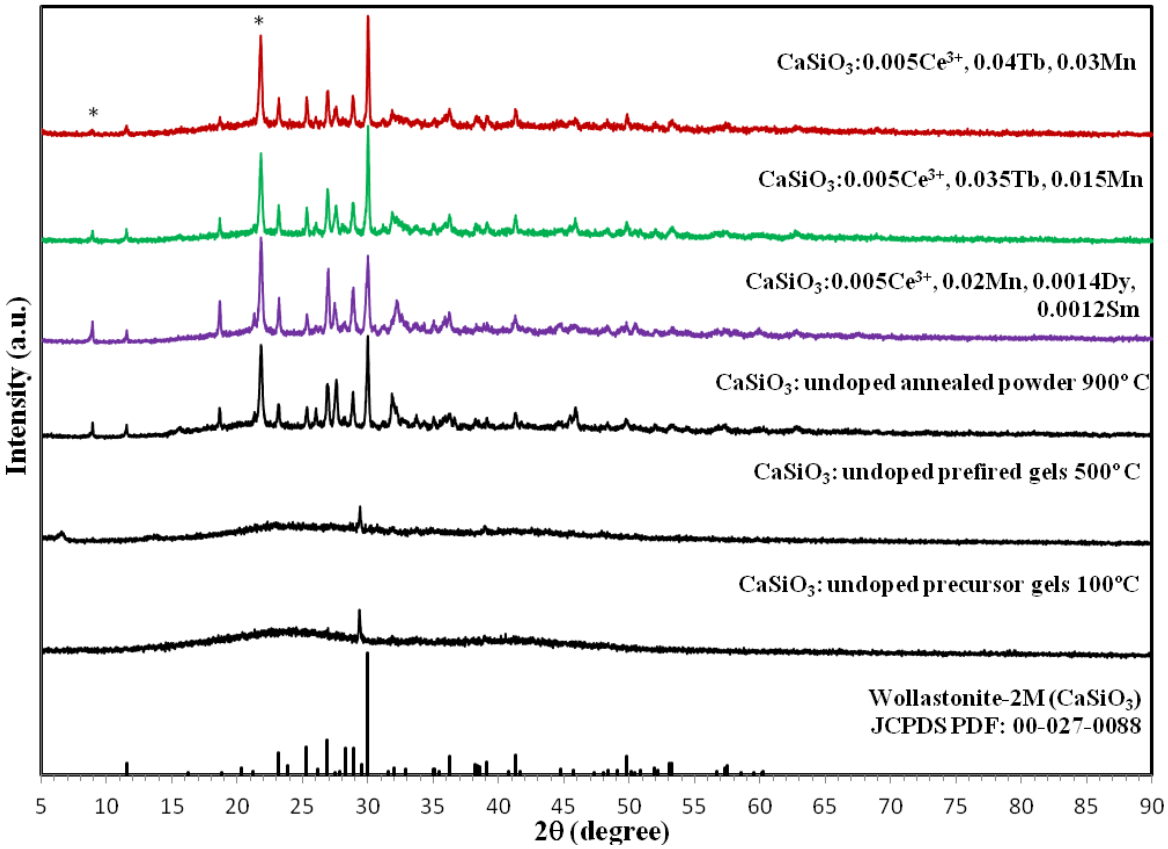

Figure 3.1. XRD patterns of undoped $CaSiO_3$ precursor gels and powder, $CaSiO_3$:Ce^{3+}, Mn^{2+}, Dy^{3+}, Sm^{3+}, and $CaSiO_3$:Ce^{3+}, Tb^{3+}, Mn^{2+} phosphors.

As reported previously by Gittens *et al.*, agrellite has a primary phase volume adjacent to that of wollastonite, but its crystallization in preference to wollastonite is dependent upon high fluoride (F) content [80]. Thus, the wollastonite phase being dominant here suggests that high levels of F were decomposed during the annealing process. Moreover, despite using a slight excess of F during synthesis, the possible intermediate formation of highly-volatile SiF_4 in the precursor gels could have caused a considerable loss of F and Si due to evaporation. Also, in natural agrellite samples, the partial replacement of calcium atoms by strontium and potassium was reported to generate substantial differences in the structure [83], which ultimately makes the synthetic replication of its structure more complex. Based on the unexpected phase difference, the synthesized phosphors will be referred to as $CaSiO_3$ from this point on in the chapter.

3.3.2. FT-IR characterization. The FT-IR spectra of the undoped $CaSiO_3$ precursor gels and annealed powder are shown in Figure 3.2. For the sample dried at 100 ºC, the FT-IR spectrum shows a series of broad bands corresponding to the –OH group (3489 cm^{-1}), the NO_3^- group (1635, 1430, and 1363 cm^{-1}), various stretching modes of Si–O (1155–820 cm^{-1}) and the stretching of Ca–O (~550 cm^{-1}), all of which arise from the starting materials contained in the gels. These components include ethanol, water, $Ca(NO_3)_2$, $NaNO_3$, and polymerized silanol groups. In the precursor gels prefired at 500 ºC, the absorption intensities of the broad bands decreased significantly indicating pyrolysis of most of the starting materials. However, the weak NO_3^- bands still observed from 1635–1363 cm^{-1} indicates incomplete decomposition at this temperature. In contrast, the appearance of weak stretching modes attributed to SiO_4 tetrahedra become noticeable in the spectral region from ~800–1100 cm^{-1}.

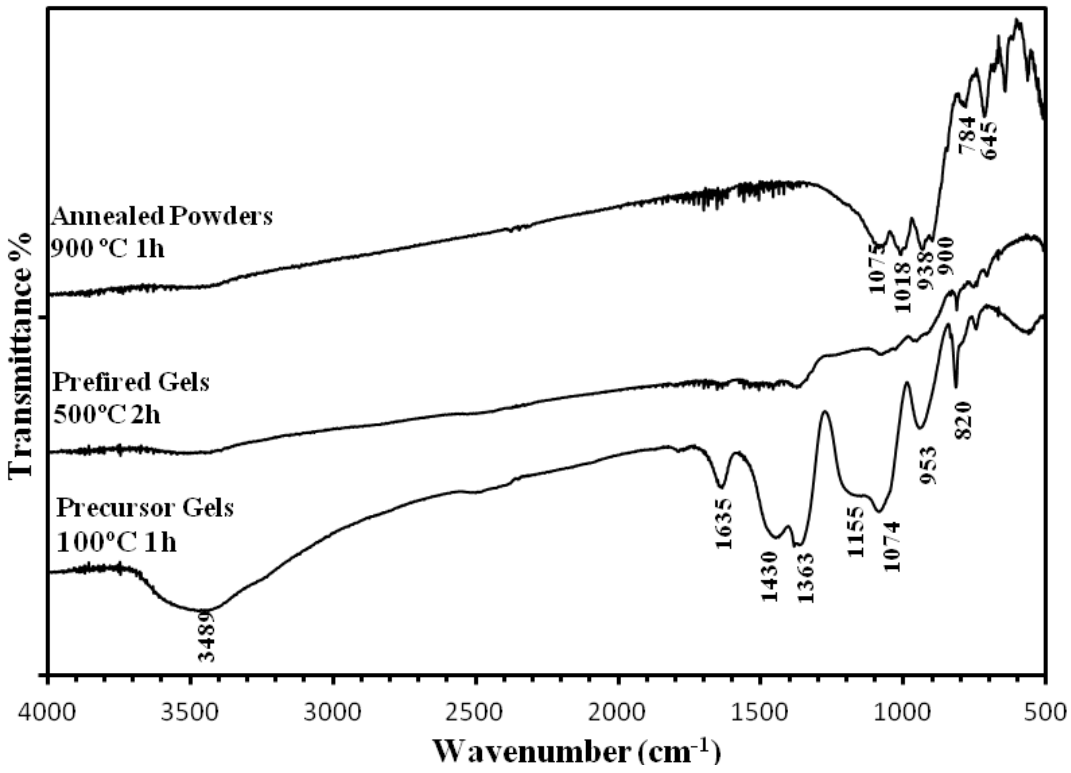

Figure 3.2. FT-IR spectra of undoped $CaSiO_3$ precursor gels dried at 100 ºC, prefired at 500 ºC, and annealed at 900 ºC.

After annealing at 900 ºC, the broad absorptions of the starting materials become negligible, and a strong well-organized absorption region attributed to the SiO_4 groups is now apparent. The group of peaks from 800–1200 cm^{-1} are assigned to asymmetric Si–O stretching modes of the SiO_4 tetrahedron, while the sharp peaks in mid-frequency range from 600–800 cm^{-1} can be attributed to Si–O–Si bond bending as well as symmetric O–SiO stretching vibrations [85, 86]. Overall, the predominant sharp bands suggest that crystalline $CaSiO_3$ has formed at 900 ºC, agreeing well with the XRD profiles presented in Figure 3.1.

3.3.3. Emission properties of natural agrellite and synthesized $CaSiO_3$:Ce^{3+}, Mn^{2+}, Dy^{3+}, Sm^{3+} phosphor. Figure 3.3 compares the emission between the natural agrellite sample (bottom in black) and the synthesized $CaSiO_3$:0.005Ce^{3+}, 0.02Mn^{2+}, 0.0014Dy^{3+}, 0.0012Sm^{3+} phosphor (top in purple). The insets are photographs of the phosphor powder (top) and agrellite (bottom) excited by a UV lamp at 302 nm. The dominant band at ~370 nm occurring in both spectra is due to the $5d^1 \rightarrow 4f^1$ allowed transition of Ce^{3+}. The broad emission is a combination of two bands associated with the ground state splitting into its $^2F_{5/2}$ and $^2F_{7/2}$ components. The two weak bands at ~479 and 488 nm occurring in both samples can be ascribed to the forbidden $^4F_{9/2} \rightarrow {}^6H_{15/2}$ transition of Dy^{3+}. In the natural sample, the $^4F_{9/2} \rightarrow {}^6H_{13/2}$ transition of Dy^{3+} at ~574 nm is superimposed with the broad $^4T_1(G) \rightarrow {}^6A_1(S)$ emission of Mn^{2+} at ~570 nm. While in the synthetic phosphor, the Mn^{2+} emission is blue-shifted with maximum at ~555 nm. Since the *d–d* transitions of Mn^{2+} are strongly coupled with the host chemical environment, the blue-shift is reflective of the structural differences. Moreover, the blue-shifted Mn^{2+} emission in the $CaSiO_3$ phosphor allows the $^4F_{9/2} \rightarrow {}^6H_{13/2}$ transition of Dy^{3+} to become more resolved. Figure 3.4 shows a magnified spectrum from 525-620 nm where the weak emissions of Sm^{3+} are also observed which correspond to the $^4G_{5/2} \rightarrow {}^6H_{5/2}$ (563 nm) and $^4G_{5/2} \rightarrow {}^6H_{7/2}$ (603 nm) transitions.

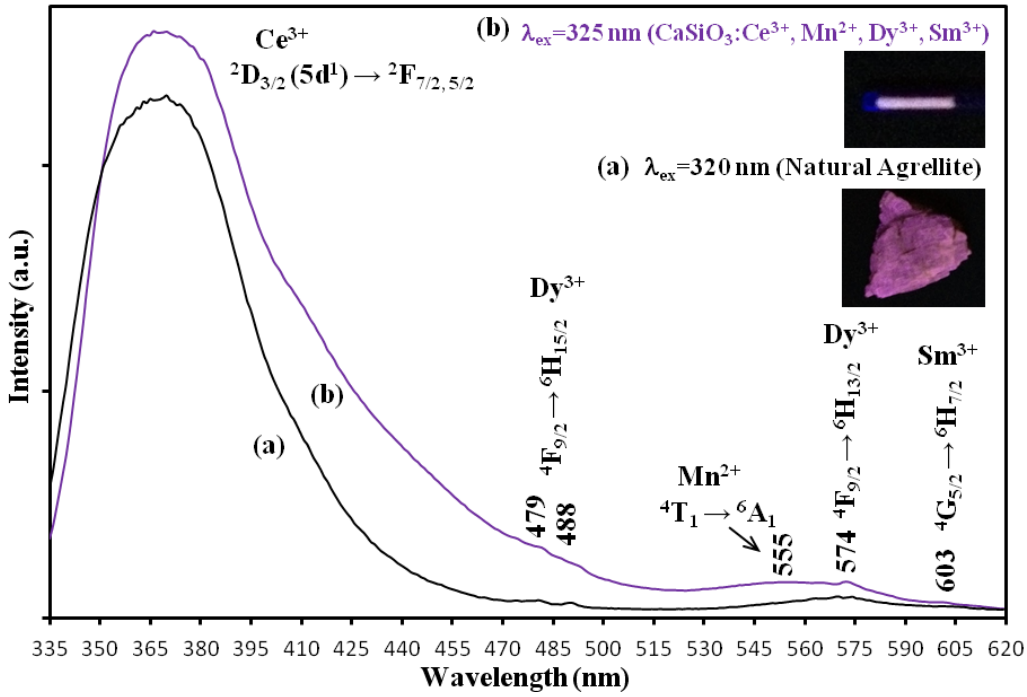

Figure 3.3. (a) Emission spectra of natural agrellite ($NaCa_2Si_4O_{10}F$) excited at 320 nm, and (b) the $CaSiO_3$:0.005Ce^{3+}, 0.02Mn^{2+}, 0.0014Dy^{3+}, 0.0012Sm^{3+} phosphor excited at 325 nm.

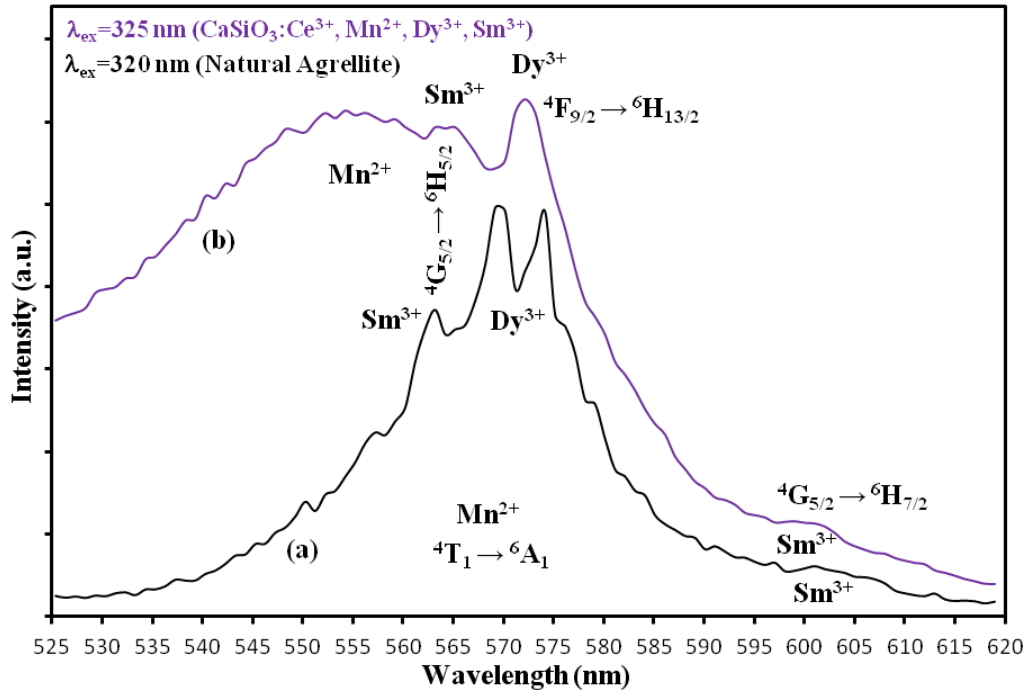

Figure 3.4. Magnified emission spectra of (a) natural agrellite and (b) the $CaSiO_3$:0.005Ce^{3+}, 0.02Mn^{2+}, 0.0014Dy^{3+}, 0.0012Sm^{3+} phosphor from 525–620 nm.

The chemical compositions of natural agrellite reported by Gittens *et al.* revealed that 3.84% of the total composition (in wt. %) was attributed to rare earth (RE) elements. Out of the 3.84%, 1.13% was determined to be CeO_2, placing it as the highest component of the RE fraction with Y_2O_3 and La_2O_3 next in line at 1.07% and 0.54%, respectively. All other RE fractions were <0.50% but as shown in Figure 3.4, Dy_2O_3 and Sm_2O_3 can still be detected spectroscopically despite accounting for only 0.14 and 0.12%, respectively.

3.3.4. Excitation properties of natural agrellite and synthesized $CaSiO_3$:Ce^{3+}, Mn^{2+}, Dy^{3+}, Sm^{3+} phosphor. The excitation spectra of the natural $NaCa_2Si_4O_{10}F$ sample and the synthesized $CaSiO_3$:0.005Ce^{3+}, 0.02Mn^{2+}, 0.0014Dy^{3+}, 0.0012Sm^{3+} phosphor are presented in Figure 3.5. For both samples, the excitation spectra were obtained by monitoring the 5*d*–4*f* emission of Ce^{3+} at 370 nm. In the natural sample, the 4*f*–5*d* excitation profile consists of three noticeable $5d^1$ excited states: a weak high-energy band at ~247 nm, a middle-band at ~283 nm, and a dominant band at ~321 nm. In comparison, the synthesized phosphor also exhibits three excitation bands but at red-shifted positions corresponding to ~257, ~300, and ~325 nm. In the synthetic phosphor, the energy difference between the shoulder at ~300 nm and the dominant band at ~325 nm is ~2,600 cm^{-1}. While in agrellite, the difference between the middle band (283 nm) and its dominant band (321 nm) is ~4000 cm^{-1}. This significant difference demonstrates how the higher excited states of Ce^{3+} are more perturbed by the structural differences, as opposed to the lower $5d^1$ excited state in which the dominant band exhibits a similar maximum for both systems (321 vs. 325 nm).

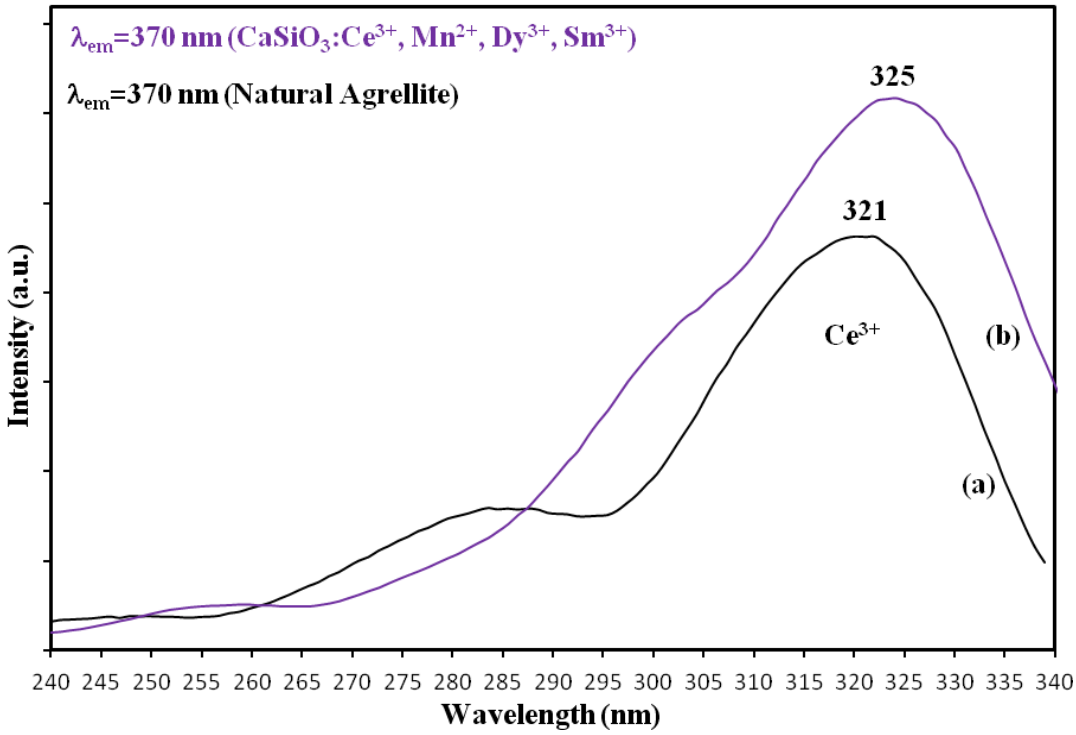

Figure 3.5. (a) Excitation spectra of natural agrellite, and (b) the $CaSiO_3$:0.005Ce^{3+}, 0.02Mn^{2+}, 0.0014Dy^{3+}, 0.0012Sm^{3+} phosphor by monitoring emission at 370 nm.

3.3.5. Photoluminescence of $CaSiO_3$:0.005Ce^{3+}, 0.04Tb^{3+}, *x*Mn^{2+} phosphor. Figure 3.6 portrays the emission spectra of the triply-doped $Ca_{1.955-x}SiO_3$:0.005Ce^{3+}, 0.04Tb^{3+}, *x*Mn^{2+} phosphor. The 5*d*–4*f* emission of Ce^{3+} at ~370 nm is present in all spectra. For reference, the $CaSiO_3$ sample doped with 0.5 mol% of Ce^{3+} alone is indicated by the solid blue spectrum. When 4 mol% of Tb^{3+} is co-doped with Ce^{3+} (green spectrum), a series of weak bands appear at 418, 436, and 445 nm, prominent blue and green bands at 488, 542 nm, and less intense orange and red bands at 583, and 620 nm. These bands can be attributed to the $^5D_3 \rightarrow {}^7F_5$ (418 nm), $^5D_3 \rightarrow {}^7F_4$ (436 nm), $^5D_3 \rightarrow {}^7F_3$ (445 nm), $^5D_4 \rightarrow {}^7F_6$ (488 nm), $^5D_4 \rightarrow {}^7F_5$ (542 nm), $^5D_4 \rightarrow {}^7F_4$ (583 nm), $^5D_4 \rightarrow {}^7F_3$ (620 nm) transitions of Tb^{3+} ions. The Mn^{2+} ions were added at varied concentrations of 1, 2, and 3 mol% which are indicated by the black, purple, and red dashed spectra, respectively. By fixing the Ce^{3+} and Tb^{3+} concentrations at 0.5 and 4 mol%, respectively,

the effects of increasing Mn^{2+} were easily evaluated. The $^4T_1(G) \rightarrow {}^6A_1(S)$ transition of Mn^{2+} produces a broad orange emission at ~560 nm that is closely superimposed with the $^5D_4 \rightarrow {}^7F_5$ (542 nm) and $^5D_4 \rightarrow {}^7F_4$ (583 nm) transitions of Tb^{3+}. As the Mn^{2+} concentration increases, there is clear evidence of an overall quenching of the Tb^{3+} transitions, suggesting an energy transfer process between the two ions. However, despite being pumped through the excitation of Ce^{3+} (λ_{ex} = 325), increasing the Mn^{2+} content appears to have negligible influence on the intensity of the 5*d*–4*f* emission band of Ce^{3+}. Although the spectroscopic contribution of the Mn^{2+} emission appears to be minor, the visual impact of Mn^{2+} is significant. The inset photograph of Figure 3.6 shows the phosphor powders being excited by a UV lamp at ~302 nm. Figure 3.7 depicts the magnified spectral region from 475–635 nm in which the Mn^{2+} broad emission shows increased intensity around the baseline region of the Tb^{3+} bands.

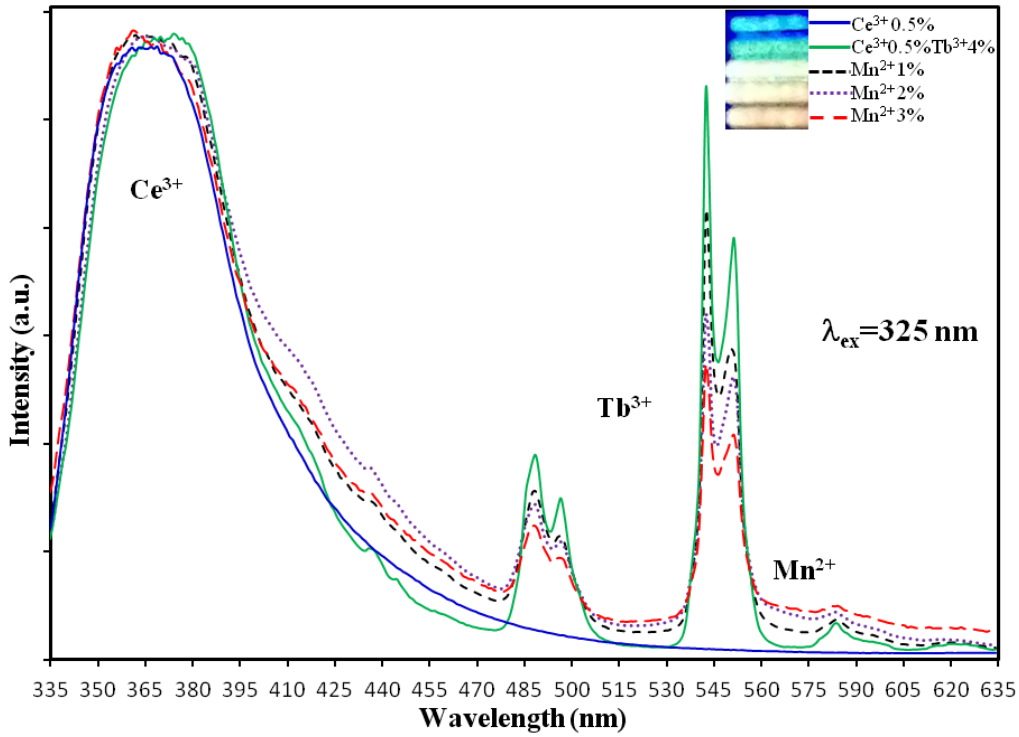

Figure 3.6. Emission spectra of $CaSiO_3$:0.005Ce^{3+}, 0.04Tb^{3+}, *x*Mn^{2+} phosphor with varied concentrations of Mn^{2+} from 1 to 3 mol%.

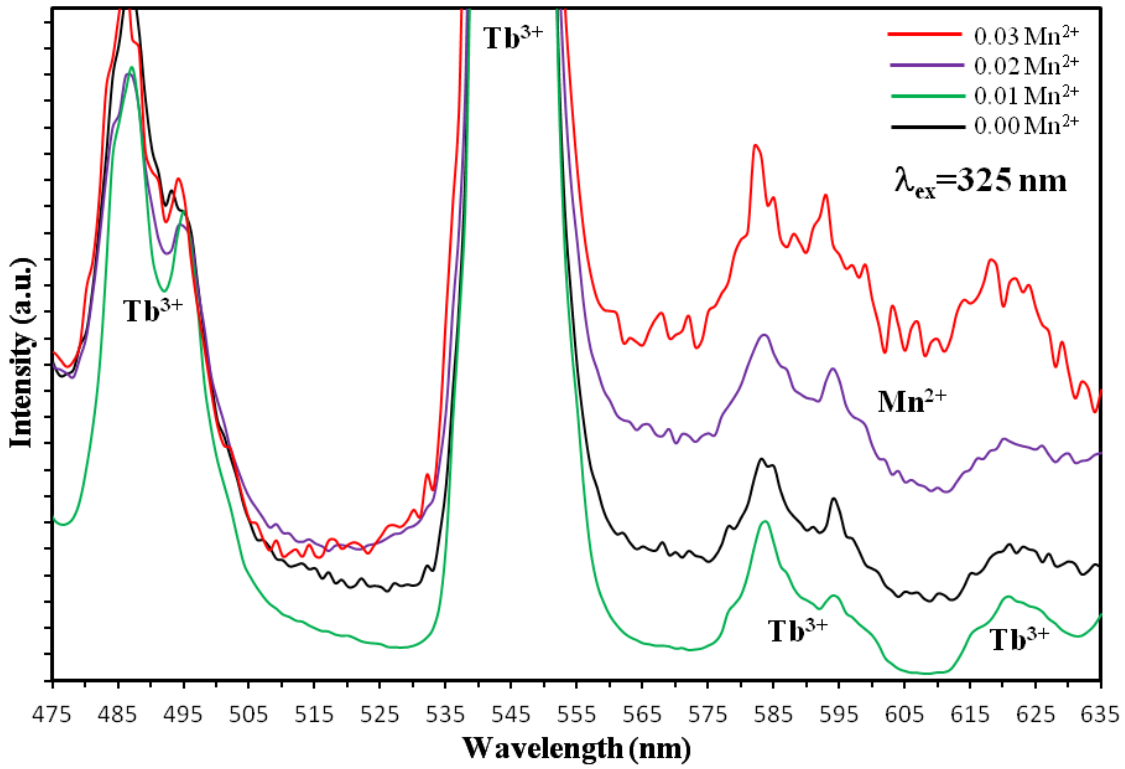

Figure 3.7. Magnified emission spectra of $CaSiO_3$:0.005Ce^{3+}, 0.04Tb^{3+}, *x*Mn^{2+} phosphor from 475–635 nm.

The sample used to obtain the excitation spectra was the white light-emitting $CaSiO_3$:0.005Ce^{3+}, 0.035Tb^{3+}, 0.015Mn^{2+} sample which is shown in Figure 3.8. Here the concentration ratios of Tb^{3+} and Mn^{2+} were slightly adjusted, but are still within range of the concentrations used for the samples presented in Figure 3.6. Therefore, this sample was used to portray the excitation properties of all the samples. The solid black spectrum is the emission profile. The excitation properties shown in Figure 3.8 are represented by the purple, green, and orange-dashed spectra which were obtained by monitoring the fixed emissions of Ce^{3+}, Tb^{3+}, and Mn^{2+} at 370, 545, and 565 nm, respectively. Since the 4*f*–5*d* transition of Ce^{3+} is observed in all three excitation spectra (~325 nm), this is direct evidence of energy transfer from $Ce^{3+} \rightarrow Tb^{3+}$, and $Ce^{3+} \rightarrow Mn^{2+}$ within the host.

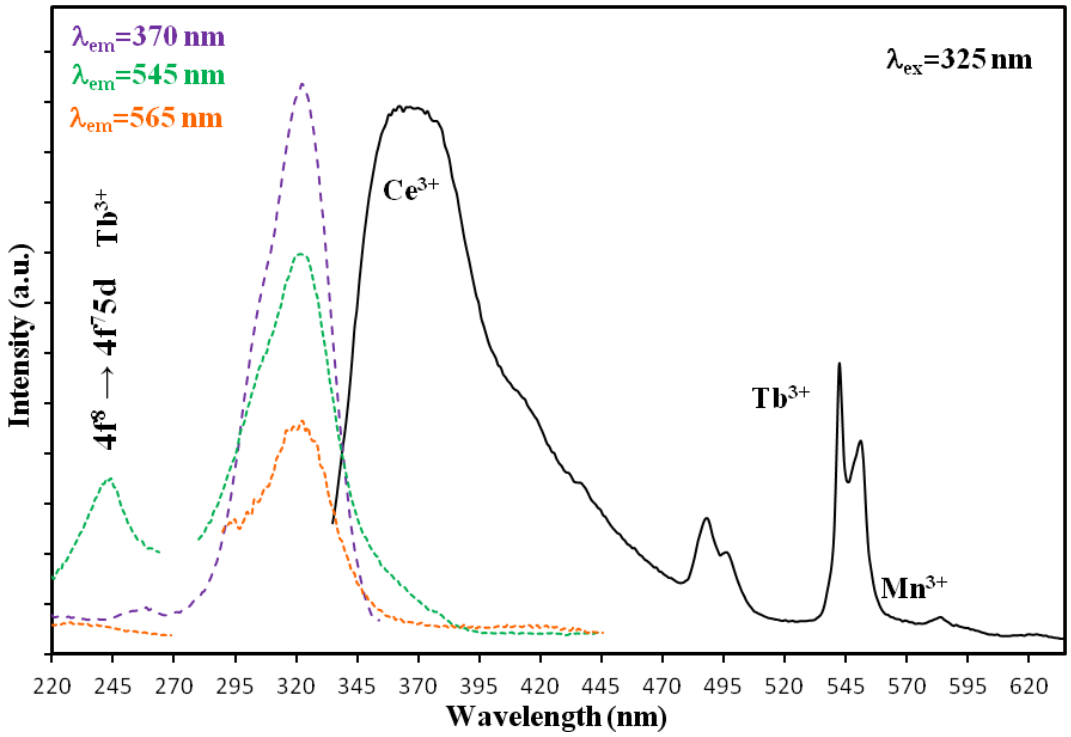

Figure 3.8. Excitation (dashed colored lines) and emission (solid line) spectra of white light-emitting $CaSiO_3$:0.005Ce^{3+}, 0.035Tb^{3+}, 0.015Mn^{2+} phosphor.

Additionally, by monitoring the 545 nm emission of Tb^{3+}, a prominent high-energy band occurring at ~240 nm reveals that Tb^{3+} can also be excited through its $4f^8 \rightarrow 4f^75d$ allowed transition. To confirm that this band was indeed due to the Tb^{3+} transition instead of a higher $5d^1$ excited state Ce^{3+}, an additional emission spectrum was obtained by exciting Tb^{3+} through its $4f^8 \rightarrow 4f^75d$ transition at ~240 nm and is shown in Figure 3.9. The broad emission of Ce^{3+} is clearly absent, and instead, transitions from higher excited states of Tb^{3+} are observed such as the $^5L_{10} \rightarrow {}^7F_6$ (360 nm) and $^5D_3 \rightarrow {}^7F_6$ (378 nm) transitions. Although energy transfer from $Tb^{3+} \rightarrow Mn^{2+}$ was the most probable explanation for the quenched Tb^{3+} emission showed previously (Figure 3.8), the energy transfer to Mn^{2+} through the $4f^8 \rightarrow 4f^75d$ transition appears negligible since the $^5D_4 \rightarrow {}^7F_4$ transition is well-defined without contribution from the Mn^{2+} emission band.

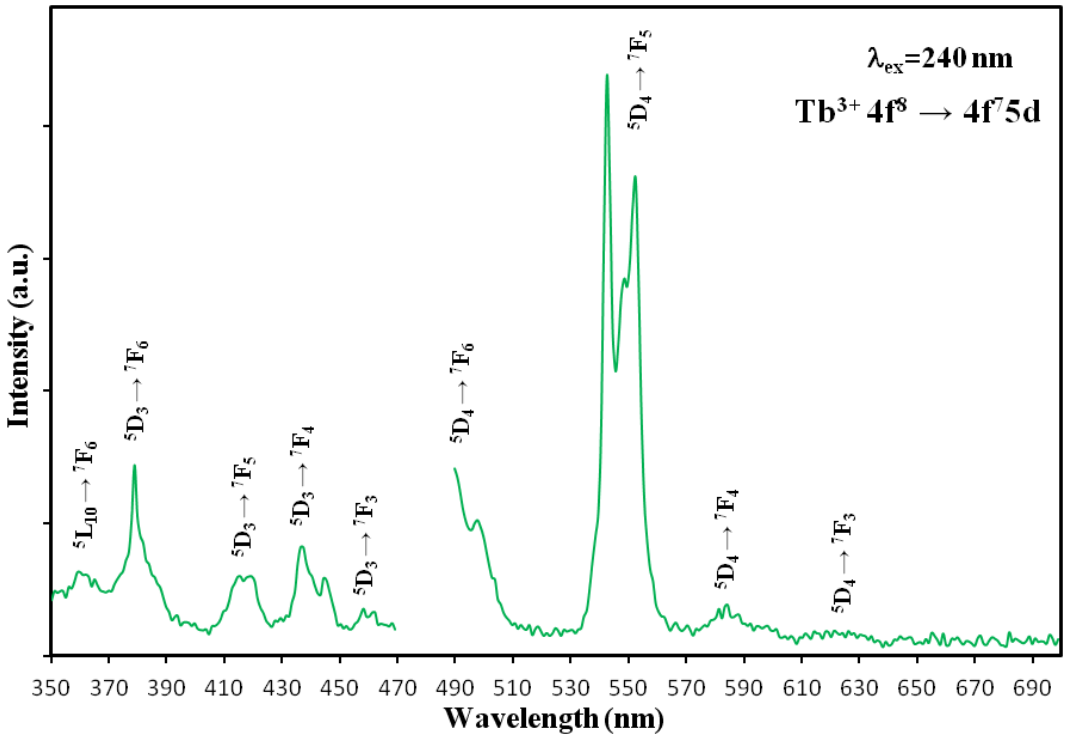

Figure 3.9. Emission spectrum obtained by exciting Tb^{3+} through the $4f^8 \rightarrow 4f^7 5d$ transition at 240 nm (spectral region from 470-490 nm was bypassed to avoid 2nd order effect).

3.3.6. Luminescence lifetime analysis. According to Blasse and Grabmarier [87], the luminescence decay behavior can be expressed by:

$$I = I_0 \exp(-t/\tau), \tag{3.6}$$

where I and I_0 represent the luminescence intensities at time t and 0, and τ is the luminescence lifetime. To analyze energy transfer via luminescence lifetime measurements, Figure 3.10 shows the decay curves of the Ce^{3+} 380 nm emission band in the samples $CaSiO_3$:0.005Ce^{3+}, $CaSiO_3$:0.005Ce^{3+}, 0.04Tb^{3+}, and $CaSiO_3$:0.005Ce^{3+}, 0.04Tb^{3+}, 0.01Mn^{2+}, for which the lifetimes of Ce^{3+} were determined to be 770, 759, and 738 ns, respectively. The decrease of the Ce^{3+} lifetime with the addition of the Tb^{3+} and Mn^{2+} acceptors is direct evidence of energy transfer from $Ce^{3+} \rightarrow Tb^{3+}$ and $Ce^{3+} \rightarrow Mn^{2+}$.

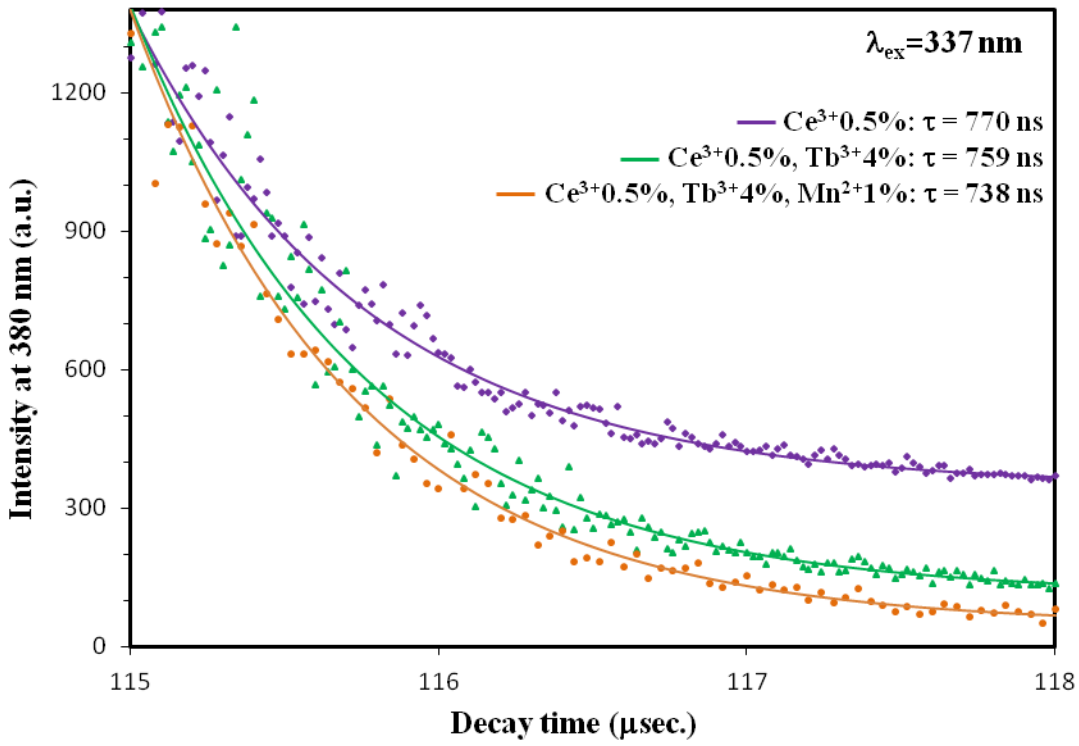

Figure 3.10. Decay profiles of Ce^{3+} 380 nm emission band in $CaSiO_3$:0.005Ce^{3+}, $CaSiO_3$:0.005Ce^{3+} 0.04Tb^{3+}, and $CaSiO_3$:0.005Ce^{3+}0.04Tb^{3+}, 0.01Mn^{2+} phosphors.

The lifetime behavior of the Tb^{3+} ions was investigated by obtaining the decay curve for the 541 emission band in the $CaSiO_3$:0.005Ce^{3+}, 0.04Tb^{3+} sample which is shown in Figure 3.11. The lifetime of the Tb emission was determined to be ~2.9 ms. Since the lifetime of Tb is considerably longer than that of Ce^{3+}, this further confirms that Ce^{3+} is serving as the donor for the Tb^{3+} emission at 541 nm. On the other hand, the decay profile shown in Figure 3.12 reveals that the lifetime of Tb^{3+} remains unchanged when Mn^{2+} is added at 1%. Consequently, it can be assumed that Mn^{2+} is not being pumped by Tb^{3+} despite quenching its emission as shown in Figure 3.6. Moreover, the presence of Mn^{2+} appears to induce NR relaxation processes of Tb^{3+} through other pathways.

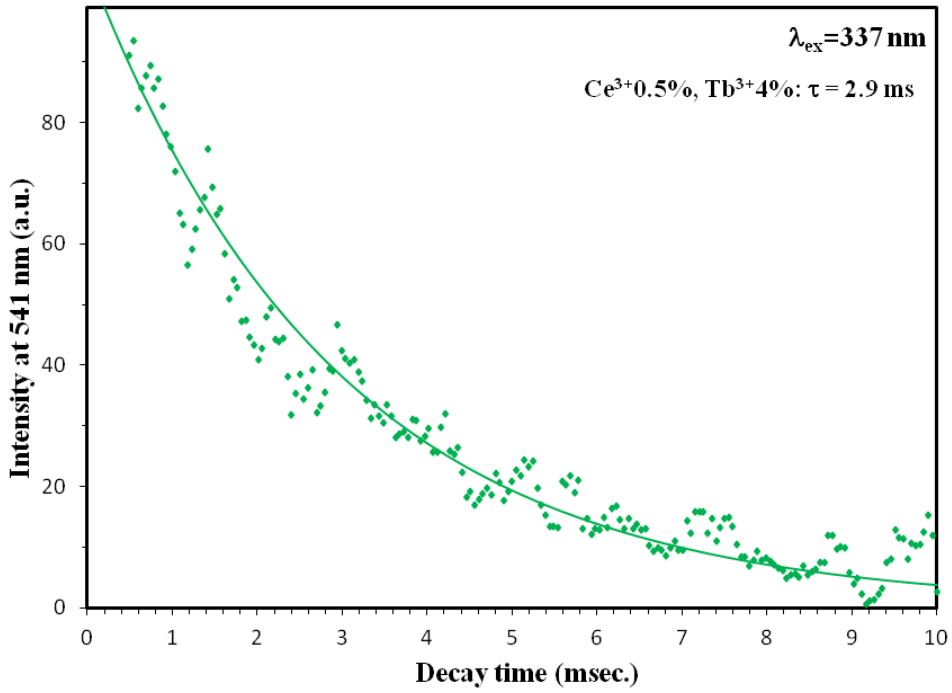

Figure 3.11. Decay profile of Tb^{3+} 541 nm emission band in $CaSiO_3$:0.005Ce^{3+} 0.04Tb^{3+} phosphor.

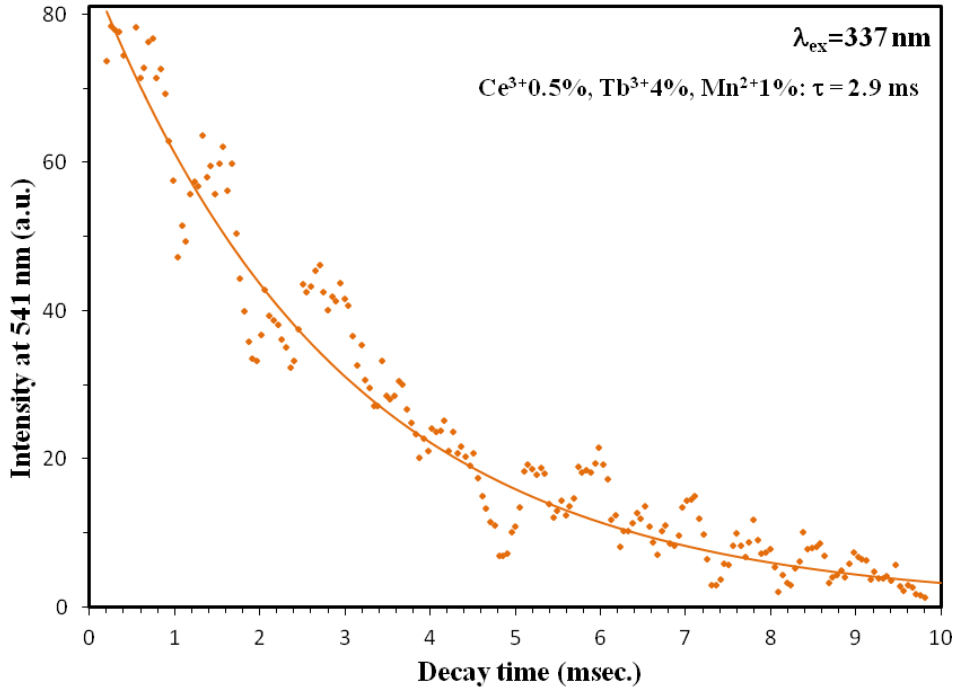

Figure 3.12. Decay profile of Tb^{3+} 541 nm emission band in $CaSiO_3$:0.005Ce^{3+}, 0.04Tb^{3+}, 0.01Mn^{2+} phosphor.

Figure 3.13 shows the decay curve for the Mn^{2+} emission at 555 nm and its lifetime was determined to be ~3.6 ms. Indeed, there exists more than a 1000 magnitude difference between the decay time of Ce^{3+} and that of Mn^{2+}. The significantly longer decay time of Mn^{2+} reveals the forbidden nature of the *d–d* transition, and also suggests that the short-lived Ce^{3+} emission is serving as the donor in the energy transfer process.

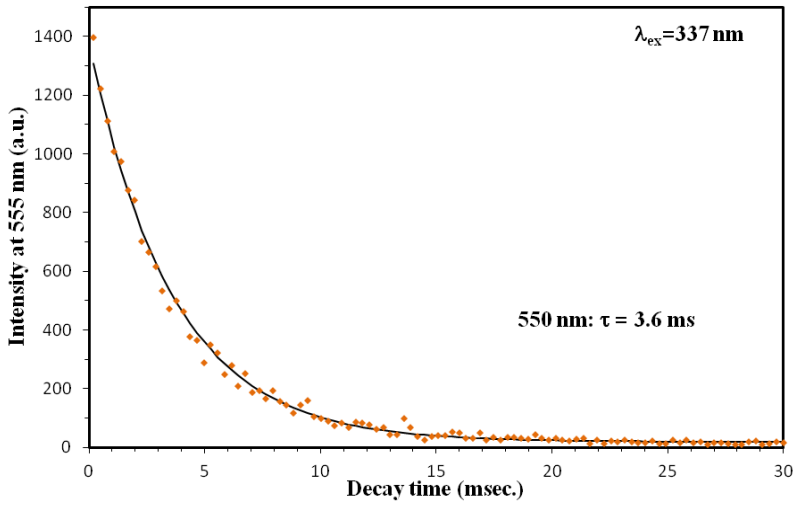

Figure 3.13. Decay profile of Mn^{2+} emission band at 555 nm in $CaSiO_3$:0.005Ce^{3+}, 0.04Tb^{3+}, 0.01Mn^{2+} phosphor.

The time-resolved emission spectrum of Ce^{3+} in the $CaSiO_3$:0.005Ce^{3+}, 0.04Tb^{3+} phosphor is shown in Figure 3.14. At a delay of 100 μs, the absence of the Tb^{3+} emission at 545 nm is direct evidence that the Tb^{3+} ions are still being pumped to their excited state by Ce^{3+}, and have yet to begin the emission process. In recognizing the close overlap of the Mn^{2+} and Tb^{3+} emission bands in the 530–570 nm region, Figure 3.15 portrays the time-resolved emission spectra to further inspect the lifetime behavior of Tb^{3+} and Mn^{2+} ions. At a delay time of 10 ms, the general emission profile of Tb^{3+} (542 nm) is dominant. However, at a 20 ms delay, the emission of Tb^{3+} has decayed significantly, and what remains is the long-lived broad emission of Mn^{2+}.

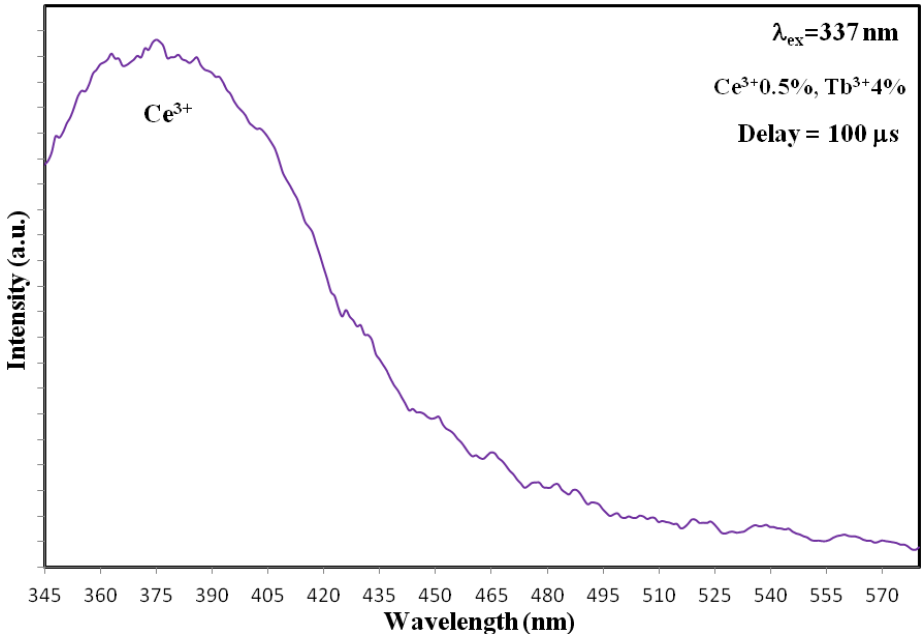

Figure 3.14. Time-resolved spectrum of Ce^{3+} emission band in $CaSiO_3$:0.005Ce^{3+}, 0.04Tb^{3+}, phosphor at a delay of 100 µs.

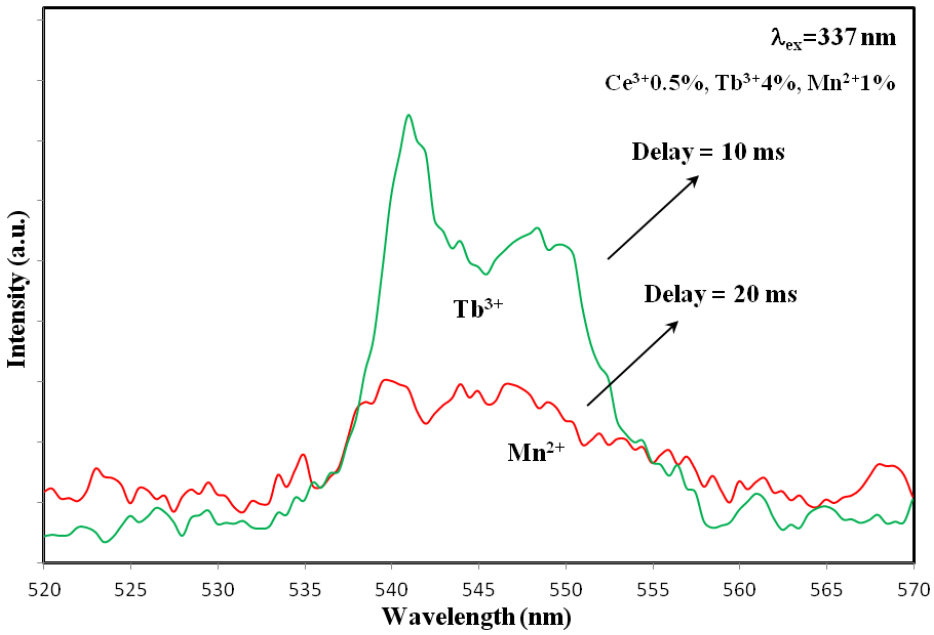

Figure 3.15. Time-resolved spectra Tb^{3+} and Mn^{2+} emission bands in $CaSiO_3$:0.005Ce^{3+}, 0.04Tb^{3+}, 0.01Mn^{2+} phosphor at delay times 10 and 20 ms.

3.3.7. Quantum yield analysis. The quantum yield (QY) analysis was an additional probe used to understand the energy transfer processes between the Ce^{3+}, Tb^{3+}, and Mn^{2+} ions, as well as the overall efficiency of the phosphors in terms of photons emitted vs. photons absorbed. In addition to energy transfer, the other NR processes that influence the luminescence lifetime can be revealed by the QY analysis, making it a complimentary characterization to the lifetime analysis. The general relation of the observed luminescence lifetime (τ_{obs}) to these processes is expressed by the following:

$$\tau_{obs} = \frac{1}{k_r + k_{NR} + k_{ET}}, \tag{3.7}$$

where k_r is the radiative rate constant, k_{NR} is the non-radiative rate constant, and k_{ET} is the energy transfer rate constant. Based on the relation, it can be seen that as these rate constants increase, the lifetime value decreases. Thus, the quantum yield analysis is vital in assessing the k_{NR} component of the phosphors. Table 1 shows the results of the quantum yield measurements for all of the $CaSiO_3$:0.005Ce^{3+}, $x$$Tb^{3+}$, $y$$Mn^{2+}$ samples including the $CaSiO_3$ sample doped with 0.5% Ce^{3+} alone as a reference. The samples are designated by the numbers on left side of table and henceforth will be referred to as such.

It can be seen from Table 1 that sample **1** exhibited the highest QY at 16.2%. Since the Ce^{3+} emission at 380 nm is in the absence of Tb^{3+} and Mn^{2+} ions, only the radiative and non-radiative rates will be dominant. In contrast, in sample **2** the QY for the Ce^{3+} emission is quenched by more than 10 times providing a quantum yield of only 1.5% suggesting a highly efficient energy transfer taking place from the $Ce^{3+} \rightarrow Tb^{3+}$ acceptor ion. When Mn^{2+} was introduced at 1% (sample **3a**), the QY for both the Ce^{3+} and Tb^{3+} emission bands increased slightly, and the total QY for the phosphor was increased to 4.8%. This observation suggests that the presence of Mn^{2+} at 1 mol% does not negatively influence the efficiency of the Ce^{3+} and

Tb^{3+} emission bands. However, for samples **3b** and **3c**, the QY of Tb^{3+} decreases linearly with increasing Mn^{2+}, agreeing well with the steady-state quenching shown previously in Figure 3.6. The slight increase of the QY for Ce^{3+} for sample **3c** reveals that the efficiency of the Ce^{3+} band is less affected by Mn^{2+} content in comparison to Tb^{3+}, which also agrees well with Figure 3.6 where the intensity of the Ce^{3+} band remains unaffected by increasing Mn^{2+}.

Table 3.1

Quantum yield measurements for $CaSiO_3$:0.005Ce^{3+}, xTb^{3+}, yMn^{2+} phosphors

Sample	Quantum Yield Ce^{3+} emission at 380 nm	Quantum Yield Tb^{3+} emissions at 488 and 542 nm	Total Quantum Yield
1. $CaSiO_3$:0.5% Ce^{3+}	16.2%	N/A	16.2%
2. $CaSiO_3$:0.5% Ce^{3+}, 4%Tb^{3+}	1.5%	1.3%	2.8%
3a. $CaSiO_3$:0.5% Ce^{3+}, 4%Tb^{3+}, 1%Mn^{2+}	2.6%	2.2%	4.8%
3b. $CaSiO_3$:0.5% Ce^{3+}, 4%Tb^{3+}, 2%Mn^{2+}	1.2%	1.2%	2.4%
3c. $CaSiO_3$:0.5% Ce^{3+}, 4%Tb^{3+}, 3%Mn^{2+}	1.6%	1.1%	2.6%
4. $CaSiO_3$:0.5% Ce^{3+}, 3.5%Tb^{3+}, 1.5%Mn^{2+}	2.1%	1.0%	3.1%

In sample **4** where Tb^{3+} and Mn^{2+} have been lowered to 3.5 and 1.5 mol%, respectively, the QY is increased for the Ce^{3+} band which could be due to the reduced interaction with Tb^{3+} ions. On the other hand, the QY of Tb^{3+} is only slightly affected. Since the lifetimes (Figure 3.10) and QY (Table 1) were obtained for the Ce^{3+} emission in samples **1**, **2** and **3a**, the radiative (k_r) and non-radiative (k_{NR}) rate constants were calculated using equations 3.7 and 3.8, respectively [88].

$$k_r = \frac{\phi \text{samp}}{\tau_{obs}} \tag{3.8}$$

$$k_{NR} = \left(\frac{1}{\tau_{obs}} - k_r\right) \tag{3.9}$$

where, ϕsamp is the quantum yield for the Ce^{3+} and Tb^{3+} emission bands in samples **1**, **2**, and **3a**, and τ_{obs} are the lifetime values obtained from Figures 3.10–3.12. The calculated radiative and non-radiative rate constants for the excited state decay processes of the Ce^{3+} and Tb^{3+} ions are summarized in Table 2. As shown in Table 2, the non-radiative (k_{NR}) components of the Ce^{3+} emission increase progressively with the addition of Tb^{3+} and Mn^{2+}. The radiative rate constants, $k_{r,}$ for the Ce^{3+} emission in **1** is calculated as 2.1×10^5 s^{-1}, while the non-radiative rate constant k_{nr} is 1.08×10^6 s^{-1}. As shown in the Table, the non-radiative rate in compound **2** increases to 1.29×10^6 s^{-1}. Assuming that the increase is due to the energy transfer contribution to the overall rate, k_{ET} value is estimated as 1.1×10^5 s^{-1}. Moreover, the values of the k_r and k_{NR} processes for the Tb^{3+} emissions in **2** are calculated as 4.48 and 340 s^{-1}, respectively.

Table 3.2

*Summary of photophysical data for Ce^{3+} and Tb^{3+} emissions in samples **1**, **2**, and **3a***

Sample	λ (nm)	ϕ_{samp}	τ	k_r, s^{-1}	k_{NR}, s^{-1}
1. $CaSiO_3$:0.5% Ce^{3+}	380	0.162	770 ns	2.10×10^5	1.08×10^6
2. $CaSiO_3$:0.5% Ce^{3+}, 4%Tb^{3+}	380	0.015	759 ns	1.97×10^4	1.29×10^6
3a. $CaSiO_3$:0.5% Ce^{3+}, 4%Tb^{3+},1%Mn^{2+}	380	0.026	738 ns	3.52×10^4	1.32×10^6
2. $CaSiO_3$:0.5% Ce^{3+}, 4%Tb^{3+}	488, 542	0.013	2.9 ms	4.48	340
3a. $CaSiO_3$:0.5% Ce^{3+}, 4%Tb^{3+},1%Mn^{2+}	488, 542	0.022	2.9 ms	7.58	337

Comparison of the decay processes in Ce^{3+}, and Tb^{3+} emissions indicate that, while radiative and nonradiative processes in the former are competitive, the nonradiative process is dominant in the latter, which is also in agreement with the quenching observed Figure 3.6. The addition of Mn^{2+} at 1% in sample **3a** slightly increases the radiative (k_r) component for both the Ce^{3+} and Tb^{3+} emission bands. Although the lifetime of Tb^{3+} is being unaffected by the presence of Mn^{2+} suggests a lack of energy transfer between the two ions, it is clearly evident that the

overall non-radiative processes of the Tb^{3+} emission remain dominant in both samples **2** and **3a**. Hence, for any practical application further modification of the structural features may be needed to enhance the radiative component exhibited in the Tb^{3+} ions.

3.3.8. Chromaticity characterization. Figure 3.16 depicts the Commission Internationale de l'éclairage (CIE) chromaticity coordinates of the natural agrellite, $CaSiO_3$:0.005Ce^{3+}, 0.02Mn^{2+}, 0.0014Dy^{3+}, 0.0012Sm^{3+}, and $CaSiO_3$:0.005Ce^{3+}, *x*Tb^{3+}, *y*Mn^{2+} phosphors. The chromaticity coordinates of natural agrellite (0.32, 0.21) locate in the mid-purple color space. According to principles of chromaticity, since the coordinates of agrellite fall along a linear path represented by the dashed arrow drawn between the violet region (~380 nm) and the yellow-orange region (~580 nm), this suggests that the pink appearance of the natural agrellite emission is generated by appropriate mixing of the Ce^{3+} violet emission, and the yellow-orange contributions of Mn^{2+}, Dy^{3+}, and Sm^{3+}. The synthesized $CaSiO_3$:0.005Ce^{3+}, 0.02Mn^{2+}, 0.0014Dy^{3+}, 0.0012Sm^{3+} phosphor exhibits coordinates (0.29, 0.22) significantly close to agrellite (0.32, 0.21). For reference, the coordinates of $CaSiO_3$:0.005Ce^{3+} in the absence of the yellow-orange emitting Mn^{2+}, Dy^{3+}, and Sm^{3+} are also given to further demonstrate that the pink emission is only generated by the proper mixing of violet and orange light sources. In the $CaSiO_3$:0.005Ce^{3+}, 0.04Tb^{3+}, yMn^{2+} phosphors with tuned concentrations of Mn^{2+} and Tb^{3+}; it is clearly evident that most of the coordinates are plotted in the white region of color space. In the $CaSiO_3$:0.005Ce^{3+}, 0.04Tb^{3+}, *x*Mn^{2+} sample where Mn^{2+} is absent (0 mol %), the coordinates (0.25, 0.29) locate in the whitish cyan region demonstrating the mixing of the dominant violet and blue-green emission bands of Ce^{3+} and Tb^{3+}, respectively. The addition of Mn^{2+} at 1 mol%, increases both the *x* and *y* values significantly (0.31, 0.38), despite exhibiting a relatively weak contribution to the emission spectra of Figures 3.6 and 3.7.

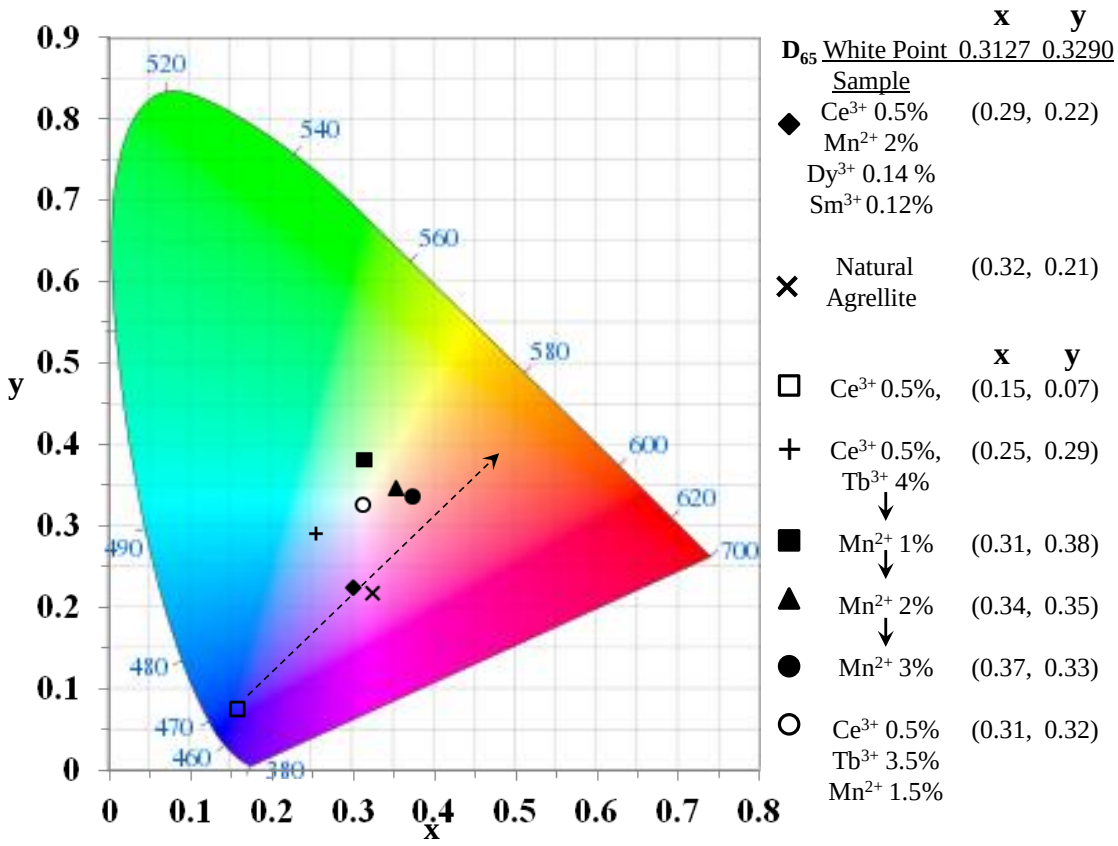

Figure 3.16. CIE chromaticity diagram of natural agrellite, $CaSiO_3$:0.005Ce^{3+}, 0.02Mn^{2+}, 0.0014Dy^{3+}, 0.0012Sm^{3+}, and $CaSiO_3$:0.005Ce^{3+}, *x*Tb^{3+}, *y*Mn^{2+} phosphors.

As the Mn^{2+} content increases to 2 and 3 mol%, a notable decrease in the *y* coordinates agrees well with the quenching of the Tb^{3+} emission, while the increased *x* coordinates correspond to the enhanced orange emission of Mn^{2+} ions. Importantly, the coordinates of the Mn^{2+} 2 mol% (0.34, 0.35) and 3 mol% (0.37, 0.33) samples correspond to correlated color temperatures (T_c) of 4932 ºK and 3923 ºK, respectively. These color temperatures match color tones associated with warm white light, which may render these phosphors suitable for warm-WLEDs. By slightly lowering the Tb^{3+} content to 3.5 mol% and the Mn^{2+} to 1.5 mol%, the chromaticity coordinates were optimized to the central region of white light (0.31, 0.32). Moreover, the $CaSiO_3$:0.005Ce^{3+}, 0.035Tb^{3+}, 0.015Mn^{2+} sample exhibits a T_c of 6624 ºK, which

demonstrates an excellent closeness to daylight (natural) white light (6500 ºK), making this phosphor a suitable candidate for WLEDs intended for general illumination. The photograph of all seven $CaSiO_3$:0.005Ce^{3+}, *x*Tb^{3+}, yMn^{2+} phosphors under UV lamp at 302 nm is shown in Figure 3.17.

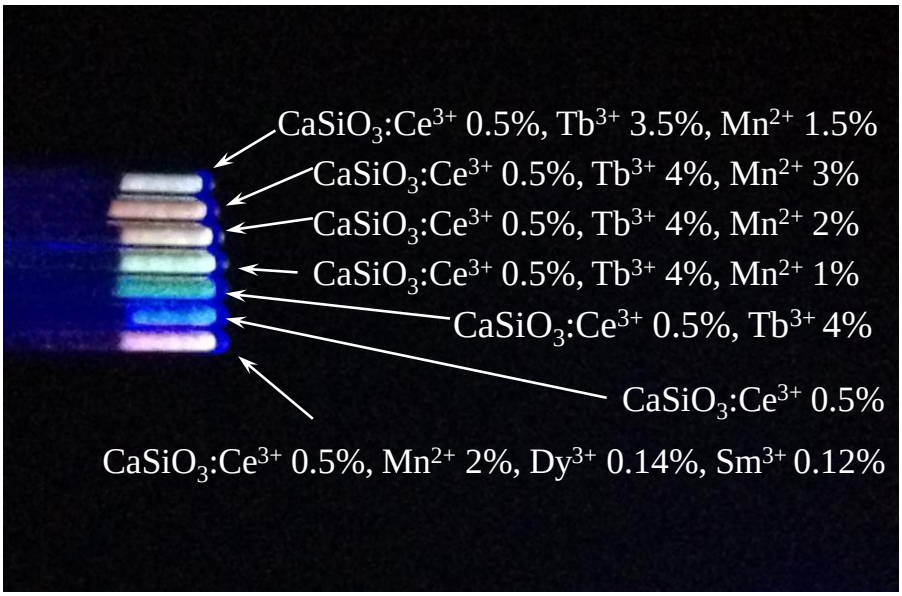

Figure 3.17. Photographs of all synthesized $CaSiO_3$:0.005Ce^{3+}, *x*Tb^{3+}, *y*Mn^{2+} phosphors under UV lamp at 302 nm.

3.4. Conclusion

The emission and excitation properties of the natural agrellite mineral have been reported. The attempt to synthesize a phosphor with a structure synonymous to agrellite phase, continues to be work in progress. Despite the structural differences between agrellite and the $CaSiO_3$ phosphor reported here, great progress was achieved in understanding the necessary chromatic elements required to reproduce its pink emission. Concurrently, novel phosphors with various hues of white light were successfully prepared using traditional sol-gel techniques. Moreover, a unique energy transfer was observed from Ce^{3+} to Tb^{3+} and Mn^{2+} ions as confirmed by PL spectra, lifetime measurements, and QY data. While Mn^{2+} was mainly pumped through

the Ce^{3+} donor, increasing its concentration induced significant quenching of the Tb^{3+} emission bands resulting in tunable chromaticity coordinates. The decay analysis showed a relatively short decay time for Ce^{3+} and a significantly longer lifetimes for both Tb^{3+} and Mn^{2+}, suggesting the existence of energy transfer from Ce^{3+} to Tb^{3+} and Mn^{2+}. The time-gated emission profile of Ce^{3+} at a delay of 100 μs showed an absent Tb^{3+} emission, providing additional evidence of Tb^{3+} serving as the acceptor in the excitation process. The $CaSiO_3$:0.005Ce^{3+}, 0.035Tb^{3+}, 0.015Mn^{2+} phosphor showed an optimized daylight white emission with a color temperature of ~6624 K, while the phosphor with Mn^{2+} concentrations of 2 and 3 mol% provided warm color temperatures of 4932 ºK and 3923 ºK, respectively. Hence, these series of phosphors demonstrate the tunable feature of white light emission via concentration variation. With further QY improvements, the application of these phosphors to a midwave UV pump can offer promising applications for several types of WLEDs.

CHAPTER 4

Concluding Remarks and Future Outlook

4.1. Concluding Remarks

In this dissertation, two concepts of achieving tunable photoluminescence were presented. The first one comprised of tuning the emission profile of a phosphor by varying the excitation wavelength. In Chapter 1, the narrow excitation band of $CaWO_4$ was extended by the inclusion of MoO_4^{2-} groups into its structure which ultimately combined two emitting complexes into one host. Since both $CaWO_4$ and $CaMoO_4$ independently are excellent hosts for energy transfer to Ln^{3+} ions, this work demonstrated that they can also serve as suitable hosts when combined. The broad-emitting $CaW_{0.99}Mo_{0.01}O_4$ host transferring its excitation energy to sharp BGR-emitting Ln^{3+} ions introduced a novel way to generate the emission of white light. Moreover, the red-shifted location of the Eu^{3+}–O^{2-} CT excitation band within the $CaW_{0.99}Mo_{0.01}O_4$ host, allowed the red component of Eu^{3+} to contribute under longer excitation wavelengths, serving as an additional source of tuning the quality of the white light via changing the excitation wavelength.

Chapter 2 further portrayed the first concept of wavelength-tunability which was also made possible by the dominant Eu^{3+}–O^{2-} CT band, and its red-shifted position relative to the WO_4^{2-} CT excitation band. The charge compensation effects of Na^+ on the luminescence properties of $CaWO_4$:Eu^{3+} not only enhanced the red emission, but also influenced the excitation mechanisms of the phosphor in which the Eu^{3+}–O^{2-} CT band was clearly more dominant in the $Ca_{1-2x}WO_4$:Eu_xM_x (M = Na^+) samples. The proposed explanation is based on fact that the charge compensation reduced the number of Ca^{2+}-vacant sites that would otherwise increase lattice distortion. Thereby, since the Eu^{3+} ions are in less competition with vacancies when Na^+ is

included, the occupation Eu^{3+} at more Ca^{2+} sites leads to increased emission intensity. Also, in considering the S_4 point symmetry of $CaWO_4$, Ca^{2+} ions are in 8-fold coordination with oxygen, where four have bond lengths of 2.44 Å and the other four are at 2.48 Å forming a distorted cube that lacks inversion symmetry [49, 89]. Since the $^5D_0 \rightarrow {}^7F_2$ (616 nm) electric dipole transition of Eu^{3+} is hypersensitive to coordination environments that lack inversion symmetry, the prominent increase in the intensity of this transition provides further evidence that the co-doping of Na^+ permits more Eu^{3+} ions to occupy more Ca^{2+} sites. Ultimately, these aforementioned conditions led to the fabrication of a blue/red-emitting $Ca_{1-2x-2y}Tm_xEu_yNa_{x+y}WO_4$ phosphor with emission properties closely matching the absorption profile of chlorophyll *b*. Moreover, the capability of tuning the blue and red emissions offers a potential benefit for plants that require specific ratios of blue/red light, while reducing the number LED units needed for operation.

The second concept comprises obtaining tunable photoluminescence by varying the dopant concentrations within the phosphor host. In the initial attempts to reproduce the photoluminescence of agrellite, multiple samples and trials not reported here were synthesized with various ratios of Ce^{3+} and Mn^{2+} until the emission and chromaticity properties matched well with agrellite by using 0.5 mol% Ce^{3+} and at least 2 mol% Mn^{2+}. Gittens *et al.* reported that the Ce^{3+} and Mn^{2+} contents (in wt. %) of natural agrellite were 1.13 and 0.25%, respectively [80]. These fractions were also attempted in this investigation, but the result was not the characteristic pink emission of agrellite, but instead a dominant bluish-violet emission of Ce^{3+} where contributions from Mn^{2+} were not detected in the emission spectrum. Certainly, the difference in crystal phase and structure is likely the explanation as to why such different Ce^{3+} and Mn^{2+} ratios were required for the emission properties of the synthetic phosphor to match that of agrellite.

The concept of concentration tuning was further demonstrated in the synthetic phosphor triply-doped with Ce^{3+}, Tb^{3+}, and Mn^{2+} ions. The Tb^{3+} ion was selected because it was efficiently pumped by Ce^{3+} and yet did not significantly quench the Ce^{3+} emission, even up to the 4 mol% concentration reported here. The increased orange emission of Mn^{2+} at the expense of the quenched Tb^{3+} emissions allowed tunable photoluminescence to exist via concentration tuning.

4.2. Future Outlook

The improvement of single-phased full color-emitting phosphors will continue to attract attention in the near future. It is important to emphasize, the objective of this dissertation was to explore potential phosphor systems that exhibit tunable photoluminescence. However, the practical application of these phosphors into LED technology will require additional research. Undoubtedly, coupled with improving phosphor development is improving the UV-LED pump sources they will be applied to. Although longwave GaN-based UV-LEDs emitting from 375-400 nm have matured significantly in the last decade, UV-LEDs emitting from 210-350 are still in progress to catch up in terms of efficiency. However, the development of short and midwave UV-LEDs is gaining interest [90, 91]. AlGaN-based LEDs have been reported to emit at 254 nm [92], 280 nm [93, 94], and 325 nm [95] by various groups. Although the UV-LED pump sources emit single wavelengths, the benefit of tunable luminescence is having the capability to adjust the emission of the phosphor to match the excitation sources available.

In regards to recommendations for the $CaW_{0.99}Mo_{0.01}O_4:Tm^{3+}$, Tb^{3+}, Eu^{3+} phosphor, a lifetime analysis which was not employed here, would reveal if energy transfer exists between the WO_4^{2-} and MoO_4^{2-} complexes when combined into a single host. Likewise, the lifetime analysis of the Eu^{3+} emission in the blue/red-emitting $Ca_{1-2x}WO_4:Eu_xM_x$ ($M = Na^+$) system would provide a clearer understanding of how the charge compensation of Na^+ impacts the

energy transfer between WO_4^{2-} groups and Eu^{3+} ions. Concerning further studies for the silicate system, attempts to synthesize a phosphor with a closer match to the agrellite phase are ongoing. Furthermore, steps will be taken to analyze its emission when fabricated onto thin films, which will reveal its emission stability when coated onto a UV-LED chip. Initially, the 5*d*–4*f* emission of Eu^{2+} was employed instead of Tb^{3+} which provided a broad green emission (~500 nm) in the phosphor host (see Figure A1 of Appendix). However, in comparison to Tb^{3+}, the inclusion of Eu^{2+} significantly quenched the Ce^{3+} emission making the overall emission intensity of the phosphor weak. Furthermore, the addition of Mn^{2+} in turn quenched the emission of Eu^{2+}, making efforts to optimize chromaticity in the white light region difficult. Therefore, the employment of Eu^{2+} was aborted in this investigation, but future groups may consider other methods to optimize its intensity.

References

1. Zhang, H.; Fu, X.; Niu, S.; Sun, G.; Xin, Q., Photoluminescence of YVO_4:Tm phosphor prepared by a polymerizable complex method. *Solid State Commun.* **2004,** *132* (8), 527–531.

2. Xie, R.-J.; Hirosaki, N.; Mitomo, M.; Takahashi, K.; Sakuma, K., Highly efficient white-light-emitting diodes fabricated with short-wavelength yellow oxynitride phosphors. *Appl. Phys. Lett.* **2006,** *88* (10), 101104–3.

3. Mikhailik, V. B.; Kraus, H.; Wahl, D.; Itoh, M.; Koike, M.; Bailiff, I. K., One- and two-photon excited luminescence and band-gap assignment in $CaWO_4$. *Phys Rev. B* **2004,** *69* (20), 205110.

4. Mikhailik, V. B.; Kraus, H.; Miller, G.; Mykhaylyk, M. S.; Wahl, D., Luminescence of $CaWO_4$, $CaMoO_4$, and $ZnWO_4$ scintillating crystals under different excitations. *J. Appl. Phys.* **2005,** *97* (8), 083523–8.

5. Gonzalez-Ortega, J. A.; Tejeda, E. M.; Perea, N.; Hirata, G. A.; Bosze, E. J.; McKittrick, J., White light emission from rare earth activated yttrium silicate nanocrystalline powders and thin films. *Opt. Mater.* **2005,** *27*, 1221–1227.

6. Krames, M. R.; Shchekin, O. B.; Mueller-Mach, R.; Mueller, G. O.; Ling, Z.; Harbers, G.; Craford, M. G., Status and future of high-power light-emitting diodes for solid-state lighting. *J. Display Technol.* **2007,** *3* (2), 160–175.

7. Nakamura, S.; Fasol, G., *The Blue Laser Diode: GaN Based Light Emitters and Lasers*. Berlin, Germany, 1997.

8. Ye, S.; Xiao, F.; Pan, Y. X.; Ma, Y. Y.; Zhang, Q. Y., Phosphors in phosphor-converted white light-emitting diodes: Recent advances in materials, techniques and properties. *Mat. Sci. Eng. R* **2010,** *71* (1), 1–34.

9. Chen, L.; Lin, C.-C.; Yeh, C.-W.; Liu, R.-S., Light converting inorganic phosphors for white light-emitting diodes. *Materials* **2010,** *3* (3), 2172–2195.

10. Ye, S.; Liu, Z.-S.; Wang, X.-T.; Wang, J.-G.; Wang, L.-X.; Jing, X.-P., Emission properties of Eu^{2+}, Mn^{2+} in $MAl_2Si_2O_8$ (M = Sr, Ba). *J. Lumin.* **2008**, 1–5.

11. Lakshminarayana, G.; Yang, R.; Qiu, J. R.; Brik, M. G.; Kumar, G. A.; Kityk, I. V., White light emission from Sm^{3+}/Tb^{3+} codoped oxyfluoride aluminosilicate glasses under UV light excitation. *J. Phys. D: Appl. Phys.* **2009,** *42* (1), 015414.

12. Lakshminarayana, G.; Yang, H.; Qiu, J., White light emission from Tm^{3+}/Dy^{3+} co-doped oxyfluoride germanate glasses under UV light excitation. *J. Solid State Chem.* **2009,** *182* (4), 669–676.

13. Guo, C.; Zhang, W.; Luan, L.; Chen, T.; Cheng, H.; Huang, D., A promising red-emitting phosphor for white light emitting diodes prepared by sol–gel method. *Sens. Actuators, B* **2008,** *133*, 33–39.

14. Yang, W.-J.; Luo, L.; Chen, T.-M.; Wang, N.-S., Luminescence and energy transfer of Eu- and Mn-coactivated $CaAl_2Si_2O_8$ as a potential phosphor for white-light UVLED. *Chem. Mater.* **2005,** *17* (15), 3883–3888.

15. Yang, W.-J.; Chen, T.-M., White-light generation and energy transfer in $SrZn_2(PO_4)_2$:Eu,Mn phosphor for ultraviolet light-emitting diodes. *Appl. Phys. Lett.* **2006,** *88* (10), 101903–3.

16. Kim, J. S.; Jeon, P. E.; Park, Y. H.; Choi, J. C.; Park, H. L.; Kim, G. C.; Kim, T. W., White-light generation through ultraviolet-emitting diode and white-emitting phosphor. *Appl. Phys. Lett.* **2004,** *85* (17), 3696–3698.

17. Kim, J. S.; Lim, K. T.; Jeong, Y. S.; Jeon, P. E.; Choi, J. C.; Park, H. L., Full-color $Ba_3MgSi_2O_8$: Eu^{2+}, Mn^{2+} phosphors for white-light-emitting diodes. *Solid State Commun.* **2005,** *135*, 21–24.

18. Liu, S.; Zhao, G.; Ying, H.; Wang, J.; Han, G., Eu/Dy ions co-doped white light luminescence zinc–aluminoborosilicate glasses for white LED. *Opt. Mater.* **2008,** *31*, 47–50.

19. Wenbo, M.; Shi, Z.; Wang, R., Luminescence properties of full-color single-phased phosphors for white LEDs. *J. Alloys Compd.* **2010,** *503* (1), 118–121.

20. Wang, W.; Yang, P.; Gai, S.; Niu, N.; He, F.; Lin, J., Fabrication and luminescent properties of $CaWO_4$:Ln^{3+} (Ln = Eu, Sm, Dy) nanocrystals. *J. Nanopart. Res.* **2010**.

21. Nazarov, M. V.; Jeon, D. Y.; Kang, J. H.; Popovici, E.-J.; Muresan, L.-E.; Zamoryanskaya, M. V.; Tsukerblat, B. S., Luminescence properties of europium-terbium double activated calcium tungstate phosphor. *Solid State Commun.* **2004,** *131*, 307–311.

22. Blasse, G.; Grabmarier, B. C., Luminescent materials. Springer: Berlin, 1994; p 103.

23. Gao, D.; Li, Y.; Lai, X.; Wei, Y.; Bi, J.; Li, Y.; Liu, M., Fabrication and luminescence properties of Dy^{3+} doped $CaMoO_4$ powders. *Mater. Chem. Phys.* **2011,** *126* (1-2), 391–397.

24. Hou, Z.; Chai, R.; Zhang, M.; Zhang, C.; Chong, P.; Xu, Z.; Li, G.; Lin, J., Fabrication and luminescence properties of one-dimensional $CaMoO_4$: Ln^{3+} (Ln = Eu, Tb, Dy) nanofibers via electrospinning process. *Langmuir* **2009,** *25* (20), 12340–12348.

25. Cavalli, E.; Boutinaud, P.; Mahiou, R.; Bettinelli, M.; Dorenbos, P., Luminescence dynamics in Tb^{3+}-doped $CaWO_4$ and $CaMoO_4$ crystals. *Inorg. Chem.* **2010,** *49* (11), 4916–4921.

26. Zalga, A.; Sazinas, R.; Garskaite, E.; Kareiva, A.; Bareika, T.; Tamulaitis, G.; Juskenas, R.; Ramanauskas, R., Sol-gel synthesis of RE^{3+}-activated $CaWO_4$ phosphores. *Chemija* **2009,** *20* (3), 169–174.

27. Grobelna, B.; Lipowska, B.; Klonkowski, A. M., Energy transfer in calcium tungstate doped with Eu(III) or Tb(III) ions incorporated into silica xerogel. *J. Alloys Compd.* **2006,** *419* (1-2), 191–196.

28. Zhu, F.; Xiao, Z.; Yan, L.; Zhang, F.; Huang, A., The influence on intrinsic light emission of calcium tungstate and molybdate powders by multivalence Pr codoping. *Appl. Phys. A* **2010**, 1–5.

29. Wang, W.; Yang, P.; Cheng, Z.; Hou, Z.; Li, C.; Lin, J., Patterning of red, green, and blue luminescent films based on $CaWO_4:Eu^{3+}$, $CaWO_4:Tb^{3+}$, and $CaWO_4$ phosphors via microcontact printing route. *ACS Appl. Mater. Interfaces* **2011,** *3* (10), 3921–3928.

30. Liao, J.; Qiu, B.; Wen, H.; Chen, J.; You, W.; Liu, L., Synthesis process and luminescence properties of Tm^{3+} in AWO_4 (A = Ca, Sr, Ba) blue phosphors. *J. Alloys Compd.* **2009,** *487* (1-2), 758–762.

31. Liao, J.; Liu, L.; You, H.; Huang, H.; You, W., Hydrothermal preparation and luminescence property of $MWO_4:Sm^{3+}$ (M = Ca, Sr, Ba) red phosphors. *Optik - International J. Light Electron Opt.* **2011**.

32. Zhu, F.; Xiao, Z.; Zhang, F.; Yan, L.; Huang, A., Donor doping process and white light generation in $CaMoO_4$ powders with multivalence Pr codoping. *J. Lumin.* **2011,** *131* (1), 22–24.

33. Zheng, Y.; Huang, Y.; Yang, M.; Guo, N.; Qiao, H.; Jia, Y.; You, H., Synthesis and tunable luminescence properties of monodispersed sphere-like $CaWO_4$ and $CaWO_4$:Mo/Eu, Tb. *J. Lumin.* **2012,** *132* (2), 362–367.

34. Pang, M. L.; Lin, J.; Wang, S. B.; Yu, M.; Zhou, Y. H.; Han, X. M., Luminescent properties of rare-earth-doped $CaWO_4$ phosphor films prepared by the Pechini sol–gel process. *J. Phys.: Condens. Matter* **2003,** *15*, 5157–5169.

35. Yang, P.; Quan, Z.; Li, C.; Lian, H.; Huang, S.; Lin, J., Fabrication, characterization of spherical $CaWO_4$:Ln @MCM-41(Ln = Eu^{3+}, Dy^{3+}, Sm^{3+}, Er^{3+}) composites and their applications as drug release systems. *Micropor. Mesopor. Mat.* **2008,** *116* (1-3), 524–531.

36. Guild, J., The colorimetric properties of the spectrum. *Phil. Trans. R. Soc. London* **1931,** *A230*, 149.

37. Wright, W., A re-determination of the trichromatic coefficients of the spectral colours. *Trans. Opt. Soc.* **1928,** *30*, 141.

38. Billmeyer, J., F. W.; Saltzman, M., *Principles of Color Technology*. 2nd ed.; John Wiley & Sons: New York, 1981.

39. Stevens, W. R., *Building Physics, Lighting: Seeing in the artificial environment*. Pergamon Press: Oxford, 1969.

40. Kaufman, J. E.; Christensen, J. F., *IES Lighting Handbook; the standard lighting guide*. 5th ed.; Waverly Press: New York, 1972.

41. Zhang, Q. Y.; Pita, K.; Ye, W.; Que, W. X., Influence of annealing atmosphere and temperature on photoluminescence of Tb^{3+} or Eu^{3+}-activated zinc silicate thin film phosphors via sol-gel method. *Chem. Phys. Lett.* **2002,** *351* (3-4), 163–170.

42. Zhang, Q. Y.; Pita, K.; Buddhudu, S.; Kam, C. H., Luminescent properties of rare-earth ion doped yttrium silicate thin film phosphors for a full-colour display. *J. Phys. D: Appl. Phys.* **2002,** *35* (23), 3085.

43. Li, X.; Yang, Z.; Guan, L.; Guo, J.; Wang, Y.; Guo, Q., Synthesis and luminescent properties of $CaMoO_4$:Tb^{3+}, R^+ (Li^+, Na^+, K^+). *J. Alloys Compd.* **2009,** *478* (1-2), 684–686.

44. Shi, S.; Gao, J.; Zhou, J., Effects of charge compensation on the luminescence behavior of Eu^{3+} activated $CaWO_4$ phosphor. *Opt. Mater.* **2008,** *30* (10), 1616–1620.

45. Xie, A.; Yuan, X.; Hai, S.; Wang, J.; Wang, F.; Li, L., Enhancement emission intensity of $CaMoO_4:Eu^{3+}$, Na^+ phosphor via Bi co-doping and Si substitution for application to white LEDs. *J. Phys. D: Appl. Phys.* **2009,** *42* (10), 105107.

46. Su, Y.; Li, L.; Li, G., Synthesis and optimum luminescence of $CaWO_4$-based red phosphors with codoping of Eu^{3+} and Na^+. *Chem. Mat.* **2008,** *20* (19), 6060–6067.

47. Teshima, K.; Yubuta, K.; Sugiura, S.; Fujita, Y.; Suzuki, T.; Endo, M.; Shishido, T.; Oishi, S., Selective growth of calcium molybdate whiskers by rapid cooling of a sodium chloride flux. *Cryst. Growth Des.* **2006,** *6* (7), 1598–1601.

48. Tyson, R. M.; Hemphill, W. R.; Theisen, A. F., Effect of the W: Mo ratio on the shift of excitation and emission spectra in the scheelite-powellite series. *American Miner.* **1988,** *73*, 1145–1154.

49. Nazarov, M. V.; Tsukerblat, B. S.; Popovici, E. J.; Jeon, D. Y., Optical lines in europium-terbium double activated calcium tungstate phosphor. *Phys. Lett. A* **2004,** *330* (3-4), 291–298.

50. Jin, Y.; Hao, Z.; Zhang, X.; Luo, Y.; Wang, X.; Zhang, J., Dynamical processes of energy transfer in red emitting phosphor $CaMoO_4:Sm^{3+}$, Eu^{3+}. *Opt. Mater.* **2011,** *33* (11), 1591–1594.

51. Yu, Q.; Liu, Y.; Wu, S.; Lu, X.; Huang, X.; Li, X., Luminescent properties of $Ca_2SiO_4:Eu^{3+}$ red phosphor for trichromatic white light emitting diodes. *J. Rare Earths* **2008,** *26* (6), 783–786.

52. Thongtem, T.; Phuruangrat, A.; Thongtem, S., Characterization of $MeWO_4$ (Me = Ba, Sr and Ca) nanocrystallines prepared by sonochemical method. *Appl. Surf. Sci.* **2008,** *254* (23), 7581–7585.

53. Monje, O.; Stutte, G. W.; Goins, G. D.; Porterfield, D. M.; Bingham, G. E., Farming in space: Environmental and biophysical concerns. *Adv. Space Res.* **2003,** *31* (1), 151–167.

54. Kim, H.-H.; Goins, G. D.; Wheeler, R. M.; Sager, J. C., Green-light supplementation for enhanced lettuce growth under red- and blue-light-emitting diodes. *Hortscience* **2004,** *39* (7), 1617–1622.

55. Goins, G. D.; Yorio, N. C.; Sanwo, M. M.; Brown, C. S., Photomorphogenesis, photosynthesis, and seed yield of wheat plants grown under red light-emitting diodes (LEDs) with and without supplemental blue lighting. *J. Exp. Bot.* **1997,** *48* (7), 1407–1413.

56. Warrington, I. J.; Mitchell, K. J., The influence of blue- and red-biased light spectra on the growth and development of plants. *Agr. Meteorol.* **1976,** *16* (2), 247–262.

57. Klotz, I. New Greenhouse Promises Fresh Salad in Space. **http://news.discovery.com/space/greenhouse-promises-fresh-salad-in-space.html**. **2010**.

58. Jia, P. Y.; Liu, X. M.; Li, G. Z.; Yu, M.; Fang, J.; Lin, J., Sol-gel synthesis and characterization of SiO_2@$CaWO_4$,SiO_2@$CaWO_4$:Eu^{3+}/Tb^{3+} core–shell structured spherical particles. *Nanotechnology* **2006,** *17* (3), 734–742.

59. Du, H.; Fuh, R. A.; Li, J.; Corkan, A.; Lindsey, J. S., PhotochemCAD: A computer-aided design research tool in photochemistry. *Photochem. Photobiol.* **1998,** *68*, 141–142.

60. Cheng, H.; Hu, Y., Mercury in municipal solid waste in China and its control: A review. *Environ. Sci. Technol.* **2012,** *46* (2), 593–605.

61. Jang, H.; Won, Y. H.; Jeon, D., Improvement of electroluminescent property of blue LED coated with highly luminescent yellow-emitting phosphors. *Appl. Phys. B.* **2009,** *95* (4), 715–720.

62. Lu, W.; Hao, Z.; Zhang, X.; Luo, Y.; Wang, X.; Zhang, J., Tunable full-color emitting $BaMg_2Al_6Si_9O_{30}$:Eu^{2+}, Tb^{3+}, Mn^{2+} phosphors based on energy transfer. *Inorg. Chem.* **2011,** *50* (16), 7846–7851.

63. Choi, N.-S.; Park, K.-W.; Park, B.-W.; Zhang, X.-M.; Kim, J.-S.; Kung, P.; Margaret Kim, S., Eu^{2+}-Mn^{2+} energy transfer in white-light-emitting T-phase $(Ba,Ca)_2SiO_4:Eu^{2+}$, Mn^{2+} phosphor. *J. Lumin.* **2010,** *130* (4), 560–566.

64. Nishida, T.; Ban, T.; Kobayashi, N., High-color-rendering light sources consisting of a 350-nm ultraviolet light-emitting diode and three-basal-color phosphors. *Appl. Phys. Lett.* **2003,** *82* (22), 3817–3819.

65. Wu, H.; Zhang, X.; Guo, C.; Xu, J.; Wu, M.; Su, Q., Three-band white light from InGaN-based blue LED chip precoated with green/red phosphors. *IEEE Photonic. Technol. Lett.* **2005,** *17* (6), 1160–1162.

66. Li, G.; Zhang, Y.; Geng, D.; Shang, M.; Peng, C.; Cheng, Z.; Lin, J., Single-composition trichromatic white-Emitting $Ca_4Y_6(SiO_4)_6O$: $Ce^{3+}/Mn^{2+}/Tb^{3+}$ phosphor: luminescence and energy transfer. *ACS Appl. Mater. Interfaces* **2012,** *4* (1), 296–305.

67. Sun, X.; Zhang, J.; Zhang, X.; Lu, S.; Wang, X., A white light phosphor suitable for near ultraviolet excitation. *J. Lumin.* **2007,** *122-123*, 955–957.

68. Ye, X.; Yang, Y.; Liao, C.; Yang, F., Single-phase full-color $Ba_3Lu_2(SiO_4)_3:Eu^{2+}$ phosphor for white-light emitting diodes. *J. Rare Earths* **2011,** *29* (11), 1026–1028.

69. Shionoya, S.; Yen, W. M., *Phosphor handbook*. CRC Press: Boca Raton, 1999; p 1018.

70. Qiao, X.; Luo, Q.; Fan, X.; Wang, M., Local vibration around rare earth ions in alkaline earth fluorosilicate transparent glass and glass ceramics using Eu^{3+} probe. *J. Rare Earth* **2008,** *26* (6), 883–888.

71. Gaft, M.; Reisfeld, R.; Panczer, G., Interpretation of Luminescence Centers. In *Modern Luminescence Spectroscopy of Minerals and Materials*, Springer Berlin Heidelberg New York: 2005; 119–251.

72. Toncelli, A.; Bonelli, L.; Faoro, R.; Parisi, D.; Tonelli, M., Investigation of Pr-doped fluoride crystals as possible white-light emitters. *Opt. Mater.* **2009,** *31* (8), 1205–1209.

73. Lin, C. C.; Xiao, Z. R.; Guo, G.-Y.; Chan, T.-S.; Liu, R.-S., Versatile phosphate phosphors $ABPO_4$ in white light-emitting diodes: collocated characteristic analysis and theoretical calculations. *J. Am. Chem. Soc* **2010,** *132* (9), 3020–3028.

74. Wu, Z.-C.; Liu, J.; Hou, W.-G.; Xu, J.; Gong, M.-L., A new single-host white-light-emitting $BaSrMg(PO_4)_2$: Eu^{2+} phosphor for white-light-emitting diodes. *Journal of Alloys and Compounds* **2010,** *498* (2), 139–142.

75. Fuchs, E. C.; Sommer, C.; Wenzl, F. P.; Bitschnau, B.; Paulitsch, A. H.; Muhlanger, A.; Gatterer, K., Polyspectral white light emission from Eu^{3+}, Tb^{3+}, Dy^{3+}, Tm^{3+} co-doped $GdAl_3(BO_3)_4$ phosphors obtained by combustion synthesis. *Mat. Sci. Eng. B* **2009,** *156* (1-3), 73–78.

76. Zhu, G.; Wang, Y.; Ci, Z.; Liu, B.; Shi, Y.; Xin, S., $Ca_8Mg(SiO_4)_4Cl_2$:Ce^{3+}, Tb^{3+}: A potential single-phased phosphor for white-light-emitting diodes. *J. Lumin.* **2012,** *132* (2), 531–536.

77. Kim, J. S.; Jeon, P. E.; Choi, J. C.; Park, H. L.; Mho, S. I.; Kim, G. C., Warm-white-light emitting diode utilizing a single-phase full-color $Ba_3MgSi_2O_8$:Eu^{2+}, Mn^{2+} phosphor. *Appl. Phys. Lett.* **2004,** *84* (15), 2931–2933.

78. Wang, B.; Sun, L.; Ju, H.; Zhao, S.; Deng, D.; Wang, H.; Xu, S., Single-phased white-light emitting $CaAl_2Si_2O_8$: Eu^{2+}, Mn^{2+} phosphors prepared by a sol–gel method. *J. Sol-Gel Sci. Technol.* **2009,** *50*, 368–371.

79. Fleischer, M.; Mandarino, J. A., New mineral names. *American Miner.* **1977,** *62*, 173–176.

80. Gittens, J.; Bown, M. G.; Sturman, D., Agrellite, a new rock-forming mineral in regionally metamorphosed agpaitic alkalic rocks. *Can. Mineral.* **1976,** *14*, 120–126.

81. Ghose, S.; C., W., A new type of silicate double chain in agrellite, $NaCa_2Si_4O_{10}F$. *Naturwissenchaften* **1978,** *65*.

82. Ghose, S.; C., W., Agrellite, $Na(Ca,RE)_2Si_4O_{10}F$: a layer structure with silicate tubes. *American Miner*. **1979,** *64*, 563–572.

83. Rozhdestvenskaya, I. V.; Nikishova, L. V., Crystallochemical characteristics of alkali calcium silicates from charoitites. *Crystallogr. Rep.* **2002,** *47* (4), 545–554.

84. Wang, B.; Sun, L.; Ju, H., Synthesis of $Ca_3Al_6Si_2O_{16}:Ce^{3+}$, Tb^{3+} phosphors by sol–gel method and optical properties. *J Sol-Gel Sci. Technol.* **2010,** *53* (2), 454–458.

85. Socrates, G., *Infrared and raman characteristic group frequencies tables and charts*. 3rd ed.; John Wiley & Sons: West Sussex, England, 2001.

86. Luyt, A. S.; Dramicanin, M. D.; Antic, Z.; Djokovc, V., Morphology, mechanical and thermal properties of composites of polypropylene and nanostructured wollastonite filler. *Polym. Test.* **2009,** *28* (3), 348–356.

87. Blasse, G.; Grabmarier, B. C., *Luminescent materials*. Springer: Berlin, 1994.

88. Thomas, R. B.; Smith, P. A.; Jaleel, A.; Vogel, P.; Crawford, C.; Assefa, Z.; Sykora, R. E., Synthesis, structural, and photoluminescence studies of $Gd(terpy)(H_2O)(NO_3)_2M(CN)_2$ (M = Au, Ag) complexes: multiple emissions from intra- and intermolecular excimers and exciplexes. *Inorg. Chem.* **2012,** *51* (6), 3399–3408.

89. Nazarov, M. V.; Tsukerblat, B. S.; Popovici, E. J.; Jeon, D. Y., Polarization selection rules for the allowed optical transitions in europium-terbium double activated calcium tungstate phosphor. *Solid State Chem.* **2005,** *133* (3), 203–208.

90. Hirayama, H.; Yatabe, T.; Noguchi, N.; Kamata, N., Development of 230-270 nm AlGaN-based deep-UV LEDs. *Electr. Commun. Jpn.* **2010,** *93* (3), 24–33.

91. Khan, A.; Balakrishnan, K.; Katona, T., Ultraviolet light-emitting diodes based on group three nitrides. *Nat. Photonics* **2008,** *2* (2), 77–84.

92. Wu, S.; Adivarahan, V.; Shatalov, M.; Chitnis, A.; Sun, W.-H.; Khan, M. A., Micro-pixel design milliwatt power 254 nm emission light emitting diodes. *Jpn. J. Appl. Phys.* **2004,** *43* (8A), L1035–L1037.

93. Shatalov, M.; Gong, Z.; Gaevski, M.; Wu, S.; Sun, W.; Adivarahan, V.; Khan, M. A., Reliability of AlGaN-based deep UV LEDs on sapphire. *Proc. SPIE* **2006,** *6134*, 61340P-1-61340P11.

94. Adivarahan, V.; Heidari, A.; Zhang, B.; Fareed, Q.; Hwang, S.; Islam, M.; Khan, A., 280 nm deep ultraviolet light emitting diode lamp with an AlGaN multiple quantum well active region. *Appl. Phys. Express* **2009,** *2*, 102101.

95. Chitnis, A.; Zhang, J. P.; Adivarahan, V.; Shatalov, M.; Wu, S.; Pachipulusu, R.; Mandavilli, V.; Khan, M. A., Improved performance of 325-nm emission AlGaN ultraviolet light-emitting diodes. *Appl. Phys. Lett.* **2003,** *82* (16), 2565–2567.

Appendix

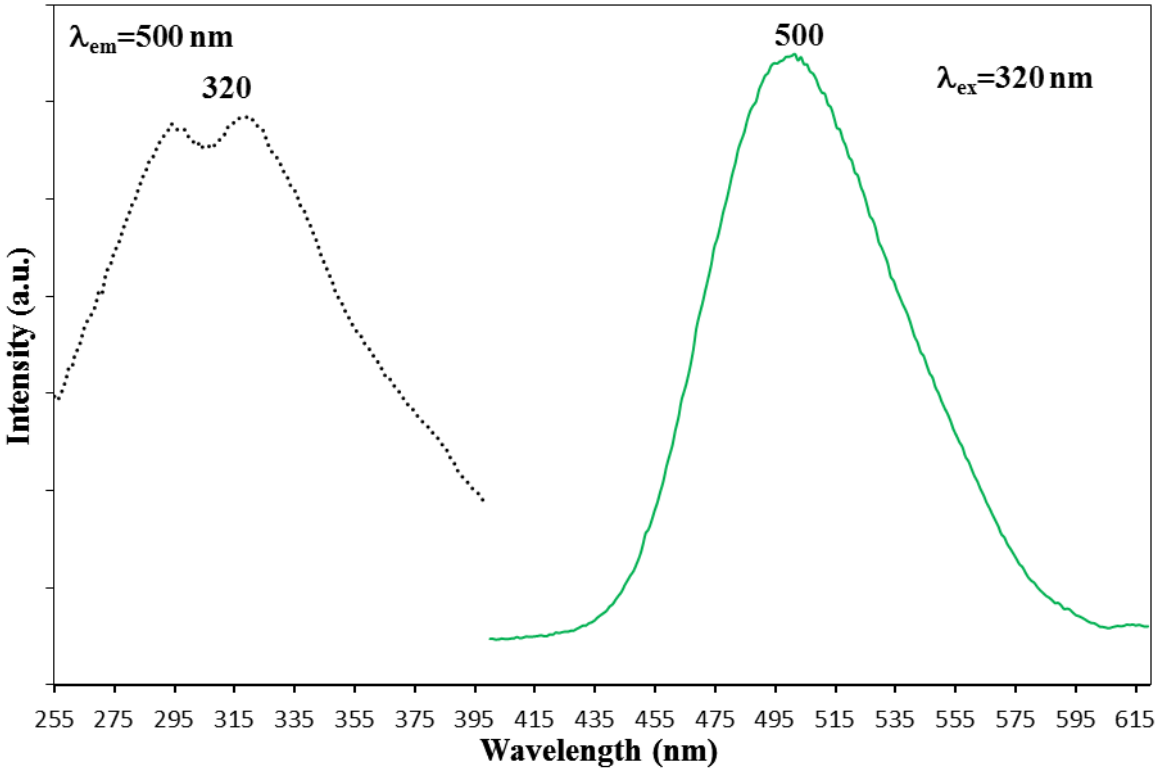

Figure A1. Excitation and emission spectra $CaSiO_3$:0.01Eu^{2+} synthesized for future studies.

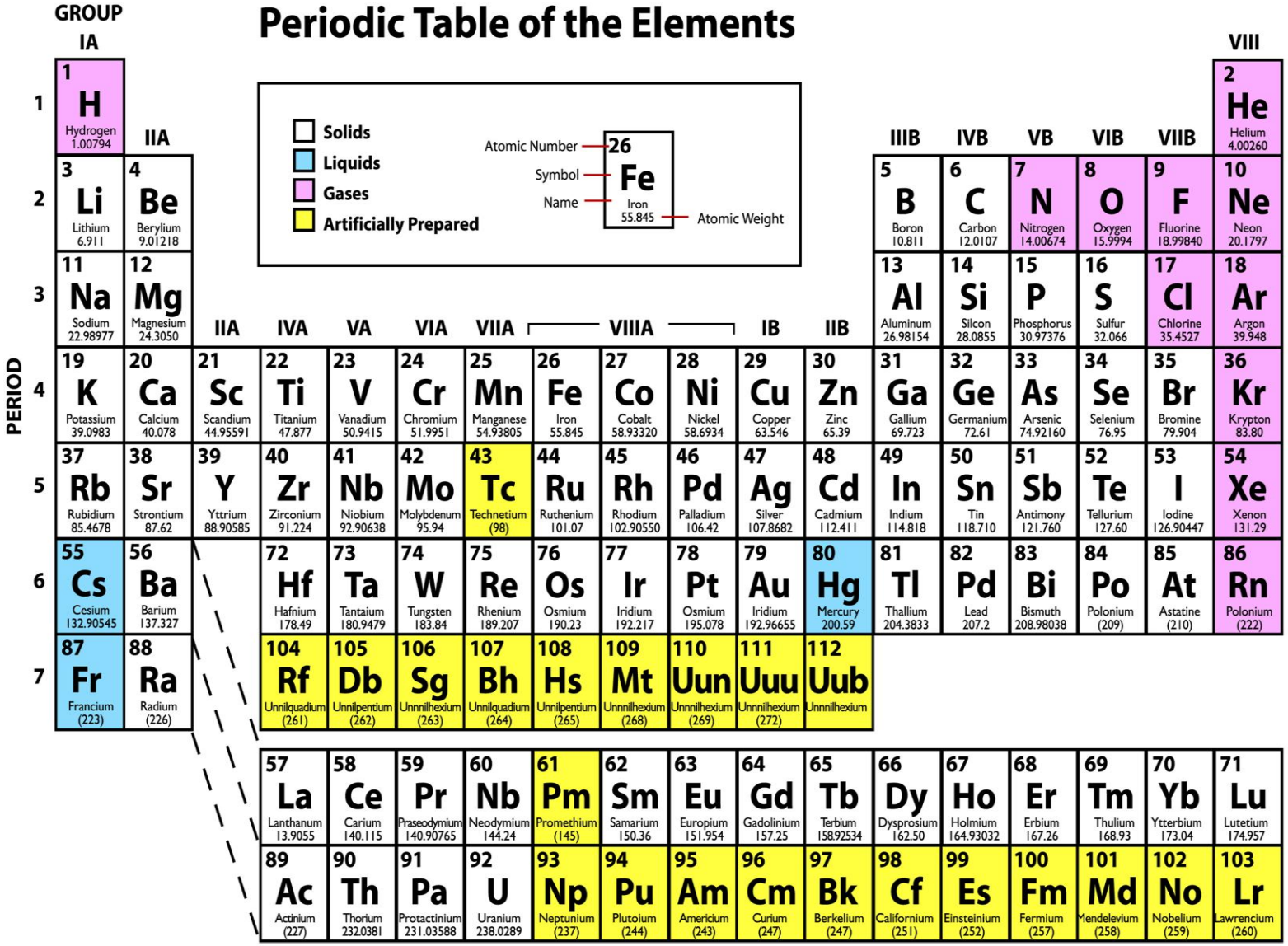

Figure A2. The periodic table of the elements.

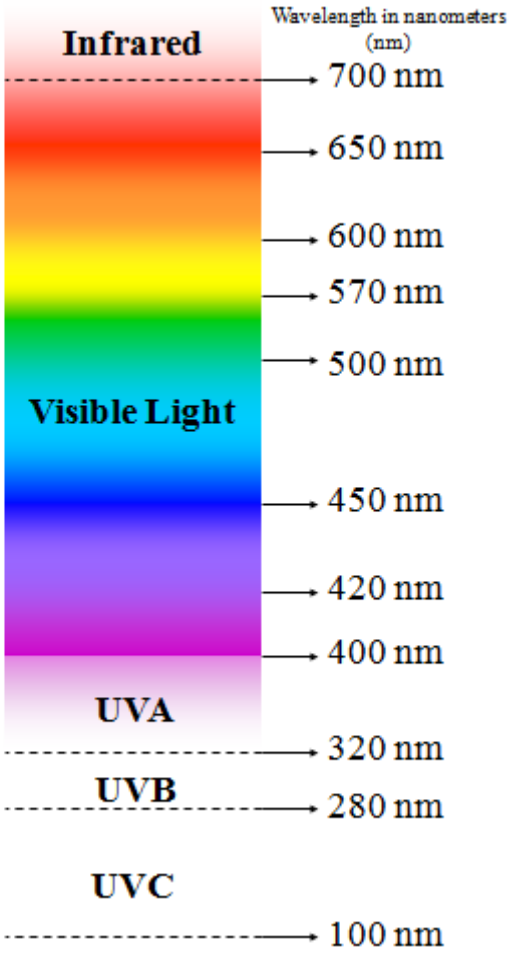

Figure A3. Relevant portion of the electromagnetic spectrum.